Aalto University
School of Engineering

Renée Mie Fredensborg Hansen

Assessment of NASA's ICESat-2 photon counting laser altimeter in the Baltic Sea to support ice mapping estimates of ridging and local bathymetry

Master's thesis for the degree of Master of Science in Technology as part of the double-degree of Cold Climate Engineering submitted for inspection.

Espoo, 25.05.2020
Supervisor: Assistant Professor Jaan Praks
Advisor(s): Senior Researcher Henriette Skourup (DTU)
Research Scientist Eero Rinne (FMI)

Approval

Thesis submitted in fulfilment of the requirements for the degree of Master of Science in Technology at Aalto University and the degree of Master of Science in Earth and Space Physics and Engineering at The Technical University of Denmark (DTU). The two degrees fall under the combined double-degree Nordic Master in Cold Climate Engineering with specialisation in Earth Observation and Space Tracking. The work presented herein was conducted at the Finnish Meteorological Institute (FMI) in Helsinki, Finland, from January 2020 to May 2020.

Hvidovre - Denmark, 25.05.2020

Supervisor:	Henriette Skourup, Senior Researcher, DTU
Supervisor:	Jaan Praks, Assistant Professor, Aalto University
Advisor:	Eero Rinne, Research Scientist, FMI

Renée Mie Fredensborg Hansen - s1535357 (DTU) and 771708 (Aalto University)

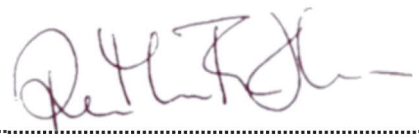

Signature

25-05-2020

Date

Aalto University
School of Engineering

Aalto University, P.O. BOX 11000, 00076
AALTO
www.aalto.fi

Abstract of master's thesis

Author Renée Mie Fredensborg Hansen

Title of thesis Assessment of NASA's ICESat-2 photon counting laser altimeter in the Baltic Sea to support ice mapping estimates of ridging and local bathymetry

Master programme Cold Climate Engineering **Code** ENG216

Thesis supervisor Assistant Professor Jaan Praks (Aalto)

Thesis advisor(s) Senior Researcher Henriette Skourup (DTU), Research Scientist Eero Rinne (FMI)

Date 25.05.2020 **Number of pages** 96+18 **Language** English

Abstract

The Ice, Cloud and land Elevation Satellite (ICESat-2) is the first Earth-orbiting photon counting laser altimeter. The novel measurements strategy allows for unprecedented global elevation measurements useful for measuring sea ice and shallow water bathymetry at high resolution. This thesis will assess how well ICESat-2 photon observations compare with ice charts from the Finnish Ice Service (FIS) and estimate ridging features in the Baltic, and asses to what extent shallow water bathymetry in the Baltic can be derived.

With sea ice being a main concern of a navigator in ice-covered regions, it is necessary to provide a deformation numeral of degree of ice ridging (DIR) to aid navigation, which provides guidance on whether a ship can safely pass through an area. The FIS ice charts provide DIR information based on ice breaker observations and SAR images. With the high-resolution and dense surface elevation observations from ICESat-2, this thesis has shown it possible to differentiate and estimate DIR. Aggregating segments of 150 photons and estimating relative elevation measurements on ridging proved able separate the observations into different levels of deformation. Future work includes additional filtration schemes to remove erroneous photons from low-laying clouds, fog and/or background sun events. These results are the first to showcase ICESat-2's ability to measure small-scale roughness structures and encourages scientists to explore ICESat-2 photons for sea ice pressure ridge detection.

Shallow water bathymetry is notoriously difficult to map, but of great interest to science applications, ship navigation and engineering applications. Presented here are the first results of shallow water bathymetry in the murky and eutrophicated waters of the Baltic. Maximum depth down to 16~m depth and average maximum depth of 8.58~m was identified and based on monthly maximum Secchi depths (1979-2018), ICESat-2 proved able to retrieve depths up to 0.87 of the maximum Secchi depth. ICESat-2 also identified specific submerged features at high resolution. Overall, these results present the capability of ICESat-2 to estimate shallow water bathymetry in more turbid waters than previously studied. Future work includes applying refraction corrections, which is estimated to be 0-5~m for depths of 0-20~m.

Keywords laser altimetry, sea ice, shallow water bathymetry, remote sensing, Baltic Sea, ICESat-2

Preface

This dissertation is submitted to the degree of Master of Science in Technology at Aalto University in Finland and the degree of Master of Science in Earth and Space Physics and Engineering at The Technical University of Denmark, both under the double-degree Nordic Master in Cold Climate Engineering.

The work described herein was conducted under the supervision of Senior Researcher Henriette Skourup at Department of Geodesy and Earth Observation, DTU Space and Assistant Professor Jaan Praks at School of Electrical Engineering, Aalto University during the period from January 2020 to May 2020 and conducted under the advisement of Research Scientist Eero Rinne at The Marine Research Unit, Finnish Meteorological Institute (FMI). The work is original to the best of my knowledge except where either acknowledgements, references or citations to previous work are stated. Neither this, nor any substantially similar dissertation, has been or is being submitted to any form of degree at any other University apart from the already mentioned.

This dissertation is partly based on results presented in a Brief Communication manuscript soon to be submitted for review in the journal The Cryosphere or in Remote Sensing. The working title is currently; *Brief communication: Estimation of degree of sea ice ridging in the Bay of Bothnia based on geolocated photons from ICESat-2* with author of this thesis as first author. The manuscript to be submitted is currently made in collaboration with Henriette Skourup (DMI), Eero Rinne (FMI) and Sinead Farrell (University of Maryland and NOAA affiliate).

Acknowledgements

I would like to give my sincerest thanks to my supervisor Henriette Skorup for the endless support, guidance, enthusiasm, encouragement and friendship throughout not only this but several projects. I hope this will not be our last. Furthermore, would I like to express my gratitude to my supervisor Jaan Praks for the great insights and for finding this incredible project for me to work with and indulge myself in. I am indebted to Eero Rinne for allowing me to partake in this work and to learn from him. Thank you for the great inputs, for the patience in me and for the invaluable comments throughout this project. It has been an amazing journey and I am forever grateful for the opportunity.

Thank you to The Finnish Meteorological Institute (FMI) for allowing me to work in the heart of research, and for all the insights the employees have given me, in particular: Mikko Lensu, Jaakko Seppänen, Juoni Vainio, Juha Karvonen, Heidi Sallila and Patrick Eriksson. A huge thanks to Hermanni Kaartokallio at the Finnish Environment Institute (SYKE) for the insights into Secchi dephs and bathymetry in the Baltic. In addition, my deepest gratitude to Heidi, Olga, Laura, Hedi and Burak at FMI for the great lunch-talks and the laughs.

I would like to express my deepest gratitude to my husband, my rock, for endless support, love and faith in me and for coming along on this one year journey to Finland with me. I could not have finished this without you. To my family and my friends for the unfailing encouragement and the optimism. To the Internachos group at Aalto University for an absolute blast with karaoke nights, dinners, Sitsits and for the friendship they have showed me during my one year stay in Finland. Thank you to Ilaria for the encouragement, the long talks, the support and the friendship. My deepest thanks to Stephanie, for enriching my abroad experience with her invaluable friendship, for the weekly coffee dates that took my mind of studies just for a little and for the tough love. Thank you to Rikke, my confidant, for absolutely everything during the last five years. This degree simply would not have been the same without you.

A final thanks is due to NASA's ICESat-2 team for a great introductory workshop, that took place at FMI in November. ICESat-2 measurements used in this study are available from the National Snow and Ice Center (NSIDC) or at NASA Open Earth Search. Daily ice charts were provided by the Finnish Ice Service (FIS). Secchi depths were provided by Baltic Marine Environment Protection Commission – Helsinki Commission (HELCOM). Depth profiles can be retrieved from the Baltic Sea Bathymetry Database (BSBD) online data base.

Contents

List of Figures

List of Tables

Acronyms

ALB Airborne LIDAR Bathymetry.

AOI Area of Interest.

ATLAS Advanced Topographic Laser Altimeter System.

ATM Airborne Topographic Mapper.

BIM Baltic Icebreaking Management.

BSBD Baltic Sea Bathymetry Database.

BSHC Baltic Sea Hydrographic Commission.

CDOM Colored Dissolved Organic Matter.

CMEMS Copernicus Marine Environment Monitoring Service.

DEM Digital Elevation Model.

DIR Degree of Ice Ridging.

DMS Digital Mapping System.

EAARL-B Experimental Advanced Airborne Research Lidar-B.

ECF Earth Centred Fixed.

ECI Earth Centred Inertial.

EM Electro-Magnetic.

ERS-1 European Remote sensing Satellite-1.

ESA The European Space Agency.

EW Extra-Wide.

FIS Finnish Ice Service.

FMI Finnish Meteorological Institute.

FY First-Year.

GLAS Geoscience Laser Altimeter System.

GRD Groun-Range Detected.

GT Ground Track.

HDF5 Hierarchical Data Format 5.

HELCOM Baltic Marine Environment Protection Commission – Helsinki Commission.

ICES International Council for the Exploration of the Sea.

ICESat Ice, Cloud and land Elevation Satellite.

ICESat-2 Ice, Cloud and land Elevation Satellite-2.

ITRF2014 International Terrestrial Reference Frame 2014.

LIDAR Light Detection And Ranging.

LSS Local Sea Surface.

MABEL Multiple Altimeter Beam Experiment Lidar.

MAD Mean Absolute Deviation.

MBES Multi-Beam Echo-Sounders.

MDT Mean Dynamic Topography.

MIZ Marginal Ice Zone.

MODIS Moderate Resolution Imaging Spectroradiometer.

MSS Mean Sea Surface.

MY Multi-Year.

NASA National Aeronautics and Administration.

NIR Near Infra-Red.

POD Precise Orbit Determination.

PPD Precise Pointing Determination.

PRF Pulse Repetition Frequency.

RANSAC Random Sample Consensus.

RGT Reference Ground Track.

RMSE Root Mean Square Error.

S-1 Sentinel-1.

SAR Synthetic Aperture Radar.

SD Standard Deviation.

SNR Signal-to-Noise Ratio.

SSH Sea Surface Height.

SYKE Finnish Environment Institute.

TEP Transmitter Echo Path.

TIN Triangular Irregular Networks.

TOF Time of Flight.

TRI Terrain Ruggedness Index.

VIIRS Visible Infrared Imaging Radiometer Suite.

WGS84 World Geodetic System 1984.

1 Introduction

The motivation and background for this thesis is presented. In addition, objectives and content of this work is presented in this Section as well.

1.1 Motivation

The Baltic Sea (see Fig. 1.1), located in the Northern Europe, is one of the largest brackish waters, defined as having higher salinity than freshwater but lower than seawater, in the world with an extent from 54° N to 66° N and a total area of 422 000 km^2 (Ronkainen et al., 2018). The Baltic can be divided into sub-regions such as: the Kattegat, the Danish Straits, the Arkona Basin, the Bornholm Basin, the Gotland Sea (these three are together known as the Baltic Proper), the Gulf of Riga, the Gulf of Bothnia and the Gulf of Finland. The Gulf of Bothnia can be further divided into the Bothnian Sea and the Bay of Bothnia (Furman et al., 2013). With the Baltic Sea's only connection to the North Sea being through the Sound (Øresund) and the Belt Seas and the exchange of water taking a profound amount of time, it allows for high salinity waters to enter the Baltic basin. Numerous rivers outflows in the Baltic while carrying fresh water equal to about 1/40 of the total yearly water column with it. The combination of the highly saline water and fresh water provides the hydrological conditions for the characteristics brackish waters (Ronkainen et al., 2018). With a location in the temperate climate zone, it means that the middle and northern areas of the Baltic Sea (the Bothnian Sea) have long winters with strong frosts. Subsequently, the southern areas have mild and relatively moist winters (EEA, 2019). This also means, that

Figure 1.1: The Baltic Sea and its sub-basins from Leppäranta and Myrberg (2009).

the northern part of the Baltic experiences a seasonal ice cover and with heavy wintertime ship navigation, it is important and necessary to monitor all the daily changes (HELCOM, 2018).

The Baltic Sea is busy with approximately 3948 vessels assisted by ice breakers per ice season (based on 10 year average, 2009-2019, from Baltic Icebreaking Management (BIM) reports), thus proper navigation is a necessity. For a navigator in the Baltic, a primary concern is sea ice. Sea ice is the main contributor to restrictions in navigation since it restricts the navigators movements (Ronkainen et al., 2018). With a maximum annual ice extent ranging from 12 to 100 % of the whole Baltic Sea area and an average of 40 %, precise monitoring of the sea ice conditions is key to limit the vessel assistance from ice breakers during the ice season (Seinä and Palosuo, 1991). The Finnish Ice Service (FIS) produce daily ice charts during the ice season which provides the ship navigators with essential information on the ice conditions including; average, minimum and maximum ice thickness, ice concentration, ice type, sea surface temperature and a deformation numeral (Degree of Ice Ridging (DIR)) (Ronkainen et al., 2018). Especially DIR is important, as it basically tells whether a ship can navigate safely through a passage (considering the ship characteristics such as ice class and *dwt* (dead-weight tonnage)) (Gegiuc et al., 2018). DIR is primarily based on observations from ice breakers and partly on Synthetic Aperture Radar (SAR) imagery and visible or Near Infra-Red (NIR) imagery (Ronkainen et al., 2018). In this dissertation, we make an assessment of the measurements from Ice, Cloud and land Elevation Satellite-2 (ICESat-2), a laser altimeter that utilises a novel multi-beam configuration photon-counting measurement approach (Markus et al., 2017). ICESat-2 builds on the heritage of its predecessor Ice, Cloud and land Elevation Satellite (ICESat), but overcomes its limitations with the re-designed measuring strategy that allows for denser surface measurements and cross-track sampling, giving the opportunity of acquiring instantaneous slope measurements (Brunt et al., 2019). We especially want to demonstrate the capabilities of ICESat-2 in estimating DIR, as this is the most useful information for the ship navigators (Gegiuc et al., 2018).

An assessment of the bathymetric capabilities of ICESat-2 in the Baltic Sea will also be provided. Shallow water bathymetry, also known as coastal or nearshore bathymetry, is notoriously difficult to map. Nonetheless, the interest appears to grow despite the challenges in acquiring the data. This can be attributed to the shallow water applications which includes e.g. shallow water hydrodynamics, sediment transport and morphology. Shallow waters can also prove dangerous for ships and small boats to operate in, due to e.g. submerged hazards (such as rocks or corals) (Parrish et al., 2019).

The possibility of measuring shallow water bathymetry can provide extremely useful information to science applications, management, ship navigation and engineering applications. Utilising ICESat-2's green laser (532 nm) provides the possibility of measuring shallow water bathymetry due to its water penetrating capabilities (Li et al., 2019). Parrish et al. (2019) showed how ICESat-2 coastal bathymetric measurements could be acquired over the U.S. Virgin Islands, where the detection of seafloor was possible in water depths of up to $\sim$40 m. However, water clarity (and quality) in the Baltic is very different from the Virgin Islands. The seasonal ice coverage in the Baltic brings nutrients to the waters and increases the eutrophication, which cause a dense growth of plant life and phytoplankton (Attila, 2019). The heavy shipping alongside being totally surrounded by land allows the Baltic to be more susceptible by pollution than other marine areas (Rhein-

heimer, 1998). All of these factors are important when considering bathymetric measurements in the Baltic since water clarity is key in having the green laser to penetrate and be reflected at the seafloor. Thus, we will assess the bathymetric capabilities of ICESat-2 in the brackish, less clear waters of the Baltic Sea. We will also touch upon the bathymetric capabilities in The Sound and Kattegat as the waters are generally more clear here (private communication, Hermanni, 2020).

1.2 Objectives

The main goal of this dissertation is to assess ICESat-2 photon measurements acquired over the Baltic Sea. There will be a primary focus on sea ice ridging and shallow water bathymetry as these applications are of most interest to Finnish Meteorological Institute (FMI). It is expected, based on prior studies on Multiple Altimeter Beam Experiment Lidar (MABEL) the airborne simulator for Advanced Topographic Laser Altimeter System (ATLAS) on board ICESat-2, that sea ice pressure ridges can be detected in the photon measurements (Farrell et al., 2015), yet no studies have elaborated further on this. A study from Parrish et al. (2019) has utilised ICESat-2 photon measurements to extract bathymetric information over the Virgin Islands, but extracting bathymetric measurements in brackish and murkier waters similar to the Baltic has to the best of our knowledge not been pursued yet.

The objectives of this dissertation includes assessing the photon measurements to support operational navigation in ice-covered areas and present a proof-of-concept for shallow waters bathymetry. Prior to the dissertation, no general method on how to approach photon measurements with regards to pressure ridges has been established. Thus, a large part of this thesis was focused on establishing a way to estimate ice ridging. For sea ice ridging we compare the ICESat-2 measurements with the FIS ice charts and extract areas where slightly ridging (DIR2), ridging (DIR3) or heavy ridging (DIR4) occurs. From here, we investigate if ridging features can be distinguished in the ICESat-2 data. Shallow water bathymetry have to some extent already been studied (e.g. Armon et al., 2020; Parrish et al., 2019). We will extract water clarity measurements (Secchi depths) to evaluate the water quality and to what extent shallow water bathymetry is possible in the Baltic. Furthermore, we will show a proof-of-concept of tracks with shallow water bathymetry from ICESat-2 and cross-compare these with the Secchi depths.

The objectives and goals can be condensed into the following research questions:

Q1 How do ICESat-2 measurements over the Baltic compare with operational ice charts?

Q2 Can ridging features (DIR in ice charts, ridge density and/or sail heights) be distinguished from the ICESat-2 data?

Q3 To what extent can coastal bathymetry in the Baltic archipelago be derived from ICESat-2 data?

1.3 Dissertation content and readership

For this dissertation, Chapter 1 presents the motivation, objectives and research questions. Chapter 2 describes the area of interest (The Baltic and to some extent the Danish Sounds), and it provides a brief introduction to sea ice formation and ice pressure ridges. In addition, the sea ice conditions and implications sea ice has on wintertime shipping is presented.

Furthermore, shallow water bathymetry and water clarity in the Baltic and Danish sounds will be presented. In Chapter 3 satellite altimetry with a specific focus on laser altimetry and ICESat-2 is presented. The study area and data description is described in Chapter 4. Chapter 5 presents the methods used in this dissertation in determining DIR and shallow water bathymetry from ICESat-2. The results are presented in Chapter 6. The discussion of the results, some future work and if the work has answered the research questions are described in Chapter 7. Chapter 8 includes future work and considerations based on findings during the work of the dissertation or thoughts and ideas on how to work with the data in the future. Chapter 9 concludes the dissertation.

Enclosed in Appendix A.1 is a description of ICESat-2's data products. Appendix A.2 presents ICESat-2 photons acquired over the Bay of Bothnia during January to March 2019. In Appendix A.3, the ICESat-2 photons denoted by a signal confidence parameter is presented and Appendix A.4 provides statistics based on these observations. Prints of the primary programs used in this study are enclosed in Appendix B.

The work presented here deals with estimating sea ice features such as pressure ridges, some of the greatest threats to ships and navigators in ice infested waters, and shallow water bathymetry, which is of interest to scientists, engineers and navigators, from the first Earth-orbiting photon-counting laser altimeter.

The primary readership for this thesis as a whole and in part are students, engineers and scientists working with or interested in:

- Ice research of sea ice features such as pressure ridges
- Hydrology and oceanography related to shallow water bathymetry and whom could be interested in the possibilities that shallow water seafloor detections provides
- Earth observation measurements

2 The Baltic and the Danish Sounds

For the Baltic and Danish Sounds, this section introduces sea ice and shallow water bathymetry. A short introduction to sea ice formation, deformation and pressure ridges in sea ice is presented. A description of maritime navigation and vessel assistance in the Baltic Sea during ice season 2018-2019 is provided. In addition, shallow water bathymetry and effects that will affect the retrieval of shallow water bathymetry from ICESat-2, including water clarity and eutrophication, is presented.

2.1 Sea ice formation

Sea ice forms by freezing of sea water. As explained by Bowditch (2019), ice can be divided into several groups depending on the characteristics of the ice type, usually related to the growth, thickness or age of the ice. The first sign of formation of new sea ice is the development of small, individual, needle-like crystals of ice known as *spicules* or *frazil ice*, which gives the sea a sort of oily appearance (see Fig. 2.1 for diagram of sea ice formation). When the spicules gathers to form a soupy layer on the surface, giving the sea a matte appearance, it is called *grease ice*. The next stage occurs when grease ice accumulates to a spongy white ice lump at a width of a few cms called *shuga*. Upon further freezing, and also depending on wind exposure, sea, shuga, salinity and grease ice, it develops into *nilas* or *ice rind*. Nilas is an elastic crust of high salinity and can be up to 10 cm in thickness with a matte surface. Ice rind has a brittle, shiny crust of low salinity with a total thickness of up to about 5 cms. New ice can also form by snow falling into seawater, called *slush*, which is near the waters freezing point but colder than the melting point of snow. Should the temperature drop below freezing point of the sea water, the slush would freeze into a ice similar to shuga. Sea ice is exposed to several type

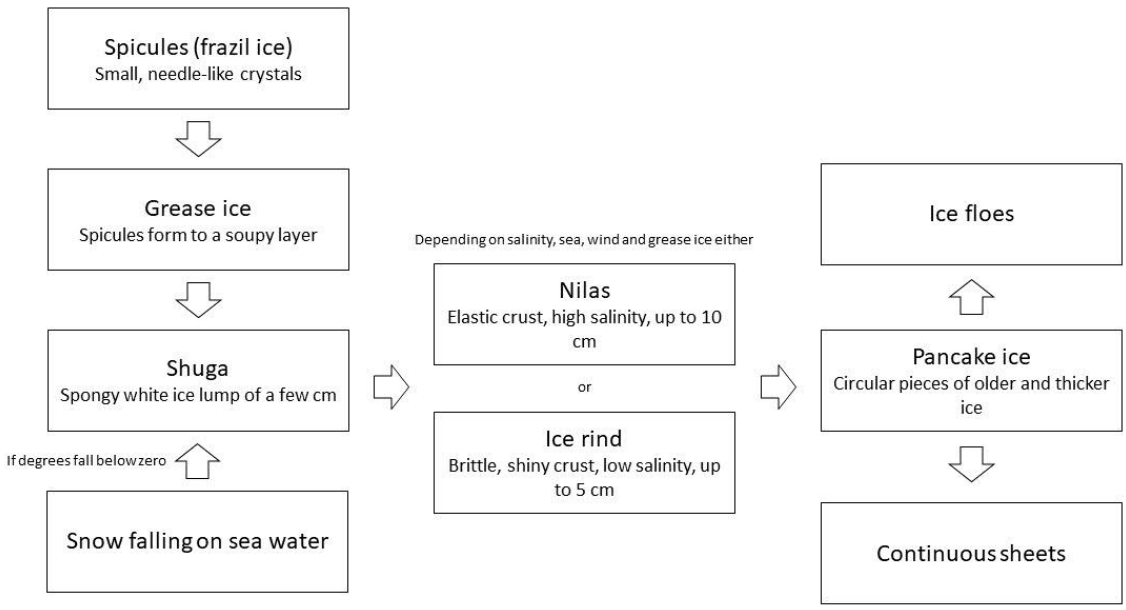

Figure 2.1: Process of sea ice formation.

of forces including waves, tides, wind, currents and temperature variations and all these forces determines the behaviour and stages of sea ice. As the ice becomes older, thicker and exposed to the influence of waves and wind, the ice will break into circular pieces called *pancake ice*. Depending on conditions the pancake ice can then develop further into either continuous sheets or *ice floes* and later on *ice fields*. When sea ice reaches a thickness of between 10 to 30 cm, it is usually referred to as *young ice*, an in-between stage between nilas and *First-Year (FY)* ice. The thickness of FY ice usually ranges from 30 cm to 2 m and is characterised by not surviving a summer melt. Sea ice surviving more than one summer melt is referred to as *Multi-Year (MY)* ice.

2.2 Sea ice pressure ridges

As explained by (Bowditch, 2019), processes of deformation occur after the development of new and young ice, which are direct consequences of the effects of winds, tides and current. Deformed ice, which is of interest in this dissertation as it can affect safe navigation, can be divided into several types depending on the key characteristics. *Bending*, the first stage in formation of pressure ice, is defined as the upward or downward motion of thin ice. After this, either *tenting* and *rafting* occurs. Tenting is where the bending creates an upward displacement of ice forming a flat sided arch with a cavity beneath. Rafting is the motion of one ice floe overriding another. When several pieces of FY ice piles over one another, it forms lines or walls of broken ice, which is referred to as a *ridge* (see Fig. 2.2). Ridges extend above and below the surface, with the extent below the sea surface, referred to as the *keel*, is often longer than the extent above the surface, known the *sail* (NSIDC, 2020b). The size and extent of ridges on sea ice depends on the ice conditions and area, which is also seen in the difference between ridge sails in the Arctic, Antarctica and the Baltic(e.g. Farrell et al., 2011; Lewis et al., 1993; Mei et al., 2019; Rabenstein et al., 2009; Tan et al., 2012). On moving ice floes, the ridges are usually formed normal

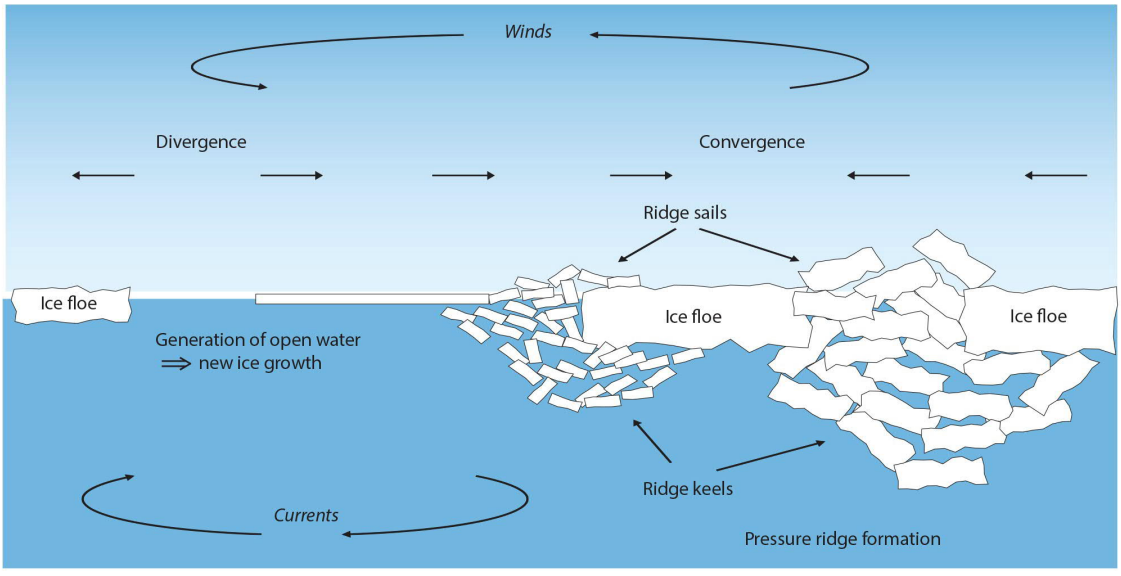

Figure 2.2: Deformation of sea ice, courtesy of AMAP. Note, due to winds and currents there will either occur divergence (ice floes separating allowing for growth of new ice since open water areas are generated) or there will occur convergence (where deformation occurs allowing the formation of pressure ridges).

to the direction of the prevailing wind and/or current. At some point, the ridge may act as sails and turn the ice floes to become parallel to the direction of the wind. The piling of the ice blocks on top of the ice surface (the sail) continues until the sail reaches its destined maximum height, however it continues below for the keel. This allows for the keel to reach up to 4 times larger than the sail. Furthermore, with brine drains throughout the ice blocks and the eventual freezing of the brine, the blocks become fused together should the weather permit it. In addition, additional bonding can develop if the surfaces of the ice blocks melt to then refreeze again. And, in the case of shallow sea, the keel may become so deep that it hits the seafloor and becomes a grounded object, where further deformation against the ridge can occur either as further building of ice blocks on the pressure ridge or by shear ridging, where floating ice moves along stationary ice (since the ridge is now grounded) (Shokr and Sinha, 2015).

Ice ridging and deformation of this scale represents a danger for marine navigation and offshore structures, since they can create hazardous conditions. Rough ice, especially pressure ridges, along navigational routes delays the marine traffic (see Fig. 2.3) and mechanical loading of deformed ice threatens offshore structures (Shokr and Sinha, 2015). The danger to the ship that a pressure ridge can cause is so severe, especially in the Arctic where ridges can have sails of more than 20 m (Shokr and Sinha, 2015), that navigational manuals directs them to avoid pressure ridges at all costs (e.g. United States Coast Guard, 1953). Hence, with the Baltic being partly covered by sea ice and having a heavy wintertime shipping base, it is of interest to investigate the possibility of detecting pressure ridges to aid navigation.

Figure 2.3: A large (about 3 m tall) ridge that formed in the vicinity of Polarstern. The unconsolidated nature of the ice blocks shows that this ridge formed relatively recently. Courtesy of the eoPortal, image credit: Steven Fons.

The sail heights are referenced to the local sea surface and based on a detection of a local maxima from surface elevation measurements. The local maxima must exceed a specific height, the cut-off height, to be identified as a pressure ridge. No physical criterion to cut-off height has been established, but the choice could be dictated by two external factors: the height must be above the noise level of the data and the ridges should not be mixed with snow drifts (Lewis et al., 1993). For shipping and navigation, to describe the severity

of deformation, some ice services (FIS included) include a deformation numeral called DIR. The definition is not globally defined, but for FIS, DIR ranges from 0 to 5 with the categories: level ice, rafted ice, slightly ridged ice, ridged ice, heavily ridged ice and brash barriers. DIR2 (slightly ridged ice) to DIR5 (brash barriers) are the largest DIR zones and ships cannot penetrate through these without ice breaker assistance (Ronkainen et al., 2018).

2.3 Sea ice and wintertime shipping

As aforementioned (Sect. 1.1), the Baltic Sea belongs to the seasonal sea ice zone. In other words, parts of the Baltic sea freezes during the ice season, either partly or completely (EEA, 2019). During normal winters, the ice cover lasts about 5-7 months in the Bay of Bothnia, 3-5 months in the Bothnian Sea , 0-4 months in the Archipelago Sea, more than 4 months in the Eastern Gulf of Finland and 1-3 months in the Western Gulf of Finland (Furman et al., 2013). According to classification of FIS the Baltic ice season is mild when the extent of ice is below 115 000 km^2, severe when the extent is above 230 000 km^2 and extremely severe when it is above 345 000 km^2 (Ronkainen et al., 2018). To assess measurements of sea ice in the Baltic, it is an obvious choice to look at the area of the Baltic most heavily covered by ice during the ice season; The Bothnian Bay.

Measurements and information on sea ice extent in the Baltic goes back to 1720 and based on (Leppäranta and Myrberg, 2009) a decreasing trend in maximum sea ice extent is seen most of the time since 1800, and the decrease appears to have accelerated since the 1980s (Fig. 2.4). However, it is difficult to demonstrate whether this is statistical significant due to the large interannual variability. The amount of *mild ice winters* of the Baltic sea has increased from 7 in the period 1950-1979 to 16 in the period 1990-2019. The amount of *severe ice winters* decreased from 6 to 1 during the same periods. Due to the expected decrease in sea ice extent, projections of the Baltic Sea ice extent under different emissions

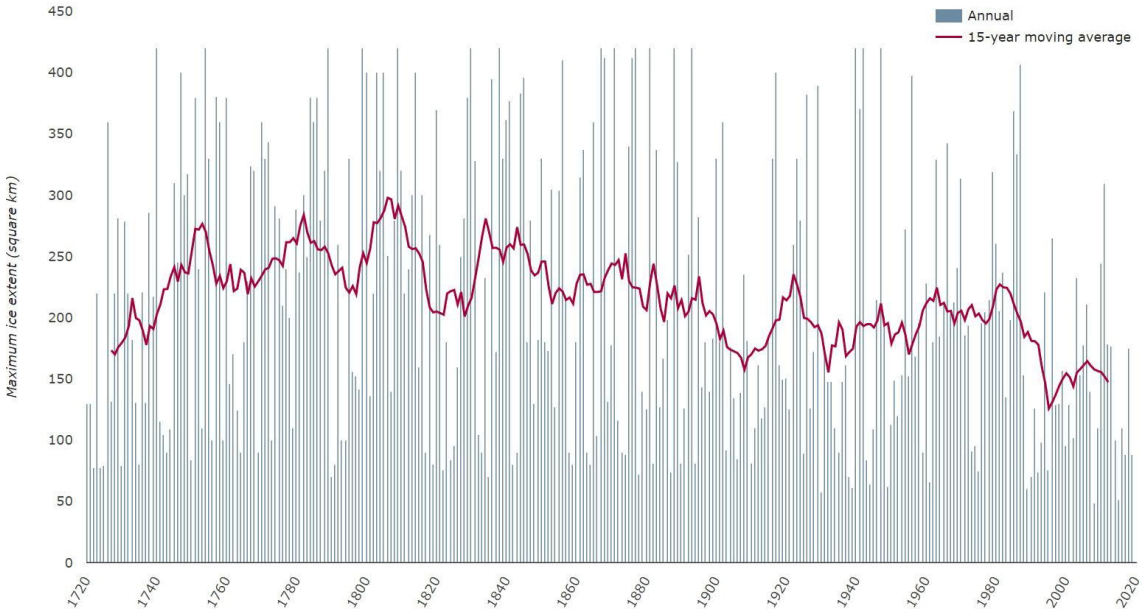

Figure 2.4: Annual maximum sea ice extent in the Baltic sea from 1720 - 2010 with a 15-year moving average (EEA, 2019). Note the somewhat decreasing trend from 1800-2010 (which is yet to be determined if statistical significant or not due to large interannual variability).

scenarios has been assessed. The different projections suggest that the maximum ice cover and ice thickness will continue to shrink significantly during the 21st century (EEA, 2019).

In this study, we will assess ICESat-2 measurements acquired in the winter of 2019. Based on a quick overview from BIM (2019), we will present ice season 2018-2019 of the Baltic. The ice season of 2018-2019 in the Baltic Sea was, according to FIS, a mild winter, categorised primarily according to the maximum ice extent, which from 2018-2019 was 88 000 m^2. Even though the winter was classified mild, it is not equivalent with easy navigation in ice-covered waters, since movement of ice fields often show a greater hazard and hindrance than the extent of the ice cover. The maximum extent was reached on 27 January. Already in late October to early November, the freezing began from inner bays of the northernmost Gulf of Bothnia. However, November and first half of December were warm, resulting in limited freezing. This did not changed until mid-December, where the temperatures dropped below zero and the freezing continued. The new year started out mild, but in mid-January, cold air flowed from the north to Fennoscandia. The cold persisted to the end of January, and the ice area grew rapidly. By January 27, the ice cover extent was 88 000 m^2, which later showed to be the maximum extent of the ice season (BIM, 2019).

February was warmer, two to five degrees warmer than the average, resulting in the ice extent only covering 34 000 km^2 by the end of February. At the beginning of March, northern Europe was covered by an outbreak of a cold polar air mass, resulting in an expanding of the ice covered area due to re-freezing. By March 7th, the area had expanded to 70 000 m^2. The following week experienced similar temperatures, causing the ice cover to remain between 65 000 m^2 to 70 000 m^2. After the spring began and low pressure occurred, the ice area was reduced, and by the end of March, the ice extent was 30 000 m^2. Both April and May were warmer than the average and by May 14th the Baltic Sea was ice free. The entire development during ice season is shown on Fig. 2.5 (BIM, 2019).

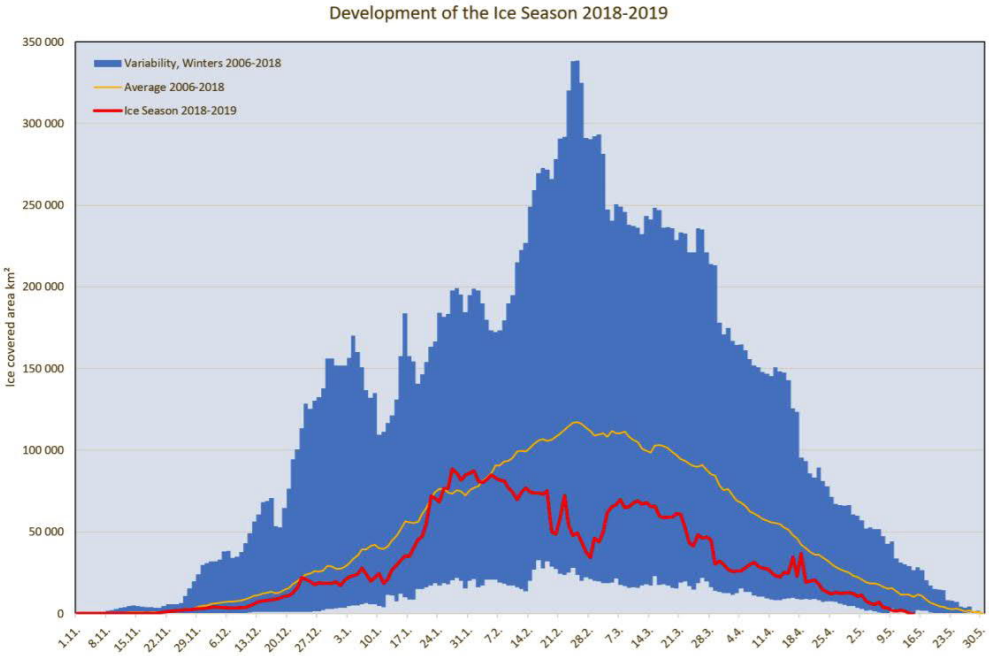

Figure 2.5: Development of ice season 2018-2019 compared to seasons 2006-2018 (BIM, 2019).

2.3.1 Maritime navigation in the ice-covered Baltic

The Baltic Sea is quite busy and thus, safe navigation is a necessity. A direct concern to a navigator is sea ice, since it restricts and often controls the navigators movements. It affects in several ways: forces changes to course and speed; affects piloting by altering appearance of landmarks; hinders establishment and maintenance of aids to navigation; produces changes in surface features and radar returns and much more (Bowditch, 2019). For the Bothnian Bay which is prone to be covered partly or completely by ice, the average ice season lasts from November to May. Therefore, sea ice is an essential factor in this area and every winter, both Finnish and Swedish icebreakers are required to assist ships in the Bay of Bothnia. A mild winters does not necessarily imply easy ship navigation, since it is the ice thickness and amount of ridges that affect navigation the most. Thus, measures to investigate and determine these two factors are important - especially for a country like Finland that relies heavily on export and import by ship (Ronkainen et al., 2018).

Vessel assistance during ice season of 2018-2019

Information of assistance of vessels in the Baltic Sea and specifically the Bay of Bothnia is presented by (BIM, 2019). A total of 3539 vessels received assistance during the 2018-2019 ice season with 1428 of them assisted in the Bay of Bothnia. During the ice season period from 25.12.2018-12.5.2019, there were 218 days of no traffic restrictions and 147 days of traffic restrictions in the Bay of Bothnia, the largest amount in the entire Baltic Sea, presumably caused by the drifting sea ice with heavy ice deformation. Traffic restrictions were initiated on December 17 in the Bothnian Bay and ice-breaking operations began on December 25. Here the icebreaker Otso ordered the start of the year's ice-breaking season. First assistance of merchant vessels was conducted on the 6th of January. The ice breaking season ended the 12th of May with the icebreaker Polaris, which coincidentally was also the last day where assistance restrictions was also in force. The assistance activity had been going on from December 27th to May 5th in the Bothnian Bay (BIM, 2019).

2.4 Shallow waters and water clarity

The Baltic Sea has a mean depth of 54 m (Furman et al., 2013), with 86% of the entire area being shallower than 100 m (Jakobsson et al., 2019), and can be partitioned into 17 open-sea sub-basins according to Baltic Marine Environment Protection Commission – Helsinki Commission (HELCOM) (Fleming-Lehtinen, 2016). Fig. 2.6 shows the depth of the Baltic generated by Fleming-Lehtinen (2016). Here it is clear, that the shallowest areas of the Baltic Sea near the Finnish coast is Archipelago Sea and the Bothnian Bay. In the sense of water clarity, Kattegat and The Sound has the highest Secchi depths, which are measurements often used as water clarity proxy (Hermanni, 2020). Thus, for assessing the bathymetric capabilities of ICESat-2 it would be preferable to look into the clearest and shallowest waters. This results in four main areas of interest to shallow water bathymetry: Kattegat, The Sound, the Archipelago Sea and the Bothnian Bay.

According to Jakobsson et al. (2019), a study of the bathymetric properties in the Baltic Sea based on two digital bathymetric models (EMODnet and IOWTOPO), almost 90% of the accumulated area in the Sound had depths smaller than 25 m. For Kattegat, more than 90% of the accumulated area had depths below 50 m. No specific characteristics were retrieved for the Archipelago Sea alone, only for the Åland Sea and the Archipelago Sea combined, which has significantly higher values (being one of the deepest areas in the Baltic). Nonetheless, for Åland Sea, 80% of the accumulated area had depths smaller

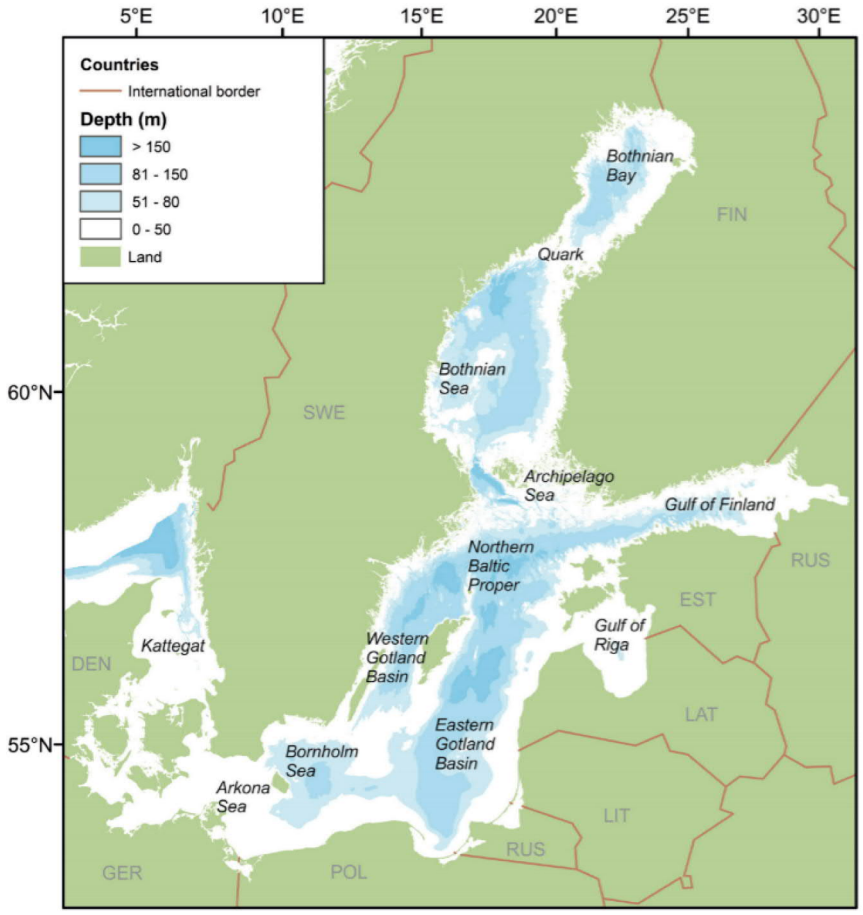

Figure 2.6: The Baltic Sea and its sub-basins. Countries sharing the Baltic Sea shoreline are indicated by acronyms (*EST = Estonia, DEN = Denmark, FIN = Finland, GER = Germany, LAT = Latvia, LIT = Lithuania, POL = Poland, RUS = Russia* and *SWE = Sweden*). The image is produced by shape-files from HELCOM by Fleming-Lehtinen (2016).

than 50 m. The Bothnian Bay had slightly more variance in their depths compared to the abundant shallow values in the other sites. For the Bothnian Bay, about 60% of the accumulated area had depths below 50 m. Based on the analysis of Jakobsson et al. (2019), sub-basin median values denoting the typical depths from the basins have been retrieved. Kattegat had a median of 19 m and the Sound a median of 12 m. Åland Sea has a median of 19 m, even though their mean was 37 m. This is caused by the mean being highly affected by the deeper depths in the Åland Sea compared to the smaller depths in the Archipelago Sea, since the Archipelago Sea was included in their Åland Sea category. The Bothnian Bay had a median depth of 34 m (Jakobsson et al., 2019).

Water clarity is the ability of water to allow for transfer of light. Water clarity has a theoretical maximum of 80 m (Fleming-Lehtinen, 2016). It is highly affected by the presence of dissolved matter or particles in the water, in particular phytoplankton, suspended particulate matter, inorganic compounds and Colored Dissolved Organic Matter (CDOM) (Lund-Hansen, 2004; Preisendorfer, 1986). In waters such as the Baltic Sea, attenuation of water clarity is complex. A proxy for water clarity is the use of Secchi depths, the depth at which a white disk submerged into water is no longer visible (Fleming-Lehtinen, 2016). With Secchi depths being a visual measure, it can be subject to various factors that do not

affect water clarity such as; surface reflectance, elevation of the sun and vessel shadow (Preisendorfer, 1986). Studies have shown that variation in Secchi depth affecting the visibility of the Secchi disk increases with increasing Secchi depth (Aas et al., 2014; Steel and Neuhausser, 2002), which makes the method less accurate in clear waters, such as the Maldives or near the US Virgin Islands compared to murkier waters, such as the Baltic. However, it can be argued that the Secchi depths are subjective and variable in comparison to instrumental measurements as the Secchi depth measurements are made by a human eye (Fleming-Lehtinen, 2016). Nonetheless, Secchi depths can be used as a proxy for water clarity and is useful in this study to investigate not only which sites could prove better for near-shore bathymetric measurements, but also to compare to what extent nearshore bathymetric measurements can be achieved by ICESat-2 as a function of water clarity.

One process that can greatly increase the turbidity of water, a measure of the degree to which water loses its transparency, and the possibility of obtaining near-shore bathymetric measurements from ICESat-2 is *eutrophication*. Eutrophication in the Baltic is thoroughly described in Furman et al. (2013) and briefly introduced in this section. When large quantities of nutrients end up in the water, altering the abundance and species composition of algae and aquatic plants, the water body is said to be suffering from eutrophication. The main driver of eutrophication is antrophogenic nutrients, in the Baltic being primarily affected by internal loading of phosphorus and fixation of atmospheric nitrogen. While eu-

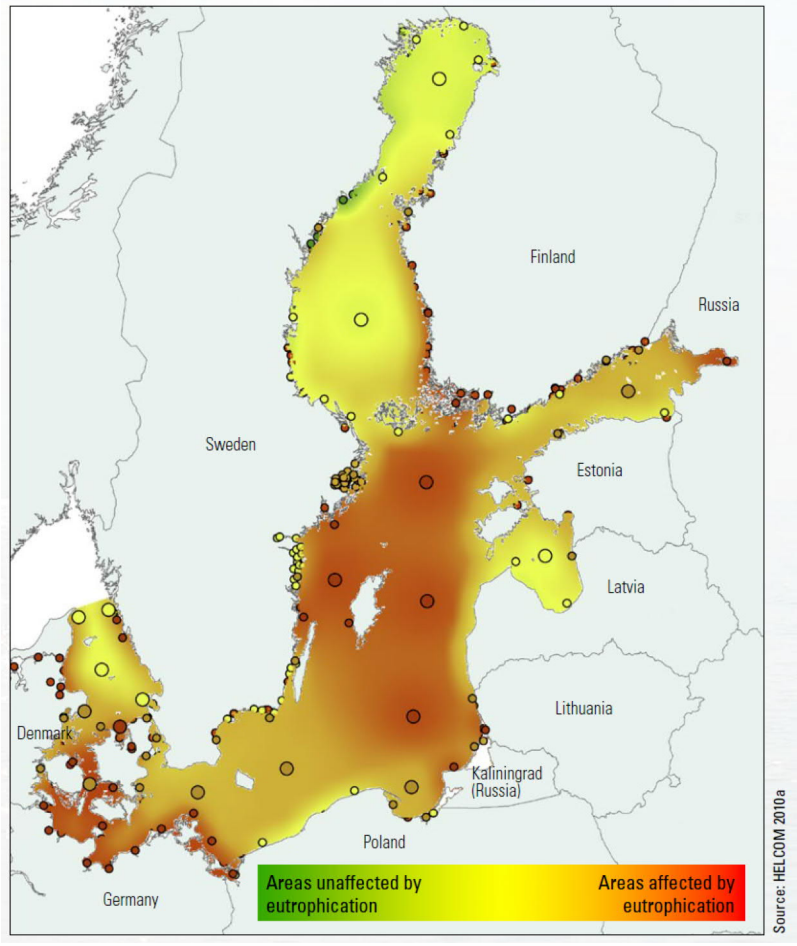

Figure 2.7: Map showing how affected by eutrophication the Baltic is, courtesy of HELCOM.

trophication in its initial state is positive, as the primary production increases allowing for an increase in zooplanktion, benthic fauna and fish catches, as eutrophication progresses the negative effects dominates. The ecosystem becomes disturbed and the faunal community disappears. Some algal blooms become toxic and can prove a health risk to both fish and humans. Furthermore, in the aspect of remote sensing of bathymetry, eutrophication leads to greater turbidity, thus decreased water transparency and clarity. Lastly, the resulting poor oxygen conditions caused by decomposition of algal mats depleting the oxygen allows for more organic material to be deposited on the bottom, which can affect the bathymetric measurements too (Furman et al., 2013).

Overall, most of the Baltic is affected by eutrophication, but extent and severity varies (see Fig. 2.7). Currently, the Bay of Bothnia, some coastal areas in the Sea of Bothnia, The Sound and Kattegat are relatively unaffected by eutrophication, whereas the Gulf of Finland, the northern Baltic Proper and the Danish Straits suffers the most (Fleming-Lehtinen et al., 2020; Furman et al., 2013). Hence, we can assume, for our studies, that eutrophication has not greatly affected Kattegat, The Sound or the Bay of Bothnia. The Archipelago Sea may be to some extent affected (see Fig. 2.7). For future work, eutrophication should be considered when investigating other coastal areas highly affected by eutrophication such as coastal areas of the Baltic Proper, when investigating bathymetry from ICESat-2..

3 Satellite altimetry

This section introduces satellite altimetry by first describing former laser altimetry studies and what lead to the follow-on mission ICESat-2. Thereafter, the measurement principle of satellite altimetry is described and the most important differences between radar and laser altimetry is highlighted. An introduction to ICESat-2 is provided and a short explanation of geophysical corrections needed in satellite altimetry is presented. Finally, the theory behind retrieving bathymetry from laser is presented.

3.1 Prior applications of laser altimetry

Measurements of sea ice thickness from space has been around since 1991 with The European Space Agency (ESA)'s radar altimeter European Remote sensing Satellite-1 (ERS-1) (ESA, 2020; Tilling et al., 2020). Altimetry on sea ice can be done by both radar altimetry and laser altimetry (Skourup, 2010). Since laser altimeters has the possibility to measure with precision down to centimetre range, it is especially interesting to employ ranging lasers in the polar regions to estimate sea ice thickness (Abdalati et al., 2010). Thus, the ICESat mission was designed. The following overview is described more thoroughly in Abdalati et al. (2010) and Markus et al. (2017).

On January 12, 2003, National Aeronautics and Administration (NASA) launched ICESat as part of NASA's Earth Observing System. ICESat was the first satellite mission explicitly designed to measure changes in polar ice. The main objective of ICESat was to observe changes in the ice sheet elevation with great spatial detail to quantify the growth and shrinkage of an ice sheet, and subsequently estimate the ice sheet mass balance and contribution to sea level. Thus, by combining state-of-the-art laser ranging capabilities, precise orbit and attitude control and knowledge of the different processes occurring, it was deemed possible that ICESat could provide very accurate measurement of ice sheet topography and elevation changes at high spatial resolution.

The high spatial resolution and accurate measurements was achieved by ICESat by sampling over $\sim$65 cm-diameter footprints at every 172 m. The precision and accuracy of elevation retrieval was $\sim$2 cm and $\sim$14 cm pr shot, respectively. The ICESat observatory carried the Geoscience Laser Altimeter System (GLAS), the mission's primary instrument, which consisted of three NIR (1064 nm) lasers. Along-side GLAS was a frequency-doubler in the beam path that converted a portion of the NIR (1064 nm) to green (532 nm). This was to enable more accurate atmospheric measurements since detectors at green wavelengths are more sensitive to those than the NIR. Due to on-orbit anomalies resulting in the premature failure of one of the lasers, a revised strategy was urgent. The revised strategy allowed for the mission to meets its overall ice sheet change detection objectives at the expense of less temporal and spatial detail than originally designed. Despite the comprised operation, ICESat demonstrated an astounding capability of not only assessing changes in ice sheet elevations, but for multidisciplinary applications including sea ice freeboard (and thickness), vegetation height and localised surface deformation. It was with these demonstrated capabilities coupled with the observations of extreme changes in the polar ice regions, that lead to call for an ICESat follow on mis-

sion resulting in the ICESat-2 mission that by advances in laser technology and learning outcomes lead to the novel design and measurement strategy.

3.2 Basic measurements principles

The basic principle of laser altimetry is very simple (see Fig. 3.1): an electromagnetic pulse is emitted from the altimeter towards the surface of the Earth, reflected and returned to the altimeter, where the two-way travel time of the pulse is determined. From the two-way travel time it is possible to determine the altitude of the satellite from the surface, the range (h_{range}). The range is referred to as one half the signal pulse round-trip time (round-trip time is defined as the time it takes for the pulse to be transmitted, reflected at the surface and received again) times the speed of light as follows (Neumann et al., 2019a):

$$h_{range} = \frac{c\,(t_t - t_r)}{2}, \tag{3.1}$$

where c represents the speed of light; t_t represents the time the pulse is transmitted; and t_r represents the time the pulse is received again.

The height of the surface, using the World Geodetic System 1984 (WGS84) ellipsoid as reference surface, is conceptualised as the difference between the height of the satellite with reference to the WGS84 ellipsoid, and the height from the satellite to the surface (Skourup, 2010);

$$h_{sh} = h_{ellipsoid} - h_{range}, \tag{3.2}$$

where h_{sh} represents the surface height with respect to WGS84 ellipsoid; $h_{ellipsoid}$ represents the heights from the satellite to the WGS84 ellipsoid determined by Precise Orbit Determination (POD) and Precise Pointing Determination (PPD); and h_{range} is the dis-

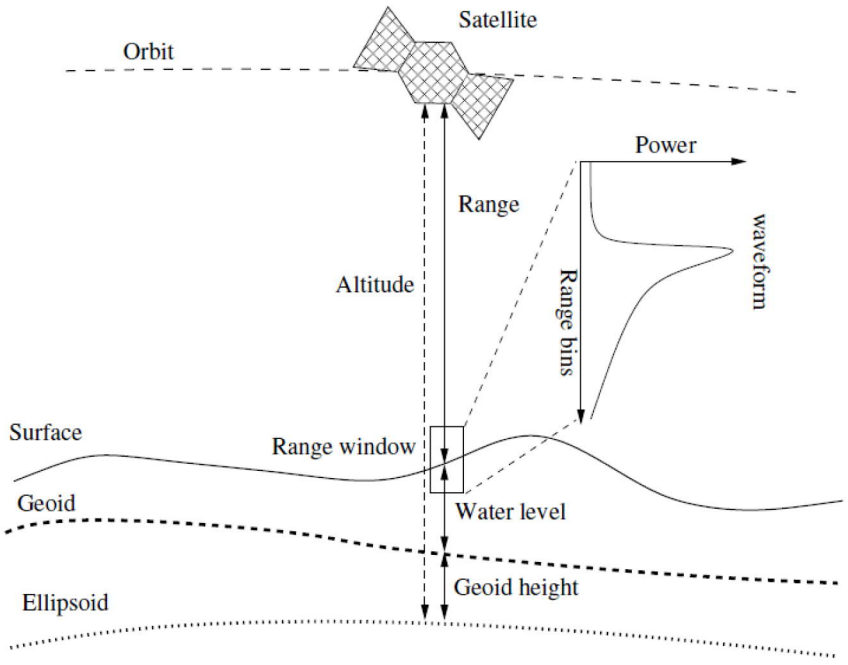

Figure 3.1: The principle of satellite altimetry, courtesy of Nielsen et al. (2017).

tance from satellite to surface return of the pulse. POD and PPD are determined by high precision on-board instruments.

In general, the height of the sea surface (h_{ssh}) is retrieved by (Skourup, 2010);

$$h_{ssh} = h_{geoid} + h_{DT} + h_{IB} + h_{tides} + h_{errors}, \tag{3.3}$$

where h_{geoid} describes the equipotential surface of the Earth; h_{DT} is the dynamic topography associated with large scale ocean circulation; h_{IB} describes the inverse barometric effect caused by atmospheric loading; h_{tides} denotes the different tides affecting the measurements; and model inaccuracies are given by h_{errors}. The definition of h_{ssh} also denotes some of the geophysical corrections needed to apply. For sea ice, the ellipsoidal surface height (h_{sh}) is the sum of the sea surface height (h_{ssh}) and the sea ice freeboard height (h_f), i.e. the height of the ice above sea level, such as (Skourup, 2010);

$$h_{sh} = h_{ssh} + h_f. \tag{3.4}$$

Thus, it is important to apply proper geophysical corrections to the range height in order to properly determine h_{sh}. Having determined the surface heights one must determine a reference for the local sea surface heights in ice covered water to redeem the freeboard heights (Skourup, 2010). For altimeters, this is usually based on the location of leads, small open water areas with calm water or newly formed ice, in the ice cover. Leads have clear signals (high energy return) in conventional radar altimetry and can quite simply be extracted from the data (Wernecke and Kaleschke, 2015). Leads in photon clouds, such as from ICESat-2, are different measures and determined differently (Neumann et al., 2019a).

3.3 Specifications of laser altimetry

In regular laser (and radar) altimetry, the altimeter measures the strength and shape of the return signal, and the shape of the return signal from one pulse as a function of time called the waveform. The waveform is defined by the characteristics of the footprint area; the surface height; reflectivity distribution; transmitted pulse shape; forward scattering in the atmosphere; and the receiver characteristics. The measurement geometry for laser altimeters are quite different compared to radar altimeters. Conventional laser altimeters generally have a narrower beam width, resulting in a quite small footprint area. This is e.g. believed to better detect larger open leads directly by relative changes in the elevation (Skourup, 2010). This was the way that GLAS worked, but this approach has been changed to a novel photon-counting measurement strategy to accommodate the new mission objectives of ICESat-2 (Markus et al., 2017; Neumann et al., 2019a).

The greatest difference between laser and radar altimetry is the that radar can measure through all atmospheric conditions, but laser altimetry is not capable of penetrating through cloud cover and is usually reflected by the first surface the pulse encounters (Skourup, 2010). However, laser altimetry is not as affected by slope-induced errors as radar altimetry due to the smaller laser footprint compared to the radar footprint (Brenner et al., 2007).

3.4 The Ice, Cloud and Land Elevation Satellite-2 (ICESat-2)

This section is based on descriptions, explanations and findings from Markus et al. (2017) and Abdalati et al. (2010). Specifications of the main instrument described in Sect. 3.4.1

are based on a combination of Markus et al. (2017), Abdalati et al. (2010), Neumann et al. (2019b), Neumann et al. (2019a), NSIDC (2020a) and NASA (2020b), and are presented as a overview of their findings combined.

NASA launched ICESat-2 on 15 September 2018 to continue the measurements of current changes in land ice elevation, sea-ice freeboard heights and vegetation canopy height as a follow-on mission building on the heritage of ICESat. While ICESat provided accurate and high resolution data of both ice sheet elevation, sea ice freeboard heights and canopy heights, one major complication was the inability to separate slope effects from true elevations. The greatest elevation change occurs along the margins of Greenland and Antarctica, but the single beam laser configuration of ICESat did not allow for deconvolving elevation change from surface slope and surface roughness. Thus, the ability to separate slope effects from true elevations was a critical improvement required in a follow on mission along side the improved spatial resolution (Abdalati et al., 2010).

To investigate both sea ice thickness, ice sheet elevations and canopy heights in proper spatial and temporal resolution, two different measuring strategies are employed: one for the polar regions and one for the land areas. ICESat has a 91-day exact repeat orbit, with a monthly sub-cycle for polar regions and oceans. It was deemed necessary to produce monthly sea ice thickness maps to better understand freeze and melt processes and to delineate dynamic versus thermodynamic sea ice thickening. Furthermore, ICESat-2 leads an operational off-nadir pointing over land areas which generates a dense grid of data over the course of two years. The land area measurements will contribute to the generation of global carbon inventory assessment, which is critical for understanding the global carbon budget. The observing strategies are relative to the area ICESat-2 is measuring; nadir pointing at polar areas for ice measurements and off-pointing over vegetation, land and hydrology measurements (Fig. 3.2). ICESat-2's orbit has the inclination of 92° allowing for measurements up to 88° north and south (Abdalati et al., 2010).

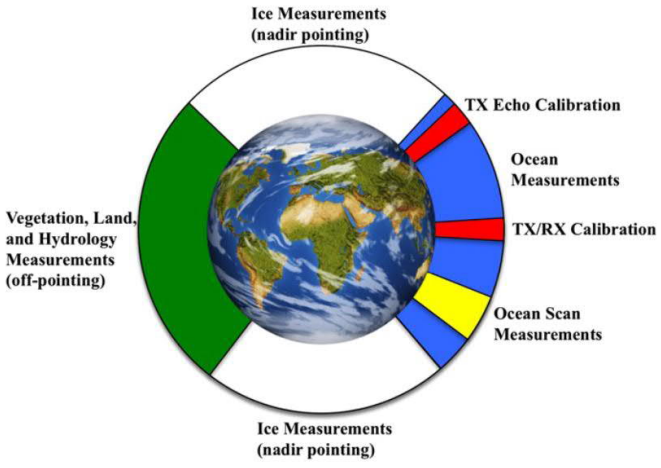

Figure 3.2: Conceptual mission operations plan of ICESat-2 (Markus et al., 2017).

Even with ICESat's great success, several limitations were identified by the science community. These included, in particular, the ability to determine changes in the cryosphere. Thus, changes to the requirements, needs and design were discussed for the follow-on mission. It was decided that the scope of the follow-on mission was to be expanded into

including not only ice sheet changes, but also high resolution measurements of sea ice freeboards and vegetation canopy heights, as ICESat had already shown great potential of determining these parameters. The science objectives as presented by Markus et al. (2017):

1. Quantify polar ice-sheet contributions to current and recent sea-level change and the linkage to climate conditions;
2. Quantify regional signatures of ice-sheet changes to assess mechanisms driving those changes and improve predictive ice sheet models; this includes quantifying the regional evolution of ice sheet change, such as how changes at outlet glacier termini propagate inward;
3. Estimate sea ice thickness to examine ice/ocean/atmosphere exchanges of energy, mass and moisture;
4. Measure vegetation canopy heights as a basis for estimating large-scale biomass and biomass change.

To allow for the science objectives to be achieved, major changes to the design of the main instrument was implemented. One of the greatest and most interesting changes was the transition from a single-pulse, full-waveform design as GLAS used to a spaceborne photon-counting laser altimeter as the main instrument (Markus et al., 2017).

3.4.1 Advanced Topographic Laser Altimeter System (ATLAS)

The main instrument on board ICESat-2 is ATLAS. Where altimeters usually sends out a pulse and tracks the travel time for the pulse to reach from the instrument down to Earth and back with the power of the returned signal resulting in a shape called the waveform, ATLAS uses a novel photon-counting approach to overcome the limitations of the GLAS instrument on board ICESat. Here, ATLAS sends out a laser pulse that is reflected at the Earth's surface and then ATLAS measures time-of-flight of the reflected photons of the laser pulse as the return signal. Each individual detected photon will be time-tagged and geolocated, which connected with the ellipsoidal height is converted into a surface elevation measurement. This photon-counting approach results in a much denser surface elevation result than full-waveform detections used by ICESat (Markus et al., 2017; Neumann et al., 2019b).

ATLAS utilises a single-photon low-pulse energy green (532 nm) laser pulse with a Pulse Repetition Frequency (PRF) of 10 kHz. It has a footprint diameter of $\sim$17 m at average orbit altitude of 500 km. The low energy pulse and high repetition rate allows a 0.7 m separation for each laser pulse on the surface, which is highly ideal for rough terrains such as glaciers or Sea Surface Height (SSH) observations where minimal gaps in along-track is preferred. Furthermore, ATLAS supports overlaps in across-track by the novel multi-beam configuration (see Fig. 3.3) relevant for estimating change determination independent of surface slope, on of the most important improvements since ICESat. The single-photon sensitive detection strategy developed allows for individual photon Time of Flight (TOF) to be determined with a precision of 800 μm. The combination of the small footprint size with the TOF and PRF requirements ensure that surface heights measurements within sea ice leads to a vertical precision of 3 cm. ATLAS splits a single output laser pulse into six beams that are arranged in three pairs of beams. Left/right spots are approximately 90 m

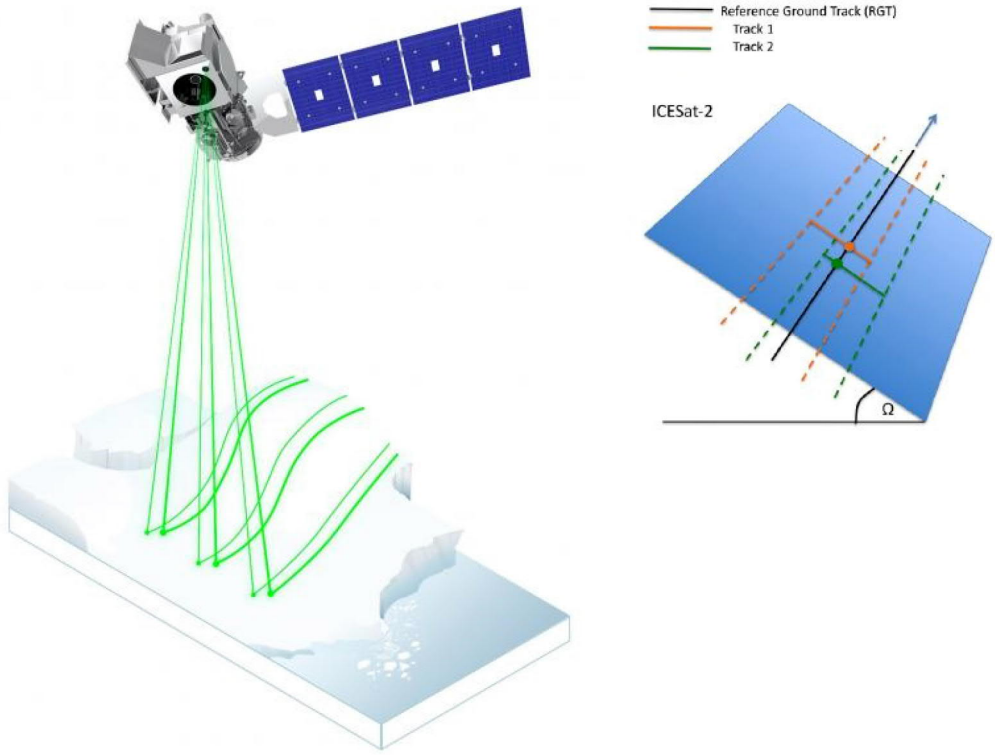

Figure 3.3: Multi-beam configuration of ATLAS: (left) ATLAS multi-beam configuration shown with its green laser split into 6 beams that are separated into 3 beam pairs (in an array of 3 x 2) (NASA, 2020a). (right) cross-track overlaps to support surface estimation independent of surface slopes. One of the new and important updates since ICESat (Markus et al., 2017).

apart in across-track direction and 2.5 km in along-track direction, see Fig. 3.4 (Neumann et al., 2019a; NSIDC, 2020a).

The beam pairs are separated by ∼3 km across-track. Each pair comprise a weak beam and a strong beam, in other words; each beam pair have different transmit energies. The energy ratio between the weak and strong beam is 1:4, thus the strong beam is ∼4 times stronger than the weak. This configuration was designed to enhance radiometric dynamic range to accommodate the different energy levels required to meet the scientific objectives (Neumann et al., 2019a,b; NSIDC, 2020a).

It is expected that only strong beams will be the primary means for ranging to low-reflectivity targets such as oceans and at times vegetation, while both strong and weak beams will provide altimetric ranging over bright surfaces such as sea ice and ice sheets. The footprint pattern created by the laser beams of ATLAS intersecting with the Earth's surface is shown in Fig. 3.4. Approximately twice a year, the ICESat-2 observatory will be reoriented to maximise sun illumination on the solar arrays causing the orientation of the footprint pattern to change. If ATLAS is forward oriented ($+x$), the weak beams are leading the strong beams and the weak beams are on the left side of the ground track. When ATLAS change to backward orientation ($-x$) the relative orientation of the beams change. Thus, the strong beams will lead the weak beams and be located on the left side of the ground track. This is essential, as the ground tracks in data product ATL03 (and consequently in the higher

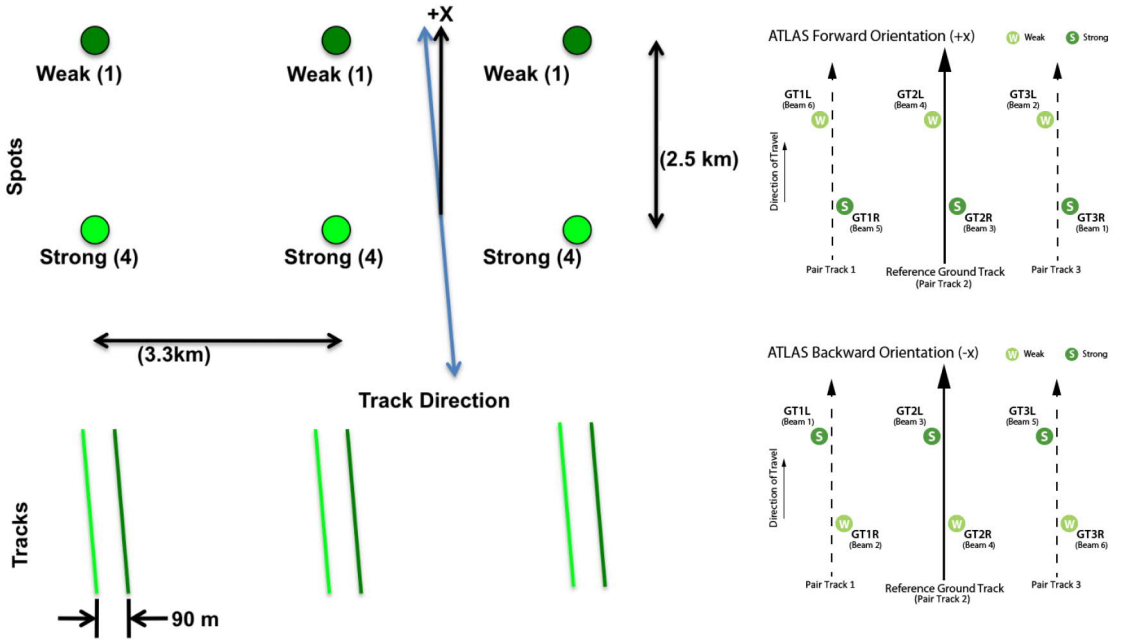

Figure 3.4: ATLAS multi-beam configuration. (Left) Configuration showing distance between the beam pairs (Markus et al., 2017), (right) Forward and backward orientation of ATLAS and the location of strong and weak beams changing due to the biannual change of orientation (NSIDC, 2020a).

level data products) are defined from left to right in the direction of travel (Ground Track (GT) 1L, GT 1R, GT 2L, GT 2R etc.) and the implementation of the changing orientation is managed through an observatory orientation parameter. For GTs in data there will be 7 parameters: six tracks for each of the beams and one track, the Reference Ground Track (RGT), showing an imaginary line through the six-beam pattern useful for getting an idea of how the tracks are distributed over the surface (NASA, 2020b; Neumann et al., 2019a,b; NSIDC, 2020a).

Before time-tagging and geolocating of each individual photon, an on-board filtration is computed. Since ATLAS measures photons entering the receiver, it not only measures reflected photons from the surface but also photons from e.g. sun reflection. The on-board software's purpose is to limit the amount of time-tagged photon events and reduce the overall data volume down-linked as the total measurements already result in vast data volume. The software includes a Digital Elevation Model (DEM), an estimate of surface relief and a surface classification mask which will constrain the time tags to the photons most likely reflected by the Earth's surface. This process is referred to as a Range Window. Furthermore, the photon time tags are reduced by statistically determining photon events most likely reflected from the Earth's surface by applying histogram window to the photon time tags. The amount of photon time tags down-linked to ground (called the Telemetry Band) varies from 3 km over rugged mountain topography to $\sim$40 m, and the Telemetry Band is re-evaluated every 200 pulses (Neumann et al., 2019b).

3.5 Geophysical corrections

In general, when a pulse travels through the atmosphere it will experience delay depending on the refractive index along the optical path. Ultimately, the pulse will encounter a surface on Earth (either ocean, land or snow/ice) and be reflected back towards the spacecraft.

The two-way-travel time is measured by a altimeter and converted into a range (Eq. 3.1), which can later be converted to ellipsoidal heights (Eq. 3.2). However, depending on the surface the pulse encounters, several corrections must be applied. Over oceans, sea ice and ice shelves the pulse must typically be corrected for temporal variability in atmospheric-oceanic interactions. This includes the inverted barometer effect, tidal effects and other corrections. Over terrestrial surfaces, each photon must be corrected for solid earth tides and ocean loading. All these corrections constitute what is referred to as *geophysical corrections* (Neumann et al., 2019a). A short summary of the relevant geophysical corrections related to altimetric elevation measurements, specifically for ICESat-2, is provided in Tab 3.1

For the geolocated photons from ICESat-2, a set of corrections have already been applied (C1-C6, see Table 3.1) in the Level-2A data product ATL03. Those geophysical corrections include solid Earth tides, ocean loading ocean pole tide and geocenter motion amongst other. For the elevation computation by ATLAS, the photon heights (H_{gc}) are computed as follows (Neumann et al., 2019a):

$$H_{gc} = H_P - H_{OL} - H_{SEPT} - H_{OPT} - H_{SET} - H_{TCA}, \tag{3.5}$$

where H_P is the photon event height; H_{OL} is the ocean loading deformations; H_{SEPT} is solid Earth tides; H_{OPT} is ocean pole tides; H_{SET} is solid Earth tides; and H_{TCA} is the

Table 3.1: Relevant geophysical corrections for altimetric elevations from ICESat-2 given by correction type, order of magnitude and brief description of each correction (Neumann et al., 2019a)

#	Abbreviation	Name	Size	Description
C1	SEA	Solid Earth Tides	±40 cm	Deformation, as elastic response, to the solid Earth due to attractions from Sun and Moon
C2	OL	Ocean Loading	Of cm size	Deformation of the Earth's crust to the weight of overlying oceanic tides
C3	SEPT	Solid Earth Pole Tide	±1.5 cm	Deformation due to centrifugal effect from small variations in polar motion
C4	OPT	Ocean Pole Tide	±2 mm	Oceanic height correction due to centrifugal effect from small variations in polar motion
C5	GM	Geocenter Motion	3 to 5 mm	Accounted for in POD in both X, Y and Z direction. Largely reflects global scale mass re-distributions in atmosphere and oceans
C6	TCAD	Total Column Atmospheric Delay	−2.6 to −0.9 m	Path delay of pulse through the neutral atmosphere, dependent on pressure, water vapour and air temperature. Depends on state of atmosphere
C7	G	Geoid	−105 to +90 m	An equipotential surface of the Earth, describes the shape the ocean surface would take affected only by gravity and rotation. Modelled by EGM2008.
C8	OT	Ocean Tides	±5 m	Ocean tides can vary significantly over short times and in height as well. Here it includes diurnal, semi-diurnal and longer period tides. Modelled by GOT4.8 including long period equilibrium tides
C9	DAC	Dynamic Atmospheric Correction	±50 cm	Describes the oceanic level response to variations in atmospheric pressure and the mass momentum forcing driven by wind stress field. Includes the inverted barometer effect. Modelled by Aviso MOG2D

total column atmospheric delay. Corrections C7-C9 (see Table 3.1) are given at a reference photon value interval (at every 20 m) and can be applied by the user to reference the photons to the geoid. All of the corrections are also given in the data set if the user needs them to either extract or remove the already applied corrections from the retrieved photons (Neumann et al., 2019b; NSIDC, 2020a).

A conventional correction applied to measurements over sea ice, is to remove values within a range of a few metres from the Mean Sea Surface (MSS) (e.g. Kwok et al., 2019a; Rinne, 2020a). MSS is given by (Skourup et al., 2007):

$$MSS = N + MDT, \tag{3.6}$$

where N is the marine geoid heights and MDT is the mean dynamic topography. Usually,

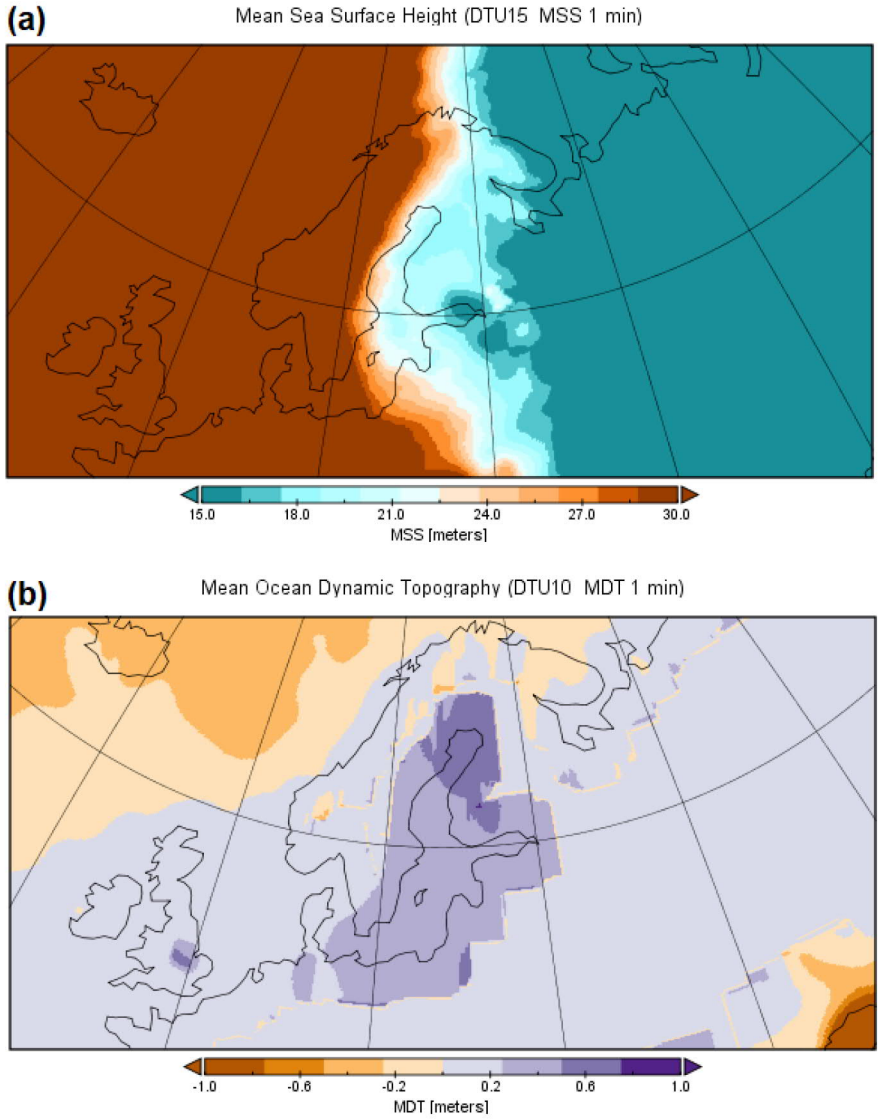

Figure 3.5: Mean Sea Surface (MSS) and Mean Dynamic Topography (MDT) of the Baltic. (a) MSS estimated by Global DTU 2015 MSS Model (available on https://www.space.dtu.dk/english/research/scientific_data_and_models/global_mean_sea_surface in 1 min x 1 min grid) and (b) MDT estiamte by Global DTU 2010 Model (available on https://www.space.dtu.dk/english/Research/Scientific_data_and_models/Global_Mean_Dynamic_topography in 1 min x 1 min grid)

the Baltic (specifically the Bothnian Bay), MSS ranges from around 18-23 m and Mean Dynamic Topography (MDT) around 0.5-0.8 m based on visual inspection of Fig. 3.5. The corrections needed by the user to be applied are C7-C9. While these corrections allows us to reference the photons to the geoid (C7, usually the largest signal that affects them), the ocean tides (C8) and dynamic atmospheric correction (C9) can also be applied. However, applying these does not make the photons in reference to MSS, but rather to the geoid.

Through an inspection of all retrieved geophysical corrections used in this study from ICESat-2 (Fig. 3.6), we see that the C8 correction ranges from -0.02 m to 0.05 m (Fig. 3.6b) and the C9 correction ranges from -0.2 m to 0.5 m (Fig. 3.6c). This means, in general, these two additional corrections adds up a range of -0.22 m to 0.55 m to be corrected for on top of the geoid which already ranges from 17-22 m (Fig. 3.6a, similar to the MSS). This means, that combining C7-C9 and subtracting these from the photon ellipsoidal heights makes the photons in reference to the geoid, but the additional corrections (C8-C9) are within the same range as MDT. This suggests, that a threshold of ± 3 m from MSS, which is commonly used for sea ice (private communication, Rinne, 2020b), is valid even if the photons are not directly referenced to MSS, but rather the geoid, since we do not correct the

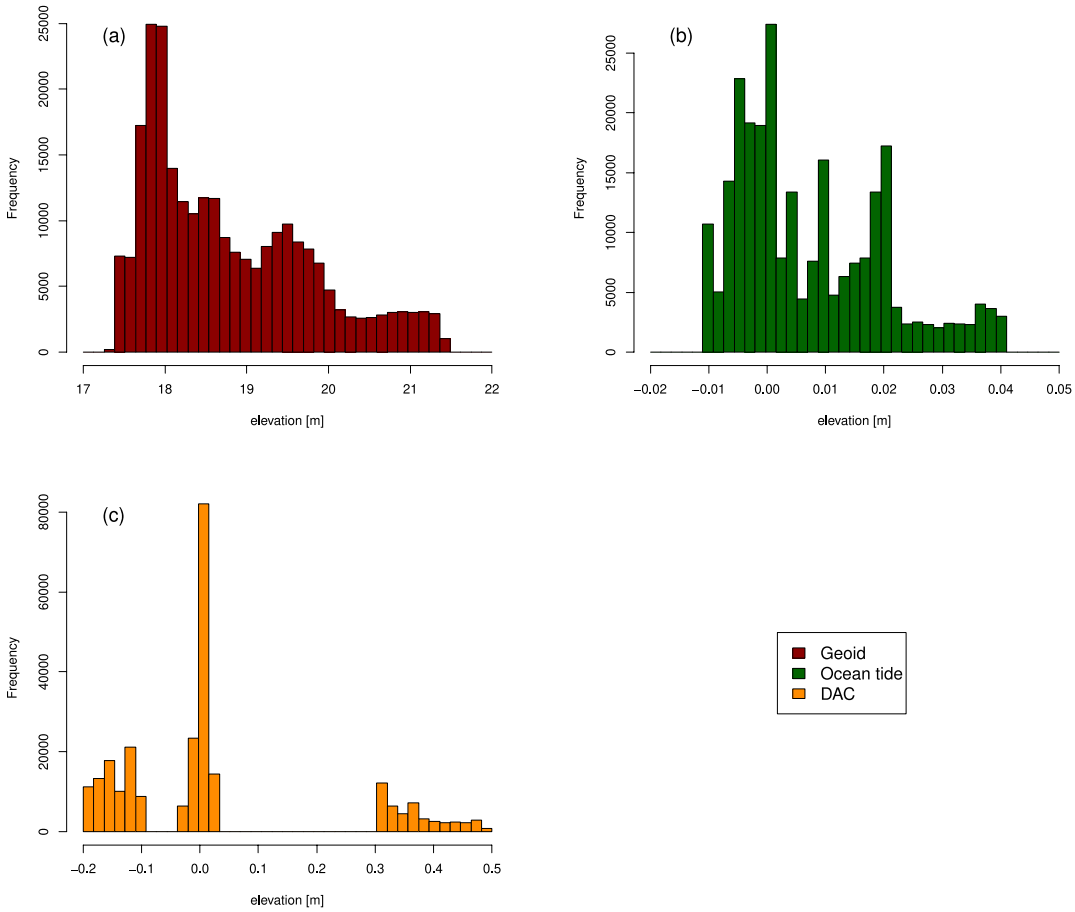

Figure 3.6: Distribution of geophysical corrections available in ATL03 data and used in this study (tracks from 1 February 2019, 17 February 2019, 23 March 2019 and 27 March 2019). (a) Geoid undulations ranging from 17 m to 23 m, (b) Ocean tides ranging from -0.02 m to 0.05 m and (c) Dynamic Atmospheric Correction (DAC) corrections ranging from -0.2 m to 0.5 m.

photons by adding an external model for MSS. In extreme cases, since generally it seems like the corrections retrieved from ATL03 are slightly lower than generally expected MSS values, we could loose some of the highest values, but since the ridge sails in the Bothnian Bay is rarely above 0.5-0.6 m on average (e.g. Gegiuc et al., 2018; Lewis et al., 1993), we do not assume there to be a significant loss of relevant information, if even any loss.

3.6 Airborne LIDAR bathymetry

Conventional bathymetric Light Detection And Ranging (LIDAR) systems are primarily built to gather nearshore bathymetry and has it roots in the mid-1960s (Forfinski-Sarkozi and Parrish, 2016; Quadros et al., 2008). In comparison with topographic lasers, that utilises a Near Infra-Red NIR laser (1064 nm) which is not able to penetrate water, airborne bathymetric lasers usually employ both a green laser (532 nm, able to penetrate water) and a NIR laser (1064 nm, for water surface measurements), see Fig. 3.7 (Quadros et al., 2008). The measured reflection of the NIR light provides the height from the water surface to the plane (for an airborne measurement), and the reflection of the green light is assumed to be the height from the sea floor, after having travelled through the water column. Travelling through the water column submits the green laser to absorption, scattering and refraction,

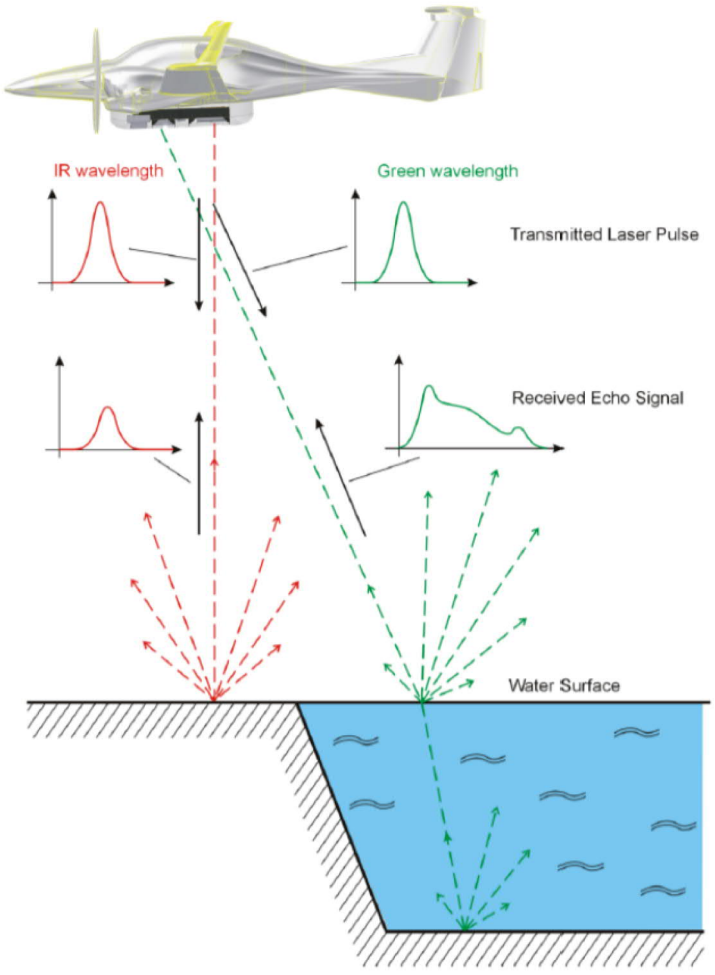

Figure 3.7: Combination of topographic (NIR, 1064 nm) laser and bathymetric (green, 532 nm) laser, courtesy of Mandlburger et al. (2011).

thus attenuating the laser return energy and limiting the depth of the water that can be measured (Quadros et al., 2008). The maximum depth a Airborne LIDAR Bathymetry (ALB) is able to measure is influenced by the interaction of the sea-bottom, water turbidity, incident sun angle and intensity (Irish and White, 1998). Ideal circumstances allows for ALB measurements up to 60 m (Wozencraft and Millar, 2005), but the circumstances and conditions are rarely that ideal. Applying the refraction corrections to the bathymetric measurements allows for corrected, seafloor detections to be made.

As ATLAS utilises a photon-counting approach, the amount of photons corresponding to the seafloor returns (n_{bot}) can be evaluated by utilising a modified version of the LIDAR equation (Quadros et al., 2008):

$$n_{bot} = \eta_q \eta_t \eta_r \frac{E_t}{hv} \rho_\lambda (\alpha_t) \frac{A_r}{\pi (R_{air} + R_w)^2} (1 - r_{int}(\alpha_s))^2 T_\lambda^2 e^{-2c_\lambda R_w}, \tag{3.7}$$

where h is Planck's constant; v is the photon frequency; R_w is the pulse travel distance in water; R_{air} is the pulse travel distance in air; η_q is the detector quantum efficiency; η_t is the transmitter optical efficiency; η_r is the receiver optical efficiency; E_t is the transmitted energy per channel per pulse; ρ_λ is the bottom reflectance at the laser wavelength, λ; α_t is the incidence angle on the bottom; A_r is the collecting area of receiver aperture; r_{int} is the air-water interface reflectance; T_λ^2 is the two-way atmospheric transmittance; α_s is the local incidence angle on water surface; and c_λ is the effective attenuation coefficient.

The geolocation process of the photons (to be described more thoroughly in Sect. 4.3.1), does not take into account the refraction and corresponding change in the speed occurring at the water-air interface, already mentioned as a relevant factor in Eq. 3.7. Consequently, both vertical and horizontal errors are introduced in the geolocated photons, which results in geolocated photons that appear deeper and further off-nadir than true measurements (Parrish et al., 2019). The impact of geolocation is shown in Fig. 3.8.

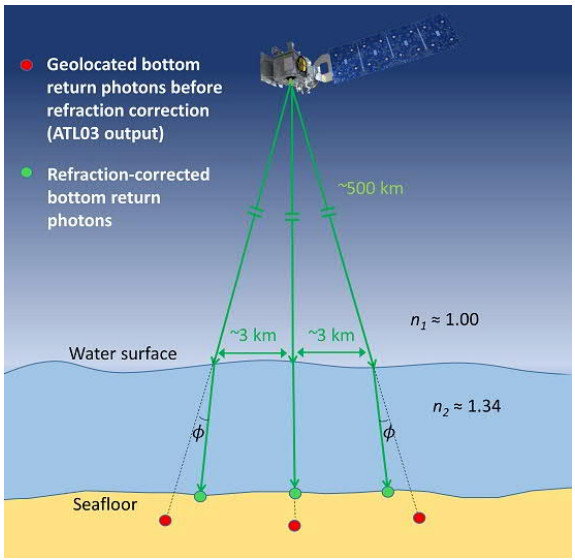

Figure 3.8: Illustration of the need for refraction correction, courtesy of Parrish et al. (2019). Axes are defined as X (out of the page) is along-track direction, Y across-track direction and Z is up. For simplicity only one strong beam is pictured. Red dots represent the uncorrected photon locations, while green dots shown the correct locations after refraction corrections. Off-nadir angles are greatly exaggerated in image.

This study does not correct for the water-air interface or the change of speed when the pulse travels through the water column, however it is necessary to correct for refraction in future work to obtain reliable bathymetric measurements. Here, we refer to Parrish et al. (2019) for an geometric understanding and explanation of the refraction corrections to be applied. Their method is based on manual extraction of water surface photons and bathymetric photons from ATLAS. This is a very tedious process and hence it has not been applied in this dissertation. We will however provide a proof-of-concept of nearshore bathymetry measurements and explain to what extend shallow water bathymetry can be retrieved in the Baltic from non-corrected photons. In addition, we describe considerations and provide recommendations for future work for using the geolocated photons to estimate bathymetry.

4 Study area and data description

In this section, the study area for investigating sea ice and shallow water bathymetry in the Baltic is presented. In addition, a description of the data sets used in this work is provided.

4.1 Ice ridging in the Bothnian Bay

In this study we investigate sea ice ridging in the Bothnian Bay, the northernmost basin in the Baltic, see Fig. 4.1. The Bay of Bothnia is a semi-enclosed basin with length of approximately 300 km, a width of 100-150 km, and an area of about 36 000 km^2 (Leppäranta and Myrberg, 2009). The Bay of Bothnia has during the last 100 years always frozen completely over except the extremely mild winters of 2014-2015 and probably also 1929-1930 (Uotila et al., 2015), but usually freezes completely even during mild winters (Dyrcz, 2017). The bay's shores are covered by fast ice during winter, its width varying with the archipelago. In the fast ice zone the ice grows thermodynamically, since the ice is attached to the coast and does not move. Along the coast of the Bothnian Bay there is a large area that allows fast ice to form every winter. Depending on the ice thickness, the boundary of the fast ice zone is located where the depth is 5-15 m. In the drift ice zone, ice floes move with the currents and winds and can pile up to ridges, extending several meters in height. Thus, ice growing in the drift ice zone consists of both thermodynamic

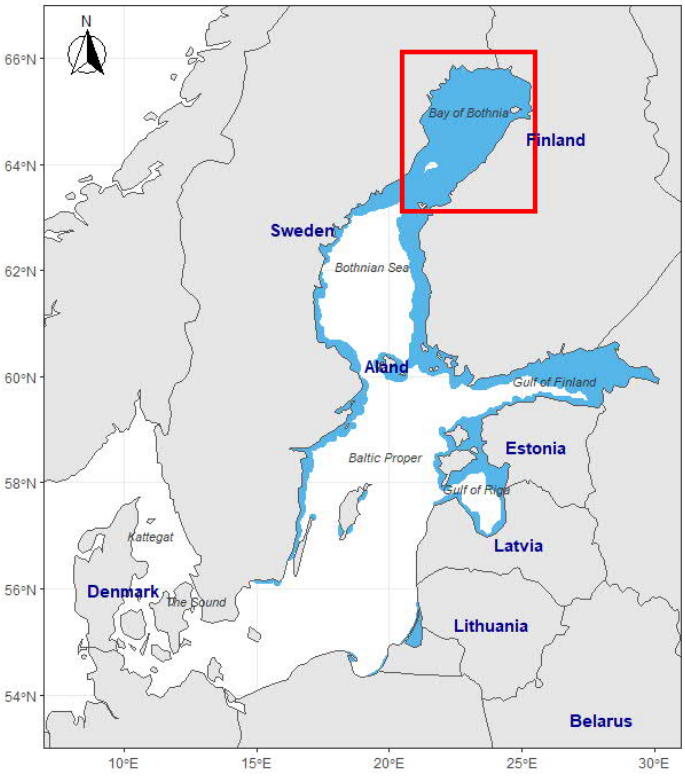

Figure 4.1: Study area for sea ice ridging. Red box shows the approximate study area extent, which in this case covers the Bay of Bothnia. Blue indicates the maximum ice extent of this season, reached on 27 January, retrieved from FIS ice charts.

and dynamic processes (Leppäranta and Myrberg, 2009; Ronkainen et al., 2018). In the northern Bay of Bothnia the sea ice thickness ranges from 15-40 cm in thickness and can be classified as either thick fast ice or very close drift ice depending on location. In the southern Bay of Bothnia the sea ice is primarily classified as thin ice and new ice in the inner archipelago (Eriksson et al., 2018; FMI, 2020).

With the launch of ICESat-2 in 2018, it provided its first ice measurements during ice season 2018-2019. We will utilises these measurements to investigate the ridging of sea ice.

Generally, pressure ridges are caused by the deformation of sea ice driven by the wind and ocean currents. Thus, one would expect different behaviour depending on the ice regime - especially if we compare ridges in ice-covered areas such as Arctic, Antarctic and the Baltic sea. Pressure ridges has been detected by different measures: the ridge sails have been detected by airborne altimetric instruments and Digital Mapping System (DMS) (e.g. Duncan et al. (2018); Tan et al. (2012); Williams et al. (2015)), while the keel draft have been detected by underwater echo-sounding instruments (e.g. Tan et al. (2012)). Duncan et al. (2018) estimated pressure ridge sail heights in the Arctic to range in average from 0.99 m to 1.60 m (over FY in Beaufort Sea, March 2013, and Chukchi Sea, March 2015, respectively) and 1.51 m to 2.11 m (over MY in Lincoln Sea, March 2011, and Greenland North Sea, Feb 2012, respectively) by use of DMS visible imagery. Average pressure ridges based on laser altimetry observations for the entire Arctic ranges from 1.14 m to 1.27 m (Rabenstein et al., 2009). Several studies in Antarctica has found average pressure ridge sail heights by use of laser altimetry to range from 0.99 m near the

Table 4.1: Summary of ridge sail height studies from the Arctic, Antarctica and Baltic Sea. Both instrument, area of interest and ridge sails are given. Ridge sails are given by either average or maximum height. Standard deviations are not shown in the table. Values in brackets are lowest and highest 99th percentiles estimated in that study.

Study	Instrument	Area	Ridge sails [m]
Duncan et al. (2018)	Operation Ice Bridge (OIB) and Digital Mapping System (DMS) visible imagery	*Arctic*: Lincoln Sea (MYI) North Greenland Sea (MYI) Beaufort Sea (FYI) Chukchi Sea (FYI)	*Average*: 1.51 2.11 0.99 1.60
Rabenstein et al. (2009)	Helicopter-borne laser altimeter	*Arctic*: near Gakkel Ridge (East) near Fram Strait near Barents Sea near Siberia	*Average*: 1.21 1.27 1.17 1.14
Mei et al. (2019)	Autonomous Underwater Vehicles (AUV) and LIDAR survey (with freeboard and snow)	*Antarctic*: near the Ross Sea	*Maximum*: 1.64 (1.16) to 2.02 (1.53)
Tan et al. (2012)	Helicopter-borne laser altimeter	*Antarctic*: Northwestern Weddell Sea	*Average*: 0.99 to 1.17
Lewis et al. (1993)	Helicopter-borne laser altimeter	*Baltic Sea*: Bay of Bothnia	*Average*: 0.52 to 0.59
Gegiuc et al. (2019)	Helicopter-borne laser altimeter	*Baltic Sea* (Bay of Bothnia): DIR3 (ridged ice) DIR4 (heavily ridged ice)	*Average*: 0.61 0.61

Marginal Ice Zone (MIZ) and the Larsens polynya areas (Tan et al., 2012), to maximum sail height of 2.02 m near the Ross Sea (Mei et al., 2019). For the Baltic sea, the pressure ridges are generally smaller due to the different drift and wind patterns alongside being surrounded by coastlines and the location only allows for FY to form. Various studies shows a general consistency in sail heights comparing heights obtained during winter 1988 with heights from winter 2011 both obtained by laser altimeter measurements (Gegiuc et al., 2018; Lewis et al., 1993). Here the average sail heights ranged from 0.5-0.6 m in 1993 (Lewis et al., 1993) with a 0.40 m cut-off height and were estimated to be 0.61 m in areas of DIR3DIR4 (ridged and heavily ridged ice, respectively) in 2011, where DIR was estimated by SAR image backscatter values (Gegiuc et al., 2018). See a summary of sail height studies in Table 4.1. It is valuable for us to know that ridges tend to range from 0.5-0.6 m in the Baltic (Lewis et al., 1993), when estimating ridging using the photon cloud from ICESat-2.

4.2 Shallow waters in the Baltic and Danish Sounds

To investigate to what extent shallow water bathymetry can be determined from ICESat-2 in the Baltic Sea, we look into shallow waters from several different areas with different water clarity's and conditions: B1 is Kattegat, B2 is the Archipelago Sea, B3 is near Luleå, B4 is near Oulu and B5 is the Sound (see Fig. 4.2). B3 and B4 are both part of the Bothnian Bay and thus, we expect similar water clarity in this sub-basin.

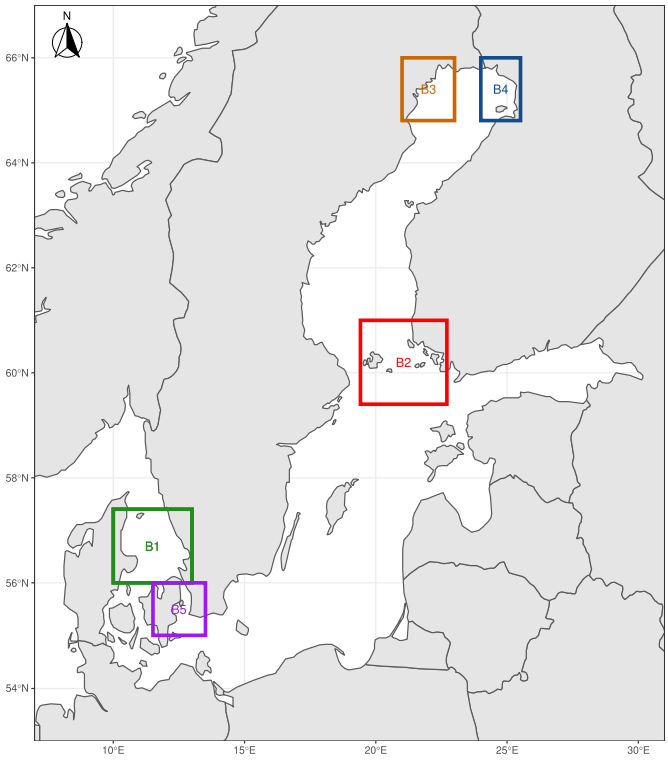

Figure 4.2: Study area for shallow water bathymetry. Boxes defines the different study areas as they have different characteristics: B1 (green) is Kattegat, B2 (red) is the Archipelago Sea, B3 (dark yellow) and B4 (blue) are near the Swedish and Finnish coast in the Bothnian Bay, respectively, and B5 (purple) is the Sound. For the Bothnian Bay (B3 and B4) we will extract photon clouds from both sides, but for the water clarity analysis we will do an overall analysis of the Bothnian Bay due to sparse Secchi depth data coverage.

As has already been mentioned, the shallowest waters are near the Archipelago Sea and the Bothnian Bay for the Baltic Sea, and Kattegat and the Sound for the Danish Waters. To summarise, based on the study of Jakobsson et al. (2019), Kattegat and The Sound have a median depth of 19 m and 12 m, respectively. Åland Sea (which includes the Archipelago Sea in their study) has a median depth of 19 m and Bothnian Bay of 34 m. Water clarity will be further investigated in this dissertation.

4.3 Data description

In this study we utilise five different data set: the geolocated photons from ICESat-2, the Finnish ice charts from FIS, Secchi depths as a proxy for water clarity available from HELCOM, depth profiles available from Baltic Sea Bathymetry Database (BSBD) and SAR images acquired by Sentinel-1 (S-1). These data sets are described in more detail in Sect. 4.3.1-4.3.5.

4.3.1 ICESat-2 data and pre-processing steps

ICESat-2's observatory and ATLAS instrument utilises a photon-counting lidar and ancillary system, which includes star trackers and GPS, to measure the time a photon takes to travel from ATLAS to Earth and back, and to determine the photons geodetic latitude and longitude (NSIDC, 2020a). The travel time of the photon can thereafter be used to estimate the range and from there, the elevation height (see Sect. 3.2). From the measured photons several data products are provided. This dissertation utilises only one of the ICESat-2 data products; The Global Geolocated Photon Data Level-2A (ATL03). You can find brief description of all the primary data products in Appendix A.1.

The Global Geolocated Photon Data product ATL03 is part of the Level-2A data products of ICESat-2. ATL03 are segmented into granules, i.e. files, spanning about 1/14th of an orbit. The boundaries of the granules are given by lines of latitude that define 14 regions, numbered from 01-14 (Fig. 4.3). The Baltic Sea is within region 03 and 05 (ascending and descending track, respectively).

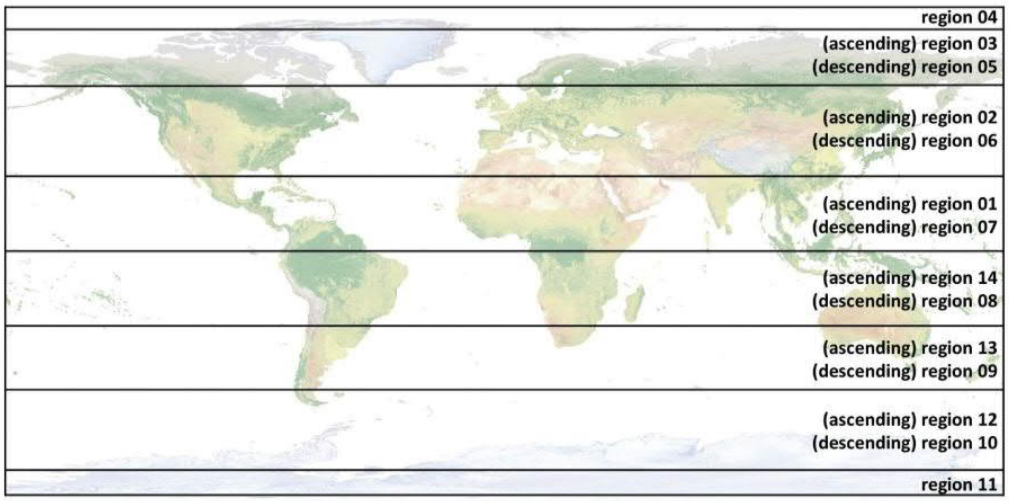

Figure 4.3: ATL03 region/granule boundaries (NSIDC, 2020a)

Simply described, ATL03 provides height, time, latitude and longitude for all photon events that ICESat-2 registers and downlinks. Furthermore, it works as a connection between the lower level data (instrumentation-specific products) and higher level, processed

data (ATL06 and above). ATL03 is the single source to all photon data and ancillary information that is required for this thesis study and for all the higher-level products (NSIDC, 2020a).

Geolocation of photons, surface classification and classification algorithms

The entire process of geolocating the photons is thoroughly described in Neumann et al. (2019b). To generate the ATL03 data product, two components are needed: the pointing vectors of the laser beams and the position of ICESat-2 in orbit. These two components are provided by PPD and POD. Combining the time of flight of the photons, transmit time of the laser pulse, the velocity and position of the spacecraft and the spacecraft attitude it is possible to make the photon geolocation. The time of flight, position and pointing parameters are used to determine the bounce points of the photons by a simple vector calculation, all given in Earth Centred Inertial (ECI) intertial frame. Accounting for precession, nutation, spin and polar motion of Earth allows for a conversion to Earth Centred Fixed (ECF) coordinates. In addition, the bounce point is transformed into International Terrestrial Reference Frame 2014 (ITRF2014) as latitude, longitude and elevation with respect to the reference ellipsoid (WGS84). The refraction correction and tropospheric delay parameters are refined and the photons are re-geolocated. To make the process less computationally expensive, they only geolocate a single photon in every $\sim$20 m along-track, referred to as reference photons. Reference photons are usually chosen between high signal confidence photons if available. If not, either medium or low confidence photons will be used when choosing a reference photons and if no are available, background photons will be used (see definition of signal confidence parameter below). Lastly, corrections for in-orbit instrument variations are applied. All photons are unique in latitude, longitude and height due to the pointing angle of the beams and the topography of the Earth's surface.

The ATL03 product also provides a surface classification mask which separates the Earth into land, ocean, sea ice, land ice and inland water areas. Each of the masked areas overlap the neighbouring area by $\sim$20 km. Several of the areas have more than one classification as the surface types can overlap or not have a unique surface definitions.

The last major step in the geolocation process is to separate signal and background sun photon events. As the telemetered photon events include both types, it is a necessity to be able to discriminate between these and keep all signal photons with as few background photon sun events as possible. The algorithm is based on generating along-track histograms and identifies regions where the photon event rate is significantly higher than the background photon rate. The background photon rate is based on utilising atmospheric histograms (which includes photons reflected off from atmospheric layers, background photons and surface photons). By removing the bins including likely surface photons, it is possible to estimate the background photon rate and use this value as a threshold for what is a likely surface photon event. Depending on the Signal-to-Noise Ratio (SNR), photons are classified as high-confidence (SNR $\geq$ 100), medium-confidence (100 > SNR $\geq$ 40), low-confidence (40 > SNR $\geq$ 3), or likely background (SNR < 3). SNR will be higher for strong beams than weak beams, so the weak beams use the histogram processing of the adjacent strong beam to discriminate between surface and background events. All photons within a given bin are classified as either background sun or signal events.

Pre-processing by signal quality

The classification of photons into confidence levels might aid the analysis if photons not reflected from the surface, e.g. reflections from clouds, are related to a specific class. Here, we investigate the distributions of high confidence quality photons compared to medium and low confidence. If the cloud cover reflections are flagged as medium or low confidence quality photons, it would provide a parameter that allows for most of the erroneous photons to be filtered away. The distribution of low, medium and high confidence photons are shown in Appendix A.3 and the distribution summary (by percentage) of the confidence levels are shown in Tab. 4.2 (for a list of the specific dates in each month, see Appendix A.4).

Table 4.2: Division of the photons divided into high, medium and low confidence levels. The intervals shows the division over all 25 granules acquired during ice season 2018-2019.

Month	High signal confidence [%]	Medium signal confidence [%]	Low signal confidence [%]
January	53.06-99.99	00.01-11.10	00.00-38.40
February	32.02-98.68	01.27-22.93	00.05-45.05
March	01.19-99.99	00.01-08.41	00.00-92.51

There are generally an abundance of high level confidence levels in the data product; from Tab. 4.2 it it shown that all three months includes values with high signal confidence up to $98.68 - 99.9$ %. On average in ice season 2018-2019 the division of the confidence levels were: 84.59 %[1], 4.69 %[2] and 10.71 %[3] for high, medium and low confidence, respectively. It is clear that there are generally fewer medium confidence level photons than low confidence level photons. When comparing the division of confidence level in percentage with the distributions of the photon heights shown in Appendix A.3, it stands out that days with visible cloud cover (cloud reflections) are typically classified as low confidence level photons. Furthermore, most of the photons classified as low confidence also turns out to be reflections from a cloud covers (or to some extent, noise in the surface). In addition, days where the low confidence level is especially high (or even higher than the high confidence level), there seems to be very limited data reflections from a surface or no surface present in the data at all, which could suggest a complete cloud cover (see Appendix A.3 for the photon clouds).

With these observation we propose to use *only* high confidence data, since in most cases there is an abundance of high confidence level data representing the surface. In the cases where the amount of high confidence data is generally lower, it is seen that most of the non-high confidence data is in fact cloud returns (or noise), which is already something we wish to remove from the data. Thus, an additional filtration by using only high confidence level data is applied to the pre-processing part.

Data availability during ice season 2018-2019

First, we investigate the data availability of ICESat-2 during the ice season 2018-2019 (only January to March 2019 since vessel assistance did not begin until end of December, so we assume severity of deformation of the ice cover was not high enough before this).

[1] High confidence averaged: Jan = 89.87 %, Feb = 81.60 % and Mar = 82.34 %

[2] Medium confidence averaged: Jan = 3.11 %, Feb = 8.17 % and Mar = 2.77 %

[3] Low confidence averaged: Jan = 7.02 %, Feb = 10.25 % and Mar = 14.89 %

Table 4.3: ICESat-2 data availability during ice season 2018-2019. Values in parenthesis describes the data files where tracks are covered by clouds.

Month	Available[a]	Overflights[b]	Useless due to clouds[c]	Useful data[d]
January	17	9	0 (7)	9
February	15	9	2 (6)	7
March	18	11	2 (5)	9

[a] Amount of data files available on https://search.earthdata.nasa.gov/search intersecting bounding box 63.10-66.10°N, 20.5-25.5°E.
[b] Amount of ICESat-2 orbits where RGT intersects the Bay of Bothnia basin (chosen by overlaying the .kml-file in Google Earth Pro).
[c] Amount of data files deemed useless due to clouds (determined visually by plotting data from ATl03 data product).
[d] Amount of data files that are available for download, intersects the Bay of Bothnia basin and is not entirely disturbed by clouds.

The data availability depends on the data available for download, RGT (i.e. whether it covers the Bay of Bothnia) and whether the data is disturbed by clouds. In total during the ice season of 2018-2019 (1/1-2019 to 31/3-2019) there were 50 granules available for download on EarthData provided by NASA which intersected the bounding box of 63.10-66.10°N and 20.5-25.5°E (Fig. 4.1). The 50 granules were distributed as: 17 granules in January, 15 granules in February and 18 granules in March. Some days have several tracks intersecting the chosen bounding box, however it might be that the track is not travelling over the sea ice, but merely very close to it causing it to intersect the bounding box. To ensure that the data available within the bounding box also crosses the Bothnian Bay, we visualise the RGT in Google Earth Pro by the .kml-files available at https://icesat-2.gsfc.nasa.gov/science/specs. From the 50 granules available during ice season 2018-2019, there were a total of 29 overflights of the Bothnian Bay almost evenly distributed per month, see Tab. 4.3 column 3.

Furthermore, to ensure that the data is of clear surface returns, we investigate if the photons are affected by cloud cover. We investigate both if the entire track is useless due to full cloud cover and how many of the tracks are partially covered by clouds and needs further filtration. As will be further explained in Sect. 5.1.2, that there is a pre-processing step included when extracting and arranging the data for further processing. This step includes filtration by an absolute height of 1000 m, a confidence quality level denoting if the data is the surface type we expect (sea ice with high confidence) and a bounding box.

When investigating the along-track ICESat-2 orbit data for the presence of cloud cover, it has already been pre-processed. However, it shows that for the ice season 2018-2019 there are few tracks completely covered by clouds, see Tab. 4.3, column 4. However, several of the tracks shows partial disturbance from clouds which has not been filtered out during the pre-processing step. To optimise an automatic ridge-detection algorithm all photons that appears to be reflected from clouds needs to be filtered out. Furthermore, when the photons are referenced to geoid, a threshold of ± 3 m from the geoid is applied which should take care of most of the cloud cover reflections still present in the data. Please note, that the cloud cover seen in the data may also occur as low or medium confidence quality photons and can partly be filtered out by using only high confidence data. For data tracks only partially disturbed by clouds, but which has evident tracks of several kilometres, there are

as follows: 7 in January, 6 in February and 5 in March (see Tab. 4.3). The geolocated photon data products available over the Bothnian Bay for the ice season 2018-2019 is shown in Appendix A.2. It is also these plots that the visual inspection of cloud cover is based on. In summary, for the ice season 2018-2019 there are in total 25 granules (data files) available partitioned as: 9 in January, 7 in February and 9 in March. Most of the filtering of data happens in the pre-processing phase, before extracting the final data set for processing, thus no exact statistics on how much data was filtered away is presented. Appendix A.3 shows the distribution of high, medium and low signal confidence which can provide the reader an idea on how much was removed by this step in the pre-processing phase. Out of the 25 granules with available surface reflections from sea ice, at least 18 must be processed further to exclude cloud returns. The 18 granules in need of further processing are partitioned as: 7 in January, 6 in February and 5 in March. A summary of the data availability is shown in Tab. 4.3. We also investigated the data availability during April and May (until 14th of May where the ice season ended). 12 granules with overflights over the Bothnian Bay were extracted, but all 12 granules were completely disturbed by cloud-cover and deemed useless in this study.

Data availability for shallow water bathymetry

For shallow water bathymetry, we choose not to look into the coastal/shallow water areas of the entire Baltic, but instead work on a proof-of-concept from known shallow-water areas. This includes looking into different areas (four areas) from different areas in the Baltic (and the Danish Sounds) with different characteristics (see Fig. 4.2). We will extract one or two ICESat-2 tracks from each area for analysis to show the potential for shallow water bathymetry in these areas.

4.3.2 Daily ice charts from the Finnish Ice Service (FIS)

Ice charts divide the ice cover into regions which represents ice fields with different characteristics and age. Furthermore, the thickness values seek to represent the typical thickness of level ice in each region. Ice charts of the Baltic are published daily by the ice service of FMI during the ice season (Fig. 4.4). There is two primary types of ice charts: basic graphic charts and gridded versions with different resolutions. The gridded charts compose information on e.g. ice concentration, average thickness, maximum thickness, minimum thickness, deformation (DIR) and sea surface temperature. The intervals of DIR on ice charts ranges from 0 to 5 and denotes: level ice, rafted ice, slightly ridged ice, ridged ice, heavily ridged ice, and brash barrier. The graphical charts represents these types with qualitative symbols only. Primary information sources for the ice charts include satellite images to estimate ice existence and concentration and in situ measurements and visual observations for ice thickness. Thickness values are based on observations made by crew members on ice breakers and, for nearshore fast ice, at fixed stations. Deformation numerals and ridging are based mostly on visual icebreaker observations and can be used as a regionally descriptive of the conditions from the point of view of navigational difficulty (Ronkainen et al., 2018).

4.3.3 Secchi depth measurements from ICES HELCOM

To investigate the bathymetric capabilities as a function of water clarity, we look into Secchi depths and use these as a proxy for water clarity. As part of the Baltic Marine Environment Protection Commission, the Helsinki Commission (HELCOM) has several stations with observations of Secchi depth (part of International Council for the Exploration of the Sea (ICES) stations) with measurements acquired from 1975-2018 (some

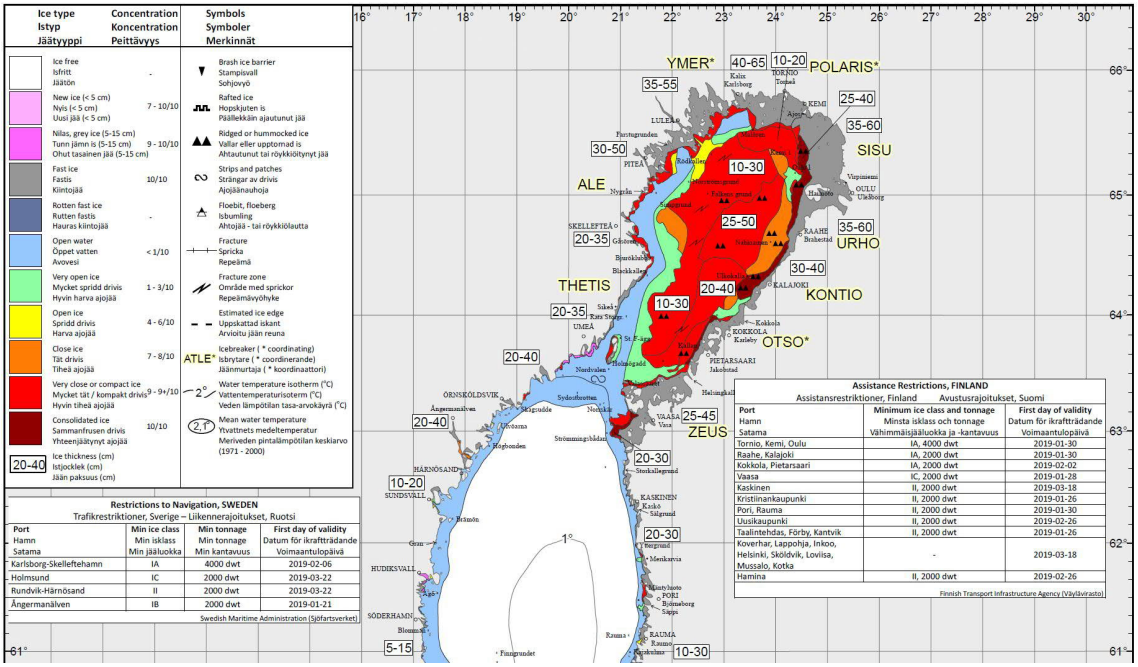

Figure 4.4: Graphical ice chart from 23 March 2019 cropped to the Bothnian Bay, generated and provided by the Finnish Ice Service (FIS).

measurements are even acquired earlier than 1975, but from the ones used in this study, the earliest is from 1975). We have extracted measurements (around 5 stations pr area) from different places in the Baltic (Archipelago Sea and Bothnian Bay) and the Danish Sounds (Kattegat and The Sound). We would like to emphasise that we have converted some of the Secchi depth measurements from centimetres to meters to ensure consistency and to be able to compare the different areas. This is even though the data set is said to have units of meters, but with measured Secchi depths above the value of 80 cm making us question this. Especially since most of the ships in the Finnish waters does not have a Secchi disk with a rod longer than 20 m (Fleming-Lehtinen, 2016; Rinne, 2020c). The centimetre measurements are predominantly in the Finnish Waters and changed to centimetre. This means that for the Finnish waters, we may be underestimating the Secchi depths. The ICES data set is available at: https://takaovi.fmi.fi/Helcom/,DanaInfo=ocean.ices.dk,SSL+Helcom.aspx?Mode=1.

4.3.4 Depth profiles from Baltic Sea Bathymetry Database (BSBD)

To compare bathymetric measurements from ICESat-2 with depth profiles from the BSBD, supplied by Baltic Sea Hydrographic Commission (BSHC). The depth profiles are drawn manually by the user and can include differences in latitude and longitude from the actual ICESat-2 track as it is manually and visually chosen by the user. Nonetheless, it is still a valuable comparison, as it provides the opportunity to investigate whether some specific bathymetric features can be seen in ICESat-2 measurements.

BSBD is created to gather bathymetry data for all of the Baltic Sea countries in one place. It is important to emphasise that this data set is different from official nautical paper charts as it is basically a digital terrain model using smoothing and interpolation algorithms, thus this specific data set is not suitable for navigating purposes. However, BSBD states that

it is useful for e.g. climate modelling and geological research (BSHC, 2020a) .

As explained by BSHC (2020b), the data used to produce the bathymetric database is based on national data products and thus, they vary with respect to data sources, quality and resolution. For Denmark, they extract gridded Triangular Irregular Networks (TIN) which is based on a combination of modern measurements and digitised nautical charts with interpolation applied. This data set has a spatial resolution of 50 m expect in the North Sea, where the resolution is 100 m. Sweden utilise data from the national depth database with a 100 m x 100 m grid unless it is the territorial waters, where they utilise a 500 m x 500 m grid due to legal restrictions. For each cell with data it is the average value that has been extracted. Data from Finland have depths combined from official nautical charts (in the territorial waters) and recent high-resolution surveys. In most of their data a 200 m x 200 m grid with average depths extracted from each cell has been used. Where 200 m is not available, depth figures from the nautical charts have been used instead. This goes as well for the territorial waters.

4.3.5 Sentinel-1 Synthetic Aperture Radar (SAR) images

The Synthetic Aperture Radar (SAR) imagery used in this thesis for comparison and evaluation of ICESat-2 photons (ATL03) is from Sentinel-1A/B (S-1A/B) platforms. The S-1 system is based on a two-satellite constellation of C-band SAR imagery (Kwok et al., 2019b). This thesis utilises one C-band frame, the Groun-Range Detected (GRD) product, acquired by S-1B on 28 March 2019 at 04:56:10 in Extra-Wide (EW) swath mode, which is a mode primarily applied to sea ice monitoring (Huang et al., 2017). The EW product has at high spatial resolution of 50 x 50 m or medium resolution of 93 x 93 m and a swath width of 420 km (Stasolla and Neyt, 2018). The SAR imagery used here were processed by ESA and archived at the Alaska Satellite Facility.

5 Methods

The method used to estimate DIR and shallow water bathymetry is presented in this section and a short overview of previous work from ICESat-2 related DIR and shallow water bathymetry is provided.

5.1 Determination of Degree of Ridging (DIR)

Determination of DIR is just one of the ridging parameters that would be interesting to investigate, however it is one of the most important parameters in ship navigation. Thus, it is the one parameter we have chosen to investigate using the ICESat-2 photon measurements.

5.1.1 Previous work

Studies on how to use ICESat-2 measurements to determine several interesting aspects of the Earth e.g. sea ice thickness (Kwok et al., 2020, 2019b; Petty et al., 2020), ocean and wave modelling (Klotz et al., 2019) or nearshore bathymetry (Armon et al., 2020; Parrish et al., 2019) has been published during 2019 and 2020, but no studies on sea ice pressure ridges from ICESat-2 have been published so far. The closest we have gotten to studies on pressure ridges from ICESat-2 is a published abstract from 2019 CISESS Science Meeting on Analysis of Arctic Sea Ice Pressure Ridges from ICESat-2 by Duncan and Farrell (2019). Here, they already state that higher level data products such as ATL07 are not suitable for retrieving ridge sail heights after validating with Airborne Topographic Mapper (ATM) laser altimeter data. It may be caused by the small-scale surface roughness structures being lost after the processing to ATL07 (Duncan and Farrell, 2019). However, they propose a first look at a new algorithm to find ridges from the geolocated photons of ATL03 and use the algorithm to calculate ridge sail height and ridge frequency distributions. This suggests, that ATL03 keeps the ridging information and can prove suitable to estimate pressure ridges.

We would like to highlight, that this abstract was not found by the authors until after most of the processing and analysis had been done. We have contacted the authors of Duncan and Farrell (2019) for a greater insight into their work, but has yet to get a respond on this. Due to issues with estimating parameters needed for locating pressure ridges (e.g. estimating a proper Local Sea Surface (LSS)), we were not able to successfully produce an algorithm to detect individual ridges using conventional methods used by former studies on pressure ridges (e.g. Farrell et al., 2015; Ronkainen et al., 2018; Tan et al., 2012). On the contrary, we will instead introduce a method for investigating DIR, a ridging parameter especially useful for ice navigation. We will in our discussion of the results and proposal of future considerations and work explain the issues we encountered when trying to determine individual ridges and propose an initial approach to estimate the ridges assuming several of the problems we encountered have been solved.

5.1.2 Processing scheme

The processing scheme for estimating DIR in the Bothnian Bay is shown in Fig. 5.1. This includes the entire process from retrieving the useful parameters from the raw ICESat-2 data to evaluating the photon distributions and estimating the DIR.

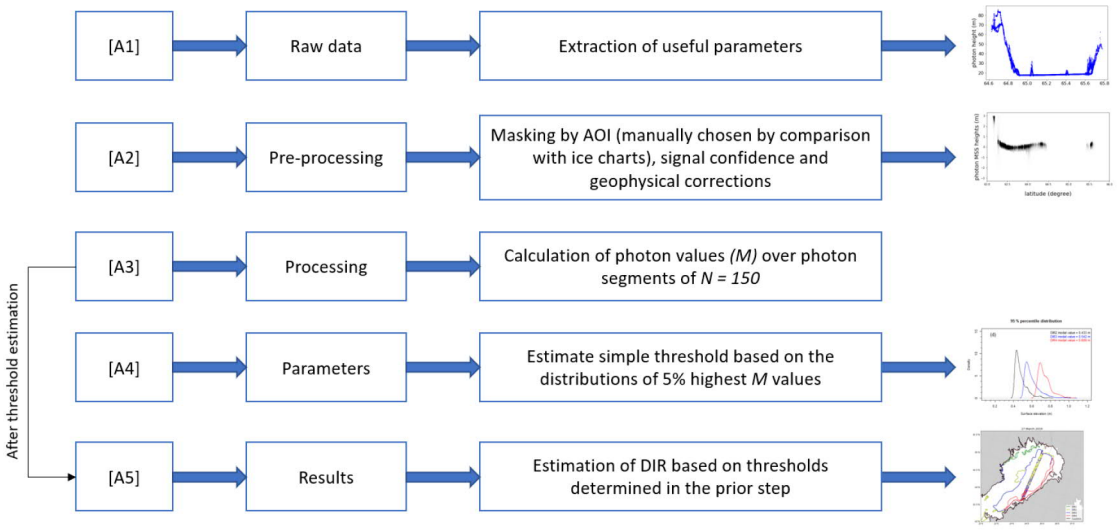

Figure 5.1: Processing scheme for estimating DIR in the Bay of Bothnia.

[A1] is the initial processing of the data. Here, we extract beam-specific parameters from the ATL03 data set, more specific: latitude (*lat_ph*), longitude (*lon_ph*), photon ellipsoidal heights (*h_ph*), signal confidence (*sign_conf_ph*), geoid correction (*geoid*), dynamic atmospheric correction/inverted barometer (*dac*) and ocean tide correction (*tide_ocean*). A few filtration steps are applied during the extraction phase, which includes an initial threshold of 1000 m and a bounding box selected by the user. If the user sets the bounding box as `None`, the entire granule track will be used.

[A2] includes the required pre-processing steps for the ATL03 photon product to extract photons from the surface of sea ice covered regions. The masking process simply mask out photons not of *signal_conf_ph* = *high* (based on the analysis in Sect. 4.3.1 which concludes, that only high signal confidence photons should be used). Further filtration removes photons not within a given bounding box (Area of Interest (AOI)) defined by the user. Here the bounding box is the Bothnian Bay and based on input from ice charts. The geophysical corrections (*geoid*, *dac* and *ocean tide*) have been removed by fitting a third degree polynomial to the data, since the corrections are only provided for every $\sim$20 m. We do not expect too large deviations caused be applying this trend, as the corrections have larger variations than 20 m (see Sect. 3.5). After applying the geophysical corrections we apply an additional filtering step, where we remove all values that are not within the range of $\pm$3 m from the geoid.

An example of the geophysical corrections, masking and filtration is shown in Fig. 5.2. Especially Fig. 5.2a shows the need for filtration as the selection of photons classified as high signal confidence does not necessarily ensure all clouds to be removed. The surface ($\sim$18 m ellipsoidal height) reflections are marked by a red box. Fig. 5.2b shows the photons after applying the geophysical corrections and removing photon heights outside the range of $\pm$3 m from the geoid. Here, the cloud returns of the upper-laying cloud cover (64.5-66°N) as seen in Fig. 5.2a (blue box) is no longer present. Returns from near the coast (around 63.0° N) remains. We did not make use of the surface classification mask, since it includes land surfaces also flagged as ocean within 20 km from the coast, as described in Sect. 4.3.1. Since we instead manually extract tracks by comparison with

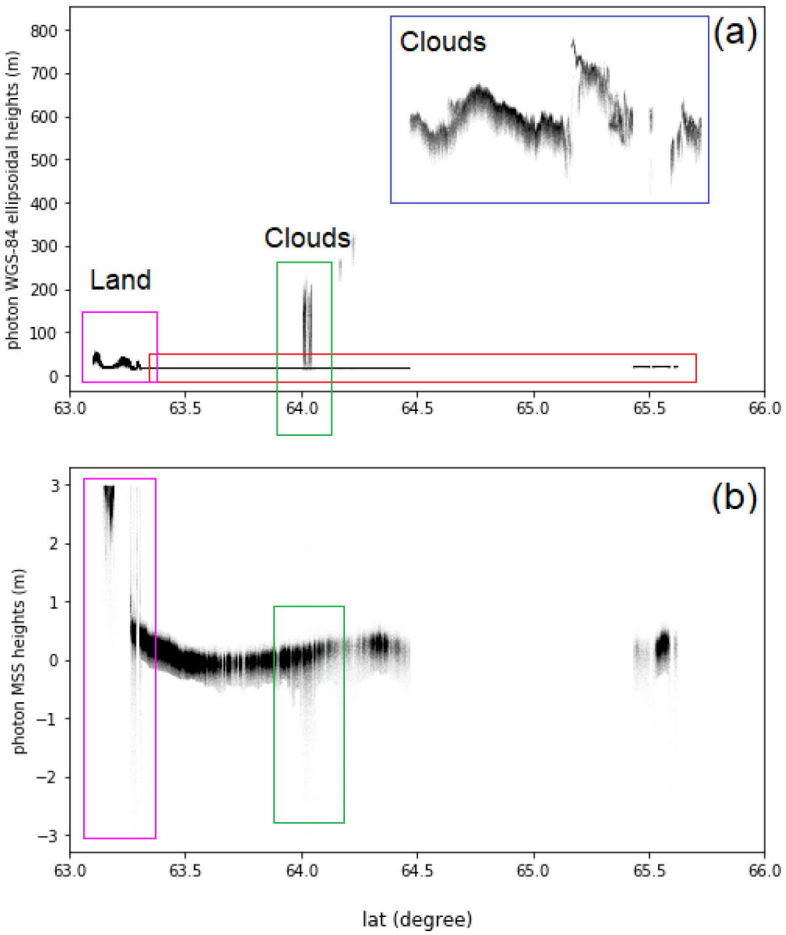

Figure 5.2: Photon elevations with high signal confidence from 1 February 2019. (a) WGS84 ellipsoidal photon heights from 63.0° N to 66.0° N. (b) photon heights after geophysical corrections (referenced to the geoid). The geophysical corrections are only applied over ocean, thus the fit will cause the photons near land areas to have a small bias (see e.g. 63.0-63.5° N). Read square defines the sea ice surface/sea surface reflections. Blue box defines the upper-laying cloud cover. Green square highlights affect by lower-laying clouds. Magenta box highlights the land cover.

ice charts, this is not seen as a potential cause for bias or error in the data. Photons that may also have been affected by lower-laying clouds (around 64° N) also remains. This has not been filtrated further in this study, but future work be included to ensure that the erroneous photons are to be removed.

[A3] is a basic processing step that calculates the photon values (M) by:

$$M = \max(h_{ph}(N)) - \text{mean}(h_{ph}(N)), \tag{5.1}$$

where h_{ph} is the photon elevations and $N = 150$ describes a segment of N photon elevations. It is a rather simple calculation that extracts a segment of 150 photons, calculates the maximum value and the mean value of the segment to calculate the M value. It is important to remember here, that the segment used are based on the number of photons which are dependent on the reflectance of the surface, cloud cover and energy of the laser pulse. Weak beams generally have fewer photons and thus, longer distances between each segment value. Furthermore, if there are areas with cloud disturbing photons or background photons that does not coincide with the surface photons, these will affect the segment value

and introduce a bias. In this step we estimate the latitude and longitude for the segment value as the mean value of the latitudes and longitudes within the segment.

[A4] is the estimation of intervals for different DIR regions based on simple thresholds. The thresholds will be based on the distribution of the 5 % highest of the M values (see Sect. 6.1.1 for analysis of the distributions and the actual estimated thresholds). Once the thresholds are determined, this step becomes superfluous as intervals based on thresholds have been set and can be used for future analysis. Nonetheless, it is an important step, as it shows whether or not different DIR zones can be distinguished from each other.

[A5] is the calculation of DIR values based on the thresholds determined in *[A4]*. These values can then also be showed over a map of longitude and latitude to show the distribution of the estimated DIR values. As a summary, the main steps we take to estimate DIR from ICESat-2 is shown in Algorithm 1.

Algorithm 1 DIR estimation from ICESat-2's geolocated photons (ATL03) in the Baltic Sea.

Require: Extract *lat_ph*, *lon_ph* and *h_ph* from the ATL03 granules. Pre-process the data with a mask of using only high signal confidence photons by parameter *signal_conf_ph* and a mask of ± 3 m from the geoid.
  for every segment of $N = 150$ **do**
    Calculate the value to categorise by, which is given as the mean value of the N photon segment subtracted from the maximum value of the N photon segment (M value). Calculate latitude and longitude of the segment as the mean value of the latitudes and longitudes within the segment of N photon elevations.
    if value is within a category of DIR **then**
      Apply the category of DIR to that value. Since there are currently only categories for DIR2-DIR4 (from slightly ridged ice to heavily ridged ice), we will have no way of saying if the values are within zones of level or rafted ice (DIR0 or DIR1) or brash barriers (DIR5).
    else
      Disregard the value. This results in a data set that only includes DIR2 to DIR4 values. It should be expected that e.g. DIR2 and DIR3 values will appear in DIR4 zones as well when there is almost no or little ridging occurring over an area.
    end if
  end for

5.2 Shallow water bathymetry

Especially shallow water (also usually referred to as near-shore or coastal) bathymetry is important, as it can provide information useful for coastal science, safe navigation and climate monitoring, but the measurements are sparse. Measurements in the shallowest of waters have been acquired by standing rods. Boat-based acoustic hydrographic surveying technologies such as Multi-Beam Echo-Sounders (MBES) allows bathymetric measurements in deeper waters (larger than four meters) (Parrish et al., 2019). Furthermore, airborne LIDAR are used in shallow water bathymetry (e.g. Quadros et al., 2008), but global measurements from satellites would be preferable since it provides measurements over greater extent than airborne or boat-based surveys.

Satellite remote sensing methods for acquiring bathymetric measurements are based primarily on passive, multi-spectral imagery and satellite altimetry. The advantage of multispectral imagery is the large spatial extent compared to track measurements acquired from LIDAR measurements (e.g. ICESat/ICESat-2). However, false readings caused by change in substrate types or other variables introduced by the environment or the need for a reference depth in multi-spectral imagery prove as disadvantages (Parrish et al., 2019). Bathymetry from satellite altimetry is based on inverting the SSH measurements as they provide information on gravity and the distribution of mass on Earth. From this, bathymetry can be predicted (Fan et al., 2019).

Depth mapping performance for bathymetric LIDAR measurements are based on water clarity and thus, the performance of ICESat-2 changes temporally. Nonetheless, the direct bathymetric mappings from ICESat-2 at a high spatial resolution can be useful to prevent shallow-water data gaps with less false reading as the measurements are directly reflected from the seafloor. Furthermore, in fusion with multispectral imagery, it can provide an optimal solution for shallow water bathymetry from remote sensing observatories (Parrish et al., 2019).

5.2.1 Previous work

Quadros et al. (2008) presented the first results of using photon measurements (green laser, 532 nm) to estimate bathymetry by MABEL measurements. MABEL proved able to detect seafloor returns up to 8 meters depth in the waters of Keweenaw Bay, Lake Superior. The depth capacity was corrected for refraction and water-level in the MABEL photons. With Keweenaw Bay being generally optically complex and having oligotrophic, relatively low production due to low nutrient content waters, it was of great interest as it showcased the capabilities of ICESat-2 in estimating bathymetry. No water clarity data was available to make a direct comparison or analysis of how well the photons detected versus water clarity. Nonetheless, was this the first major indicator that ATLAS could be used in an innovative way, beyond the scope of the objectives, to estimate shallow water bathymetry with high spatial resolution.

Parrish et al. (2019) were the first to investigate ATLAS photons with the objective of determining how well it could be used to measure bathymetry in shallow waters. Their primary research questions included assessing whether ATLAS could reliably measure bathymetry, how accurate it could measure it if possible and to what extent the the maximum depth mapping capability was as a function of water clarity, using Secchi depths as a proxy for water clarity. They showed that over the Virgin Islands (St. Thomas) it was possible to extract clear seafloor returns down to 38 m depth. Furthermore, they investigated three other areas: (1) Turks and Caicos; (2) North West Australia; and (3) Great Bahama Bank. For (1) they were able to extract seafloor returns down to 24 m, for (2) 19 m and (3) 13 m. This is with refraction corrections applied (otherwise, the maximum depth was (1) $\sim$32 m, (2) 25 m and (3) $>$15 m. They propose the method of properly extracting the bathymetric measurements by applying refraction corrections to the identified seafloor measurements. This includes manually extracting the seafloor measurements as bathymetric measurements before correction and water surface measurements for a surface reference, and applying geometric corrections to take into account the refraction caused by the air-water surface and the change in speed that the signal experiences. They state how the *z-error* (depth error) increases with increasing depth when the refraction correction is omitted as is expected. From their plots it seems that when the depth is between

0-10 m, the *z-error* is usually around 0-2 m. When applying the refraction correction the mean absolute error (for St. Thomas area) ranged from 0.30-0.44 m depending on which beam was used. In summary, it is possible in these waters to estimate bathymetric measurements with high accuracy provided the refraction corrections are applied. To investigate the depth mapping capability as a function of water clarity, they use Secchi depths (a conversion from diffuse attenuation coefficient $K_d(490)$, a measure of water's turbidity (Alikas and Kratzer, 2017), obtained from Visible Infrared Imaging Radiometer Suite (VIIRS) data, to Secchi depths using three empirical relationships between K_d and Secchi depths, see more in Parrish et al. (2019)). Here they find the average of maximum penetration to be 0.96 of the Secchi depth over the four areas, with a standard deviation of 0.10 m. This concludes their study by showing that as a function of water clarity, it is possible to estimate bathymetry measurements up to almost the total extent of the measured Secchi depths.

We investigate the use of ICESat-2 to determine bathymetry in the Baltic, a sea highly affected by eutrophication. The goal is to find shallow water bathymetry measurements from ICESat-2 in the Baltic (and Danish Sounds) and compare these with depth profiles of same area. We will not use the refraction corrections from Parrish et al. (2019) in this paper, however we would like to emphasise that future studies and work should apply these refraction corrections for obtaining the actual depths. We assume the corrections needed are fairly small, as the Secchi depths are significantly smaller in the Baltic and Danish Sounds compared to depths used in Parrish et al. (2019), thus is not as affected as e.g. in St. Thomas with depths of up to 38 m.

5.2.2 Processing scheme

Processing scheme for assessing bathymetric capabilities of ICESat-2 in the Baltic is shown in Fig. 5.3.

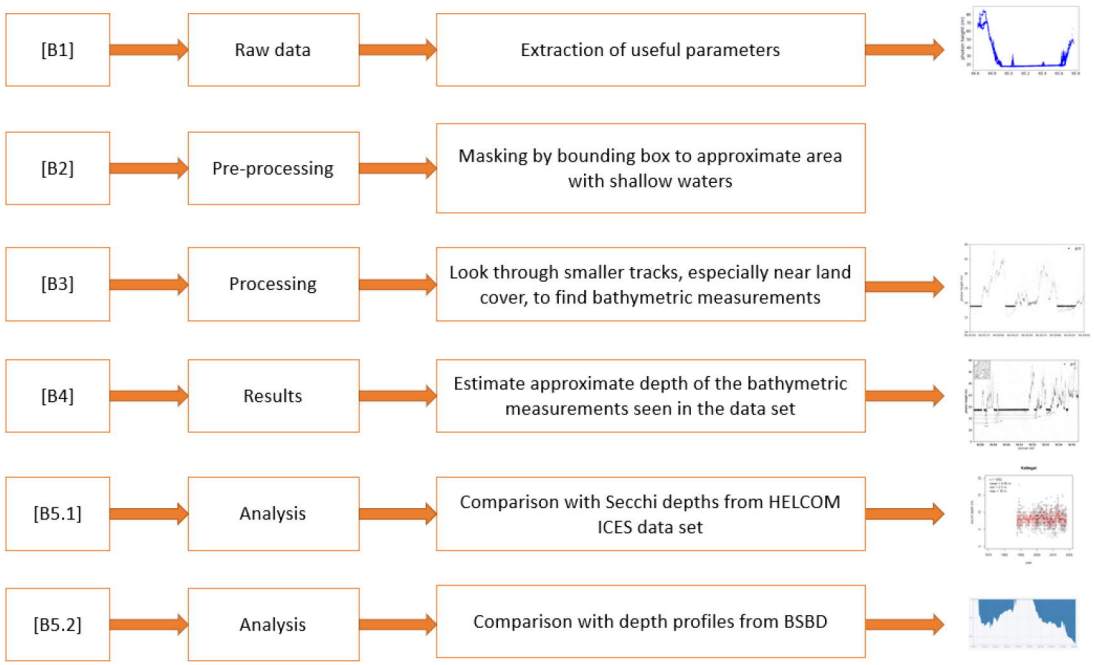

Figure 5.3: Processing scheme for shallow water bathymetry.

[B1] is the extraction of useful parameters from the raw ICESat-2 data granules. Here we extract latitude (*lat_ph*), longitude (*lon_ph*) and ellipsoidal heights (*h_ph*). We do not extract any geophysical corrections nor the signal confidence parameter. A few filtration steps are applied during the extraction of useful parameters including a height threshold of 1000 m and a bounding box defining the area of interest to be applied by the user. If the bounding box is `None`, the entire track will be returned.

[B2] is a simple pre-processing step that masks some of the data by a user given bounding box. This is to exclude most of the tracks, especially if the user has not already made use of the filtration in step *[B1]*. If one identifies some bathymetric measurements, go to step *[B3]*. If there are no photons or a lot of returns are disturbed by clouds, the data is unusable.

[B3] is the main processing step. This includes manual inspection of the ellipsoidal photons to determine if they represent bathymetric measurements. This can be a tedious process, since the bathymetric measurements can be very few and sparsely distributed compared with measurements from the water surface, so it is necessary to look closely into tracks segments of a few kilometres at a time. Compared to the studies of Parrish et al. (2019) that had over 300 km of dense and clear surface measurements, we do not expect this in the Baltic Sea mainly due to the murkier waters.

[B4] includes estimation of the approximate depth of bathymetric measurements. This manual procedure basically includes estimating the depths from the bottom of the surface returns and to the different identified bathymetric features. It should be mentioned that this depth is not necessarily the actual depth since refraction corrections has not been applied.

The analysis of the bathymetric measurements can be divided into two parts. *[B5.1]* includes comparison of the bathymetric measurements with Secchi depths extracted from HELCOM ICES data set (Sect. 4.3.3) to investigate how well the bathymetry capability is as a function of water clarity. *[B5.2]* is a comparison with depth profiles from BSBD (Sect. 4.3.4). We will primarily use the depth profiles to identify clear bathymetric features.

6 Results

The results for estimating DIR in the Bay of Bothnia by ICESat-2 photons are presented. In addition, the detection of seafloor by ICESat-2 observations in the Baltic and Danish Sounds are presented along-side a comparison with Secchi depths to evaluate the depth mapping performance as a function of water quality.

6.1 Estimation of ice ridging in the Bothnian Bay

Initially the idea was to investigate the ridge sails and ridge density based on identified pressure ridges in the ICESat-2 photons. When investigating the photons it was clear, that there were several photons in what seemed to be within a ridge and not just at the surface likely caused by subsurface scattering (Kwok et al., 2019a) which complicates the conventional approach. Instead, we look into segments of photons and use of a similar approach as the higher-level ICESat-2 data product Surface Height product (ATL07) do when determining surface heights, where we aggregate a segment of $N = 150$ photons (see Sect. 5.1.2, it represents approximately 17 m based on strong beam (GT3L) data from 17 February 2019). The value represented over the segment provides an idea of the sensed surface of that segment by taking into account several photons. In this study we look into

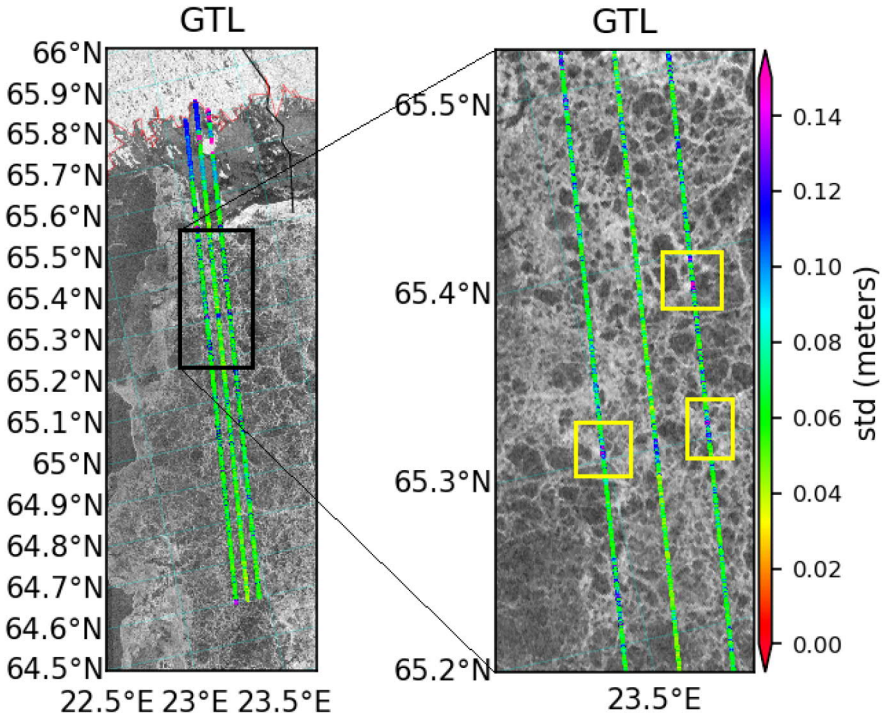

Figure 6.1: Surface roughness (by standard deviation (SD)) of $N = 150$ photons segments over the Bothnian Bay acquired the 27 March 2019. As background is a Sentinel-1 (S-1) C-band Extra-Wide (EW) swath mode Synthetic Aperture Radar (SAR) image acquired on 28 March 2019 at 04:56:10 (around ∼0.45 day after). White areas in SAR imaging is equivalent with increased backscatter related to rougher areas (compared with e.g. calm oceans shown as blacker areas). Yellow boxes denotes areas referred to in the text.

Standard Deviation (SD) as a proxy for surface roughness. The surface roughness given by SD of each segment of photon values are visually compared to S-1 images (Fig. 6.1). S-1, SAR images acquired at C-band in EW swath mode, shows the backscattering of the surface. Large backscatter pixels (white areas) are usually equivalent with rough surfaces, i.e. ridging and deformed ice. Thus, values with high SD values will be expected over ridged ice represented in the SAR image as areas with large backscatter, i.e. white areas. This is also clear from Fig. 6.1, where directly over rougher areas identified in the SAR image, we find larger values of SD of about 0.10-0.12 m and few values above 0.14 m (Fig. 6.1, yellow boxes). It is however also clear, that there is an abundance of smaller SD values about 0.06 m. This can be an indication of $N = 150$ being a too small segment, so the photons are all within the same range, or that there generally is a lot more level ice than ridged ice, where level ice is indicated by surface roughness measurements of 0.06 m. This last statement is follows the assumption that on average in the Baltic sea, we will experience 95-97 % level ice and little ridges or rubble fields (private communication, Rinne, 2020a). It can be difficult to read from Fig. 6.1 whether the photon observations are too close making them overlap causing some information to be lost. This example demonstrated that there is indeed valuable ridging information available in the ATL03 data product from ICESat-2. We are especially interested in looking into the higher values of SD describing the ridge, as this will give an idea of how high the ridge is. Surface roughness given by the SD is affected by outliers and includes more information on the majority of the measurements than on the outliers. Additional ridge information could be

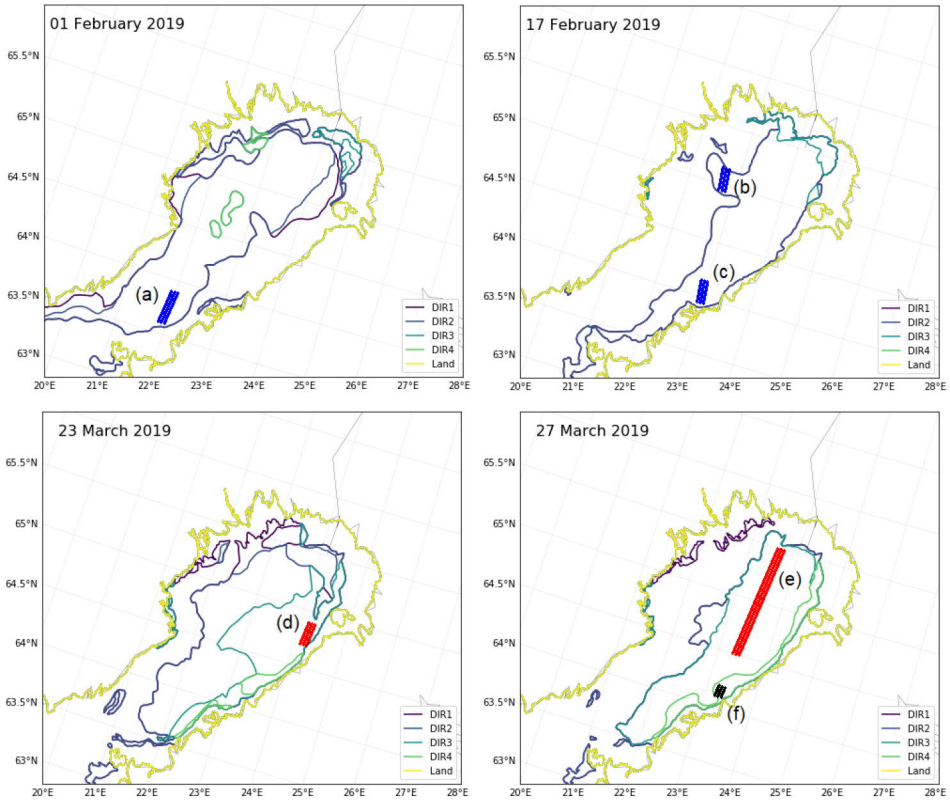

Figure 6.2: Tracks used for different DIR zones from ICESat-2. The colours represents the DIR; blue, red and black is DIR2, DIR3 and DIR4, respectively. Contours of DIR zones from ice charts are shown. Letters represents which DIR area we are referring to: DIR2a-c, DIR3d-e and DIR4f.

held in some of the highest, but fewer, values. Thus, a different measurement than SD is necessary.

To have another measure of ridging, we look into how to separate ridging from the level ice occurring throughout the same track. One measure of this is e.g. by taking the highest value within a segment of photons and from this value, subtract a measure of the level ice, e.g. by taking the average value (*mean*) or the *median*. This approach of substracting the mean as a measure of level ice is used in Sect. 6.1.1-6.1.2. One could also look into, not only, the highest value, but e.g. the 95 % percentile value of a segment (or 99 %) as this will remove the uncertainty of using an outlier as the highest value, since we are currently assuming the highest value to be the top of the ridge. We will comment on both approaches (subtracting *mean* or *median*) along-side the weaknesses of using the highest value (*max*) in comparison with e.g. a percentile value. This is presented in Sect. 6.1.3.

To investigate pressure ridges and DIR, we extract relevant ICESat-2 photons using the FIS ice charts as reference data set. In particular we extract DIR from areas manually chosen by visually comparing tracks from ICESat-2 with the ice chart polygons of the different DIR zones (Fig. 6.2). For DIR2, three areas have been chosen partitioned as one area from 1 February 2019 (DIR2a) and two areas from 17 February 2019 (DIR2b and DIR2c). DIR3 are extracted from two areas from two different days: DIR3d from 23 March 2019 and DIR3e from 27 March 2019. DIR4 are extracted from 27 March 2019. We look into the distributions of the photons from the different DIR areas and utilise intervals based on simple thresholds to classify the photons into different DIR zones.

6.1.1 Comparison between photon distributions in different DIR zones

As already mentioned, our hypothesis is that areas of heavier ridging, i.e. DIR zones of higher value, should be distinguishable from the photon product since with heavier ridging and deformation comes higher ridge sails. Thus, a larger amount of the measured elevations will be higher than the measured elevation of level ice when comparing with areas of less ridging. We want to emphasise, that this hypothesis is only based on *amplitude* and not *spatial* parameters. Spatial parameters are also relevant in determining DIR, as more deformation (thus, more ridges over a smaller area) can lead to a higher DIR zone.

To evaluate if this hypothesis is true, we investigate the distributions of photon elevations (mean elevation subtracted from the highest elevation) within a segment of $N = 150$ photons. $N = 150$ is a quite short segment if there are lots of photon returns, but were chosen as this is the same amount of photons used in the higher-level products to estimate surface heights with centimetres accuracy (Kwok et al., 2019b). Hence, we assumed this to be a reasonable amount of photons. The segment length of 150 photons were $\sim$17 m (based on measurements from strong beam GT3L acquired on 17 February 2019). We would like to emphasise, that while this segment is rather short, it varies with the amount of photon returns and can be longer in case of spatially sparse distributed photon returns. Generally, segment lengths are longer over darker areas, as there are fewer returns (Kwok et al., 2019a). The photons have, as already mentioned, been filtered by selecting only *high signal confidence* photons and applying the geophysical corrections, and the threshold of $\pm$3 m from the geoid. The distributions of the photon relative elevations (highest elevation with mean elevation subtracted of $N = 150$ photons in each segment) show different distributions for different DIR zones (Fig. 6.3a), but with a significant overlap. The error

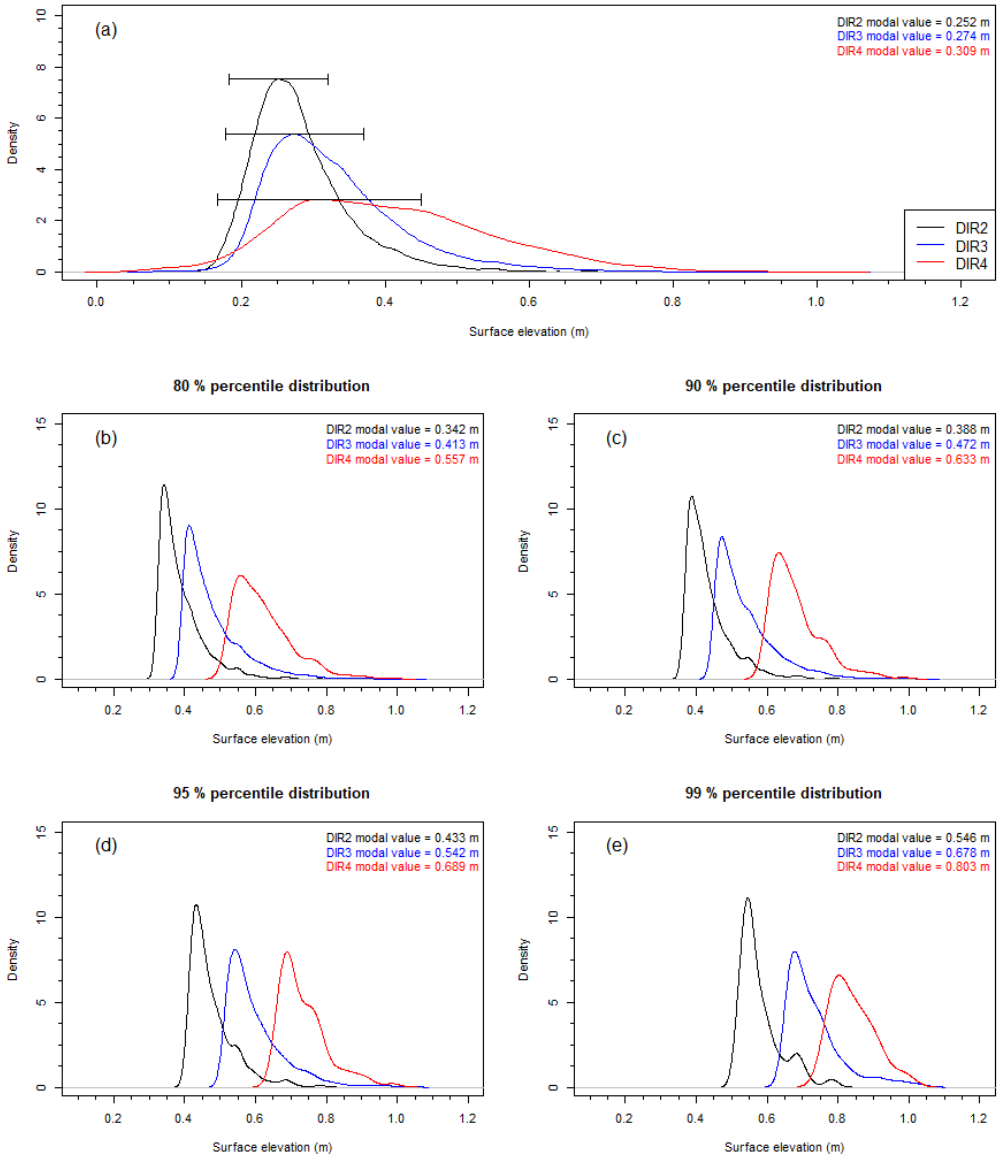

Figure 6.3: Distributions of mean elevation subtracted from the highest elevation in a segment of $N = 150$ photon elevations to estimate different degree of ice ridging (DIR) zones. DIR2, DIR3 and DIR4 are shown in black, blue and red, respectively. (a) distributions of all $N = 150$ segments from the different DIR zones with the variation shown as error bars (given by standard deviation), (b) distributions of 80 % percentile values of $N = 150$ photon segments (the 20 % highest values), (c) the 90 % percentile values (10 % highest values), (d) 95 % percentile values (5 % highest values), and (e) 99 % percentile values (1 % highest values). Modal value of each distribution is provided in the graphs.

bars used for visualising the variation of the distributions (by standard deviations) shows that it is not possible to estimate simple thresholds on the distribution of all the values by e.g. SD, as these will overlap completely.

When investigating only the highest values (observations above specific percentiles) of a segment, assuming that heavier ridging again has higher values, there is a significantly larger difference between DIR2-DIR4 classes. This is evident already from the 20 % highest relative elevations (Fig. 6.3b), but the overlap is still too large here to estimate intervals

Table 6.1: MAD values and intervals (thresholds) estimated from 95 % percentile (5 % highest values) of highest elevation - mean elevation over $N = 150$ segments of photons. The thresholds are given by the modal value $\pm$ the mean absolute deviation (MAD). Adjusted intervals are simply to exclude the gap between DIR3 and DIR4.

Ridging zone	Modal [m]	MAD [m]	Intervals (modal $\pm$ MAD) [m]	Adjusted intervals [m]
DIR2	0.433	0.045	0.389-0.478	0.38-0.48
DIR3	0.542	0.060	0.482-0.602	0.48-0.60
DIR4	0.689	0.057	0.632-0.746	0.60-0.75

that does not overlap. The same yields for the 10 % highest of the relative elevations (Fig. 6.3c). For the 5 % highest (Fig. 6.3d) and 1 % highest (Fig. 6.3e) there is still an overlap, but it is small enough to produce reasonable intervals based on simple thresholds.

In the further studies we apply the simple threshold-based classification to extract DIR values from ICESat-2 based on the 5 % highest relative elevations. As the distributions are right skewed, we use the Mean Absolute Deviation (MAD) to estimate the thresholds instead of the classic SD (Leys et al., 2013). MAD is the median of the absolute deviations from the median, and is usually more robust in the presence of outliers compared to SD. The intervals based on modal values $\pm$ MAD using the 95 % percentile data are provided in Table 6.1. To exclude a gap between DIR3 and DIR4 a small adjustment, based on manual interpretation, was applied. The adjusted intervals, which we will use to categorise and estimate DIR by ICESat-2 photons, are also presented in Table 6.1.

6.1.2 Threshold-based estimation of DIR from ICESat-2

By using the classification scheme explained in Sect. 6.1.2, we classify the ICESat-2 geolocated photons into different DIR categories. The results are presented in Fig. 6.4. What is evident, and follows our expectations, is that ICESat-2 photons classified as DIR2 (slightly ridged) occurs in all of DIR zones as there will be areas with smoother surfaces, i.e. less ridged ice between actual ridges, in all of the higher DIR zones. It is also expected that DIR3 and DIR4 values will occur in DIR2 zones since even if an area has comparably little deformation, there will likely be larger individual ridges, however they are sparsely distributed.

Nonetheless, the general behaviour of the distributions of ICESat-2 DIR estimates follows the DIR polygons of the ice charts, i.e. Fig. 6.4a shows a collection of DIR4 classified photons close to and in the DIR4 polygon. Furthermore, the distribution of DIR3 classified measurements are larger in the southern part of the track (near the border of DIR4 polygon) compared to the northern part. Finally, the northern part has a lot of DIR2 categorised measurements, suggesting that this part is less covered by ridges. Since this value is only an amplitude parameter and based on one track, the surrounding behaviour of the ice are not known from ICESat-2 observations. Hence, the spatial behaviour of the ice may provide information on why this area still belongs to the DIR3 polygon from the ice chart which ICESat-2 cannot provide. Fig. 6.4b overall has more DIR4 observations from ICESat-2, even though it not classified as a DIR4 zone in the ice chart. This does not necessarily lead to the conclusion that this area is a DIR4 area, but it gives the idea of this DIR3 polygon zone to be significantly harder to navigate through due to large deformation. This is likely due to the measurements being close to the coast and compression

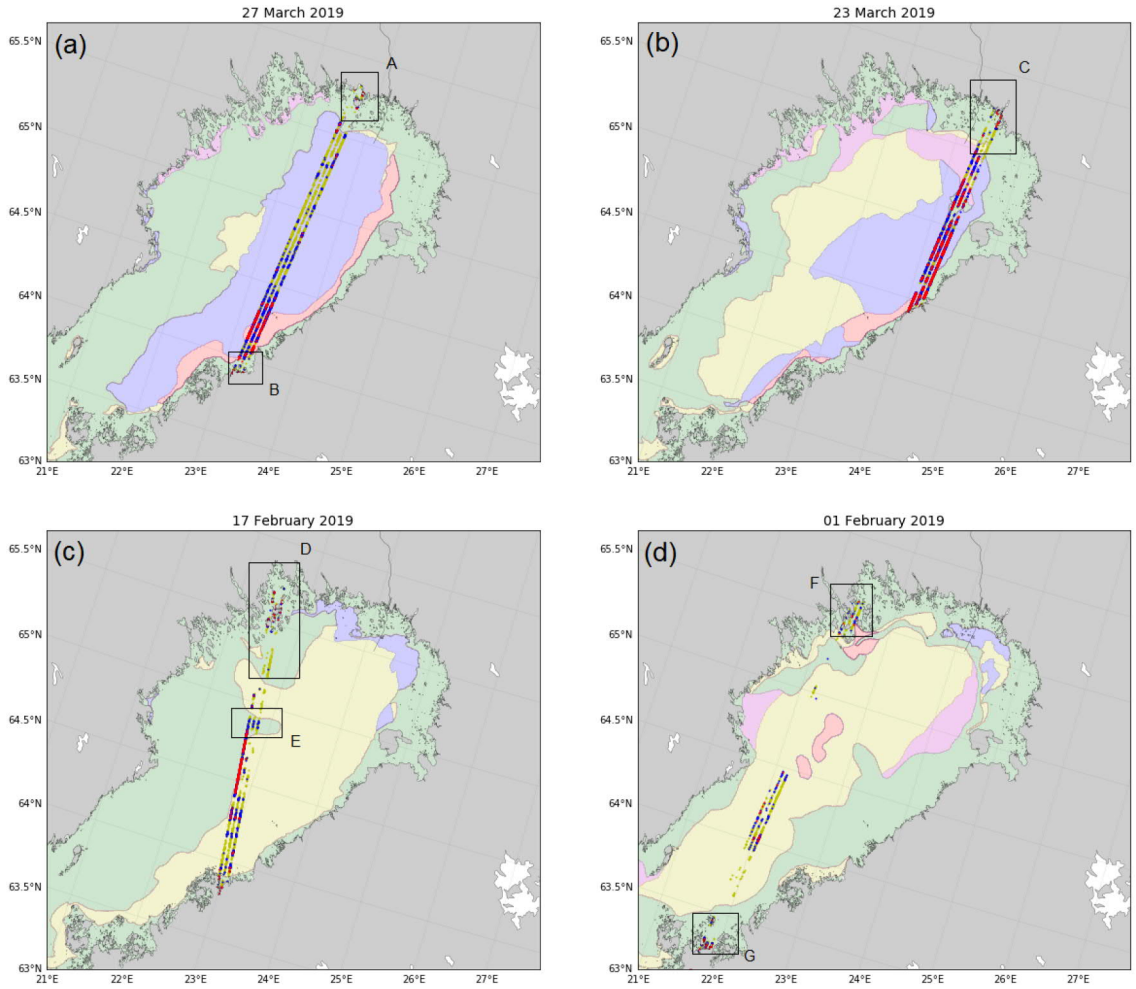

Figure 6.4: Categorised DIR data over four available days with somewhat cloud-free data; (a) 27 March 2019, (b) 23 March 2019, (c) 17 February 2019 and (d) 1 February 2019. Couloured polygons shows the DIR zones from the Finnish Ice Service (FIS) ice charts. The different DIR values based on ICESat-2 photons are shown in colours according to the polygons; DIR0 in green, DIR1 in magenta, DIR2 in yellow, DIR3 in blue, DIR4 in red. A-G denotes different areas of interest referred to in the text.

zone, so larger deformation in general occurs here. The ice will be pushed up towards the fast ice zone and the coast, which allows for the ice floes to build further and pile up to larger ridges.

What is also evident from all four days, is that when the track travels over fast ice regions, the DIR values are almost non-existent beside values over land. We expect this, as fast ice regions primarily consists of smoother ice represented by small differences between the average and highest elevation within a segment. For regions A-C (Fig 6.4a-b) and G (Fig. 6.4d) it is clear that the higher values are caused by values being measured over land. Area D and F (Fig. 6.4c-d) are behaving different than expected with DIR values occurring even though the track does not cover land. Some DIR2 values can likely also occur between the islands as there will likely be more deformation. Area E (Fig. 6.4c) shows higher ICESat-2 DIR values (DIR3 and DIR4) in areas not assigned a DIR zone or near the zone they belong to as defined by the ice chart. This can be caused by several things; it can be either background sun events that are higher than surface reflectance events or photons

tampered by low-laying clouds or possibly also by fog. It could also be caused by ocean waves, of significant wave height to be within in the adjusted intervals of ridges, crashing against the ice edge. This suggests that ice-ocean interactions observed by ICESat-2 to be investigated further.

We want to highlight that DIR zones estimated by photons from ICESat-2 are based on manual extraction of photons overlapping a specific DIR polygon in the ice charts. Since the polygons are based on a specific ice analysts interpretation of the ice data, it is to some extent subjective. Thus, the polygons may not necessarily be the actual truth. If a an area is misclassified as a DIR polygon, and the photons used in this study is based on a misclassified DIR polygon, this will be cause for misclassification of DIR from ICESat-2 photons. Thus, we propose a need for validation of DIR estimated by ICESat-2, e.g. by comparing with S-1 images similar to what we did when investigating surface roughness. If airborne laser surveys become available in the Baltic, this would also prove a reference data to estimate the accuracy of which ICESat-2 photons can estimate small-scale roughness.

The weakness of this method is the effect clouds or background events will have on the results. As mentioned earlier, the histogram filtering approach of ATL03 keeps photons flagged as surface by signal confidence, however the bins categorised as surface can still include some background photon events if the background rate threshold is too low for some of the background events. This can introduce a bias into the photon values used here, especially if a background sun event has a higher elevation than the highest surface elevation. Some photons may also be caused by a cloud cover that has not been entirely filtered out caused by e.g. low-laying clouds or fog. Thus, we propose to investigate further into the filtration of background events or photons reflected by cloud covers, especially if this method is to be automated. Clusters of mis-classified ICESat-2 events caused by cloud and/or background sun events, could possibly be applied a confidence flag to warn the ice analyst - this level of confidence can also be applied to DIR values affected by background events. Nonetheless, these results shows the potential of utilising ICESat-2 measurements to estimate ridging. Furthermore, it also suggests that ICESat-2 will be able to distinguish features at smaller scales than the resolution of SAR, which is very useful in ice charting, so a combination of SAR and ICESat-2 may also prove very interesting.

6.1.3 Segment-wise estimation of ridging

The results shown in Sect. 6.1.1-6.1.2 were based on the assumption, that higher values equals heavier ridging and that higher DIR zones are equivalent with higher ridge sails. Furthermore, we found threshold-based intervals when looking into the distribution of all relative elevations (highest elevation - mean elevation within segments of 150 photons) from each of the DIR zones. What we want to investigate now is the segment-wise estimation of ridging. This is based on the assumption, that about 95-97 % of the sea ice in the Baltic is in fact level ice (private communication, Rinne, 2020a), so only few values within a longer segment (e.g. a segment of 1 km) will actually represent a ridge (since ridges are approximately 3-5 m wide and the typical ridge spacing in the Baltic is 100 m (private communication, Rinne, 2020a)).

We have looked into the distributions of the photons within larger segments of $\sim$1-1.5 km (about 10,000 or 15,000 photons, however this is relative as it depends on the surface reflectance. Sea ice receive around 2.3-8.5 photons/shot (strong beam) compared to leads

that receive around 0.2-1 photons/shot (strong beam) (Markus et al., 2017)). First, we looked into creating a typical waveform describing the distribution of photons within a longer segment. To ensure the highest values, of which we resume are reflections of ridges, and the measurements of level ice are kept, we must order the data in an appropriate manner. We have ordered the values within each segment from the highest to the lowest. To estimate which parameter that provides most information about ridging, we look into segments of all the measured elevations within a segment, all elevations subtracted the mean of that segment (assuming the mean is a measure of the height of level ice) and all elevations subtracted the median value of that segment (assuming the median is instead a measure of the height of level ice). For all of the segments (and the three relative elevations; purely elevations, max-mean and max-median), we generate a typical distribution by for each column extracting the mean and the median as a typical value of the elevations, see Fig. 6.5.

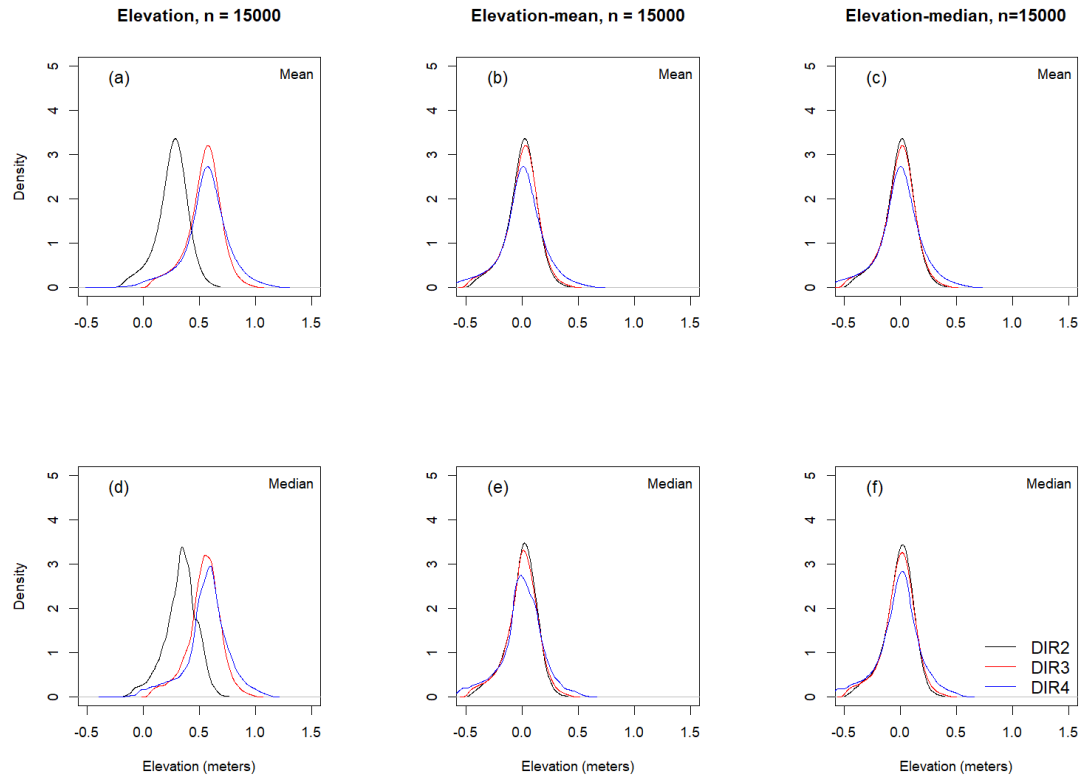

Figure 6.5: Typical distribution of relative elevations (actual photon elevations, photon elevations with elevations subtracted the mean value and photon elevations subtracted the median). (a) and (d) shows the typical distribution by actual photon elevations by using the mean and median, respectively. (b) and (e) shows the typical distribution for photon elevations with the elevations having the mean value subtracted, and by using the mean or median to estimate the typical distribution, respectively. (c) and (f) shows the typical distribution relative elevations (elevation - median) by mean or median, respectively. Black denotes DIR2, red is DIR3 and blue is DIR4.

In Fig. 6.5a and Fig. 6.5d we see the typical distribution of the elevation measurements calculated by mean and median, respectively. Fig. 6.5a shows a large difference between DIR2 and DIR3/DIR4. As we were assuming a distribution, where the values of level ice were similar in all of the distributions, but only the tail were different (changing with the different DIR), this is not what we expected. It is probably because the measurements

are taken different places within the Bothnian Bay and elevation values of DIR2 zones generally being smaller, since there are more open water areas, than areas with a constant ice cover, this will be evident in the data. Thus, the geolocated photons without any subtraction of a level ice surface does not provide any sufficient information. Fig. 6.5b and Fig. 6.5e shows the typical distributions of relative elevations by subtracting the mean (as a measure of level ice surface) from the elevations. For both graphs the distributions follows a similar pattern shape with level ice measurements being close to 0.0 m. The difference between the tails, describing the difference between the DIR zones by amplitude of the ridges, are less significant. Only DIR4 seems to be possible to clearly distinguish from the other DIR zones. DIR3 is slightly higher than DIR2. We have also looked into typical distributions of relative elevations determined by subtracting the median from the elevations. Since the distributions of the photon measurements within a segment is right skewed, the typical distributions estimated by average values of the columns (Fig. 6.5a-c) are more likely to be affected by outliers (higher ridging values) and by clusters of values, whereas the median provides the middle value of the data set.

Using the median value, we get a measure that is less affected by outliers, which is also why it is possible to get a small distinction between DIR2 and DIR3 when using relative elevations where the level ice (either by mean value or median value) are subtracted. There seems to be just slightly larger difference between the distributions in Fig. 6.5f compared to Fig. 6.5e (both between DIR2 and DIR3, and between DIR3 and DIR4), so using elevation measurements subtracted the median suggests to be the best estimate for

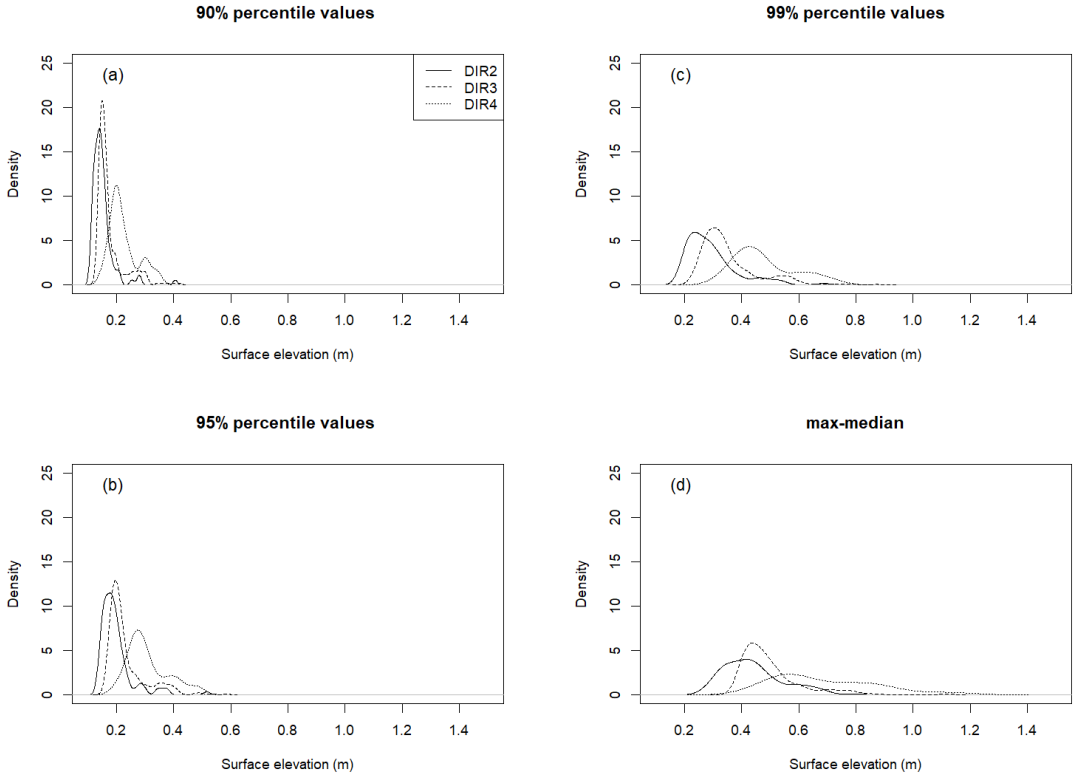

Figure 6.6: Distribution of the highest values within a segment. (a) 90 % percentile values based on elevation-median estimations, (b) 95 % percentile values based on elevation-median estimations, (c) 99 % values based on elevation-median estimations and (d) distribution of maximum-median values.

distinguishing between DIR zones in larger segments. This may also apply to the DIR estimation we did by using $N = 150$ photons in each segment, but has not been investigated further. However, since the difference is not too significant, subtracting the mean as a measure of level ice is also valid (as has been done in Sect. 6.1.1-6.1.2).

Since it is the tail that shows a difference in DIR zones, it can be assumed that looking into the highest values within one segment, that it should possible to distinguish between the different zones. Therefore, we look into four different methods of finding the highest value: three methods based on percentile values of elevations with median value subtracted (assuming median value is a measure of the level ice) and the last method is based on measuring the highest value with the median subtracted. The distributions of these are shown in Fig. 6.6.

From Fig. 6.6a-b, we see a clear distinction between the highest DIR zone (DIR4) with the lower DIR zones (DIR2 and DIR3). We expected this from Fig. 6.5f too. It suggests that DIR4 has significantly higher ridges than DIR2 and DIR3, thus the ice is especially more deformed here. In addition, it suggests that DIR2 and DIR3 are areas with similar heights of ridges. These results does not provide spatial measures of ridging, which is also one of the aspects that separates the DIR zones. Hence, it could very well be what separates DIR2 and DIR3 from each other over longer segments.

Finally, Fig. 6.6c shows a clearer separation between the different zones. From this, it can be concluded, that by 1 % of highest values it is possible to find a clearer distinction between the different DIR zones over longer segments. Looking into the final measure of ridging (max-median, Fig. 6.6d), which is a similar approach as used in the first DIR discrimination, the overlap is not as clear as in Fig. 6.6c. This may be caused by e.g. erroneous photons from cloud reflections or from background events. Thus, this method could possibly work around one of the weaknesses of the method used in DIR estimation based on shorter segments ($N = 150$).

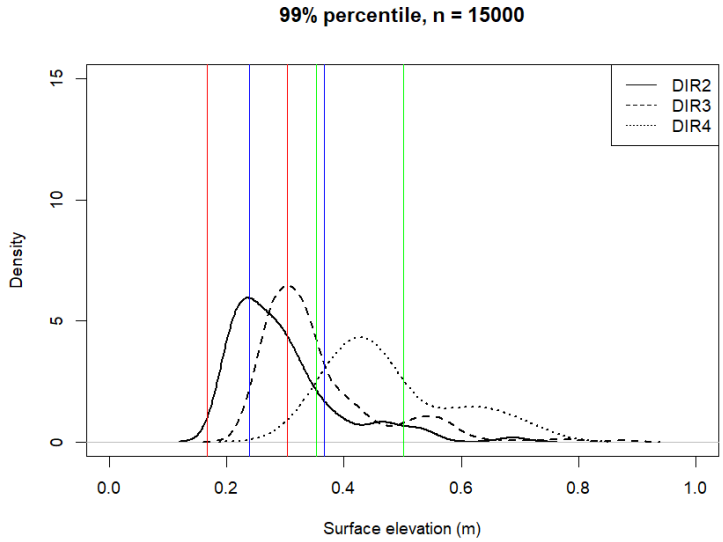

Figure 6.7: Distribution of 99 % percentile values based on segments of elevation-median values. Filled line is DIR2, dashed line is DIR3 and dotted line is DIR4. Red vertical lines note the threshold-based interval (modal value $\pm$ MAD) of DIR2, blue vertical lines is the interval for DIR3 and green vertical lines for DIR4.

With the 99 % percentile distributions showing the clearest distinction between DIR zone, it proves the most promising data to use for estimating threshold-based intervals, similar to the DIR estimation of smaller segments. When estimating the threshold-based intervals (modal $\pm$ MAD) it is clear, that it is not possible to determine threshold-based intervals that do not overlap, see Fig. 6.7. Not even a intervals between DIR3 and DIR4 could be established without an overlap even though the distinction between the distribution is largest here. Thus, it can be concluded that while it is possible to distinguish DIR zones with segments longer than $N = 150$, the overlap is to significant to determine non-overlapping intervals to classify by. But, the most significant conclusion that can be drawn from both studies on DIR is the potential that ICESat-2 photon measurements show in estimating small-scale surface roughness features such as pressure ridges in the Baltic from space-borne instruments.

One may have noticed that the distributions used here are based on segments of 15000 photons ($\sim$1.5 km). This was the largest segment we could retrieve from all areas. It should be highlighted, that at 10000 the distribution was somewhat similar. Furthermore, the analysis also looked into smaller segments (photons of 500, 1000, 1500, 5000 etc.), but the largest separation of perccentile values from each segment was first achieved at 10 000 photons or more. It would be interesting to see how the distributions look if longer segments over different DIR zones are available.

6.2 Shallow water bathymetry in the Baltic and Danish Sounds

Here we present the capability of ICESat-2 to measure bathymetry in the Baltic Sea and Danish Sounds and compare the results with depth profiles from BSBD data base. Furthermore, a comparison with Secchi depths from HELCOM ICES data set is presented.

6.2.1 Empirical depth mapping performance

The objective with reference to shallow water bathymetry, was to show a proof-of-concept of bathymetric measurements in the Baltic Sea. As explained in the Sect. 5.2, we have looked at short transects from four different areas to investigate if bathymetric measurements were possible in the Baltic. We conclude that it was possible to empirically find bathymetric measurements from all four areas. We will investigate the four tracks one by one.

Bathymetric measurements from Kattegat are shown in Fig. 6.8. Fig. 6.8a shows a $\sim$33 km transect from ICESat-2. Clear bathymetric measurements of a transect of more than 10 km is seen with depths down to 7 m. When comparing with depth profiles of BSBD, clear features are seen (the depth profile is flipped), e.g. the very short, but deep, feature seen between 0-5 km in Fig. 6.8d, which is to some extent, however not as deep, seen before 57°N in Fig. 6.8a, denoted by the yellow boxes. The same can be said about the very clear spiky feature seen around 24 km in Fig. 6.8d, which can also be seen in Fig. 6.8a just before 56.8°N. This specific spiky feature also seems to be around the same depth ($\sim$2 m depth, without refraction corrections) as on the depth profile. The spiky features are denoted by green boxes. In Kattegat, with this track, measurements down to $\sim$7 m could be seen in beginning of April. However, these measurements does not show to what depths bathymetry can be measured, as the measurements were shallow and in-between coastal areas. When looking into additional tracks, depths up to 10 m (in mid

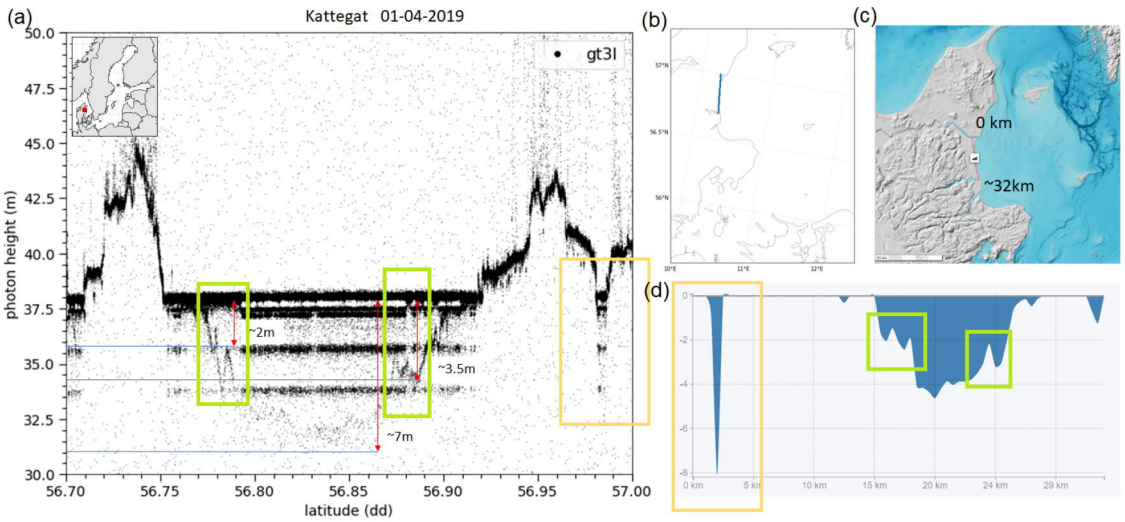

Figure 6.8: Bathymetric measurements from ICESat-2 and depth profile from BSBD acquired over Kattegat. (a) ∼33 km transect of ATL03 photons from ICESat-2 (strong beam, GT3L) with approximate location on a map in the left corner, (b) map of ICESat-2 track, (c) map of depth profiles from BSBD manually drawn, and (d) depth profile from BSBD. Yellow and green boxes denotes observations referred to in text.

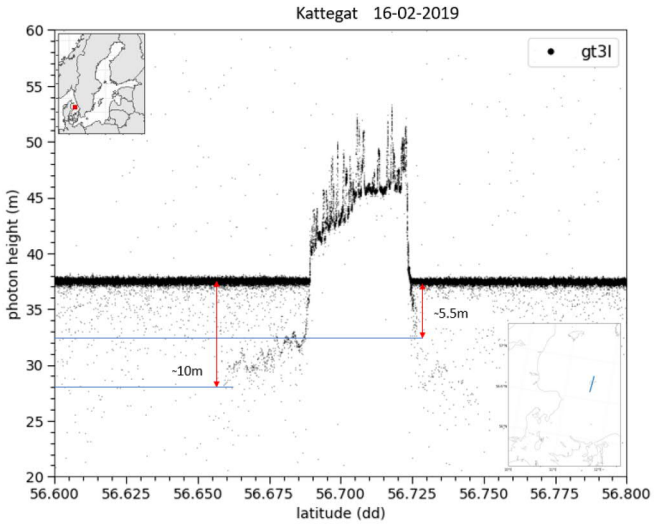

Figure 6.9: Bathymetric measurements from ICESat-2 (strong beam, GT3L) over a ∼22 km transect of the overpass. Land cover is the island of Anholt. Top left corner is the approximate location of this track and lower, right corner is the exact track of ICESat-2.

February) were seen near the Island of Anholt in Kattegat (Fig. 6.9), before ICESat-2 seafloor reflections disappears on the downward-sloping seafloor.

The constant horizontal segments of photons, as can be seen on Fig. 6.8 (and for Oulu, see Fig. 6.11), beneath the water surface is already a known issue to the ICESat-2 team. From their *Known Issue* document (available on https://nsidc.org/sites/nsidc.org/files/technical-references/ICESat2_ATL03_Known_Issues_v002.pdf), they state that this effect is seen over calm ocean surfaces where surface winds can be neglected. Their investigation shows, that this is likely caused by small after-pulses in either the transmitted pulse of ATLAS or electronic noise following the arrival of the primary surface return. It is usually shown over inland water or leads where the open water surfaces are smooth, which

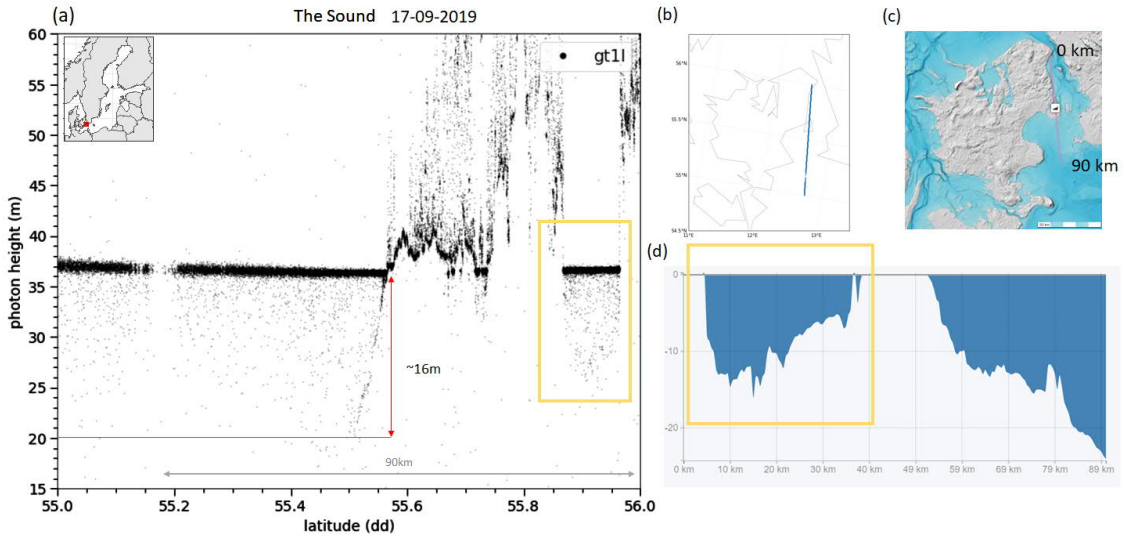

Figure 6.10: Bathymetric measurements from ICESat-2 and depth profile from BSBD acquired over The Sound. (a) ∼111 km transect of ATL03 photons from ICESat-2 (strong beam, GT3L) with approximate location on a map in the left corner, (b) map of ICESat-2 track, (c) map of depth profiles from BSBD manually drawn, and (d) depth profile from BSBD. Yellow box denotes observations referred to in text.

is also what we recognise in these plots where both areas are inland water or contained by several islands. We will discuss the affect of these after-pulses in terms of automatic detection of bathymetric measurements in Sect. 8.2, but will for now just conclude that this is a feature that can be seen. Furthermore, if one is to manually choose a photon as a bathymetric measurements, one can - as best as possible - choose to not include these horizontal layers.

For the Sound (Fig. 6.10), we found clear bathymetric observations from ICESat-2 down to approximately 16 m before the seafloor detections were no longer visible. The depth profile from BSBD show a similar downward slope. We also see scattered photons in the water column between 55.8°N-56.0°N, but cannot conclude whether the photons from the barriers of that basin is clear enough as seafloor depth measurements or if it is scattering of all the photons within the water column that provides us with an idea of how the basin looks. It may just mean, that the photons are too scattered in this small basin, maybe caused by increase in phytoplankton or other particles, to provide an idea of the bathymetric measurements. Nonetheless, even though it does not give exact bathymetric measurements that can be distinguished from the scattered photons, the scatter still provides us with an idea of the size and depth of the basin.

The ICESat-2 measurements found in the Danish Waters were the only ones, where reasonable depth profiles from BSBD were available for comparison. We assume this is due to the different resolutions of the measurements depending on the country of which they originate from, e.g. Finland has stricter restrictions in territorial waters, where values are only based on nautical charts, rather than models or satellite measurements. Nautical charts can be restricted by the government in terms of what information should be available as public information. Thus, we will in the next part of this section, where we look into bathymetric measurements from Archipelago Sea and the Bothnian Bay, not make comparisons with depth profiles of BSBD, since depth profiles were not directly available.

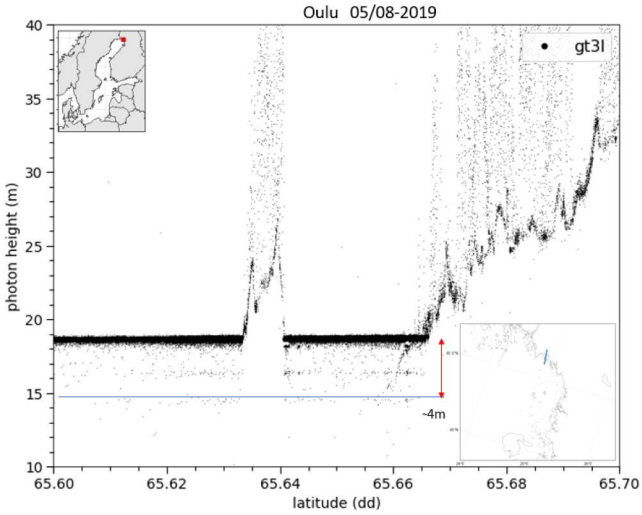

Figure 6.11: An ∼11 km transect of bathymetric measurements from ICESat-2 of the Finnish side of the Bothnian Bay, near Oulu. Image in top left corner shows the approximate area of this measurements, and lower, right corner shows the exact track including which islands it encounters.

For Oulu (the Finnish side of the Bay of Bothnia, see Fig. 6.11), bathymetric measurements can be seen down to approximately 4 m near the coastal zone acquired over inland waters. This is significantly lower than in the Danish Waters, nonetheless is it still in tune with our expectation of the Danish Waters having clearer waters which can lead to deeper bathymetric measurements. Thus, it suggests that ICESat-2 can retrieve even deeper depths if the conditions allows for it.

The conditions have shown to allow for deeper measurements near Luleå, in the Bothnian Bay but in the Swedish side, see Fig. 6.12. On this ∼11 km transect several bathymetric features can be seen - from continuous measurements between 65.20-62.21°N to sudden,

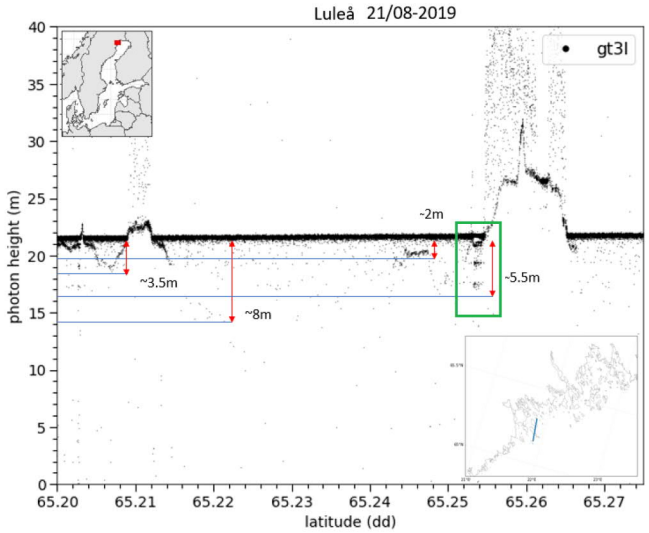

Figure 6.12: A ∼11 km transect of ICESat-2 geolocated photons with nearshore bathymetry and afterpulses shown acquired near Luleå.Image in top left corner shows the approximate area of this measurements, and lower, right corner shows the exact track including which islands it encounters. Green box denotes observations referred to in text.

but clear, low level bathymetric features around 65.24-65.25°N. Again, some after-pulses can be seen between 65.25-65.26°N (Fig. 6.12, green box). This seems to be caused by a *very* shallow area, almost confined by a bathymetric spike just before the pulse (Fig. 6.12, green box). Again, this follows the assumption of when after-pulses occurs. The deepest, but very sparse, bathymetric measurements seen on the Swedish site is down to ∼8 m, but the most defined are around 3.5 m (similar to the depths of Oulu).

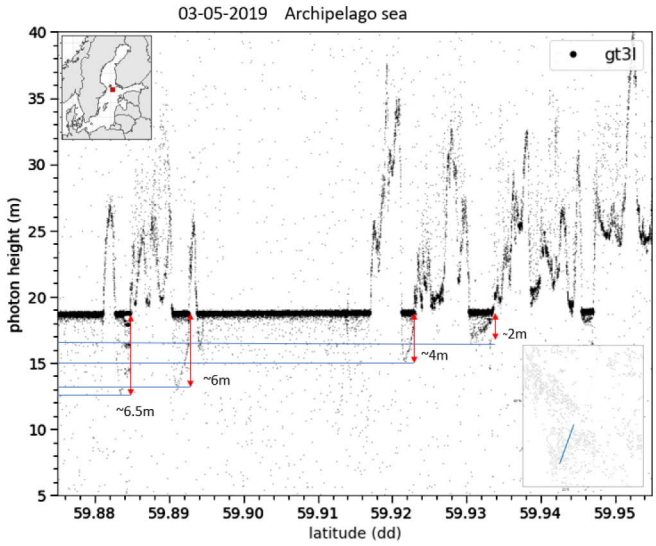

Figure 6.13: Transect of ∼7 km geolocated bathymetric photons from ICESat-2 acquired over the Archipelago Sea.Image in top left corner shows the approximate area of this measurements, and lower, right corner shows the exact track including which islands it encounters.

Finally, we have bathymetric measurements acquired over the Archipelago Sea near the Åland Islands. This one is especially interesting, as we know this is one of the shallowest areas in the Baltic. Again, in between islands (inland waters), we see lots of bathymetric measurements of a transect about 11 km long. The deepest of the measurements go as deep as ∼6.5 km between 59.88-59.89°N, were also after-pulses are once more spotted. For larger open area waters no bathymetric observations are retrieved. This may be caused by the eutrophicated waters and increased production in these water or by the sediment substrates of this specific basin (an effect that will be discussed in Sect. 7).

We can conclude from these observations that it is possible for ICESat-2 to retrieve shallow water bathymetry in the Baltic and Danish Sounds. Shallowest, but clear, maximum

Table 6.2: Sites used to estimate bathymetric depth capability. The declaration of inland water body is used to explain whether this measurements can be used as a declaration of the maximum depth from this area or if it is confined by coasts suggesting that the depth cannot be lower than this

Site	Location by range of latitude [dd]	Date of ICESat-2 overpass [dd-mm-yyyy]	Inland water body [yes/no]	Maximum observed depth (No refraction correction) [m]
Kattegat (near Jutland)	56.700-57.000	01-04-2019	Yes	7
Kattegat (near Anholt)	56.600-56.800	16-02-2019	No	10
The Sound	55.000-56.000	17-09-2019	No	16
Bay of Bothnia (near Luleå)	65.200-65.300	21-08-2019	Yes/No	8
Bay of Bothnia (near Oulu)	65.600-65.700	05-08-2019	Yes/No	4
Archipelago Sea (near Kökar)	59.885-59.955	03-05-2019	Yes	6.5

bathymetric observations were acquired in The Bay of Bothnia (near Oulu) at 4 m depth and the deepest depths were acquired in The Sound at 16 m depth. A summary of all maximum depth measurements and whether these were coastal, inland water areas or open sea is provided in Table 6.2.

It is known that water clarity is an important factor when trying to achieve bathymetric measurements from a laser pulse, both airborne, but also now spaceborne. We want to assess how well ICESat-2 retrieved bathymetric measurements as a function of water clarity. We do this, by investigating Secchi depths measured in the Baltic Sea and Danish waters.

6.2.2 Secchi depths as water clarity proxy to estimate bathymetric possibilities

To investigate the water clarity, we use Secchi depths as a proxy and look into the water clarity from different areas of bathymetric interest in the Baltic Sea and the Danish waters, similar to the analysis of Parrish et al. (2019). The Secchi depths used in this study is not from the same date as the ICESat-2 overpass, but rather from a time period with first measurements acquired in 1975, though with the majority of measurements being after 1980, and ending in 2018 at the latest. It is worth mentioning that the Secchi depth measurements used in this study are *actual* Secchi depth measurements acquired at sea. Secchi depths used in Parrish et al. (2019) are a product of empirical relationships between Secchi depths and the diffuse attenuation coefficient, K_d, as mentioned in Sect. 5.2, acquired the exact same day. We will compare with statistical parameters of the data sets to investigate the bathymetric capabilities of ICESat-2 in the Baltic and Danish Waters.

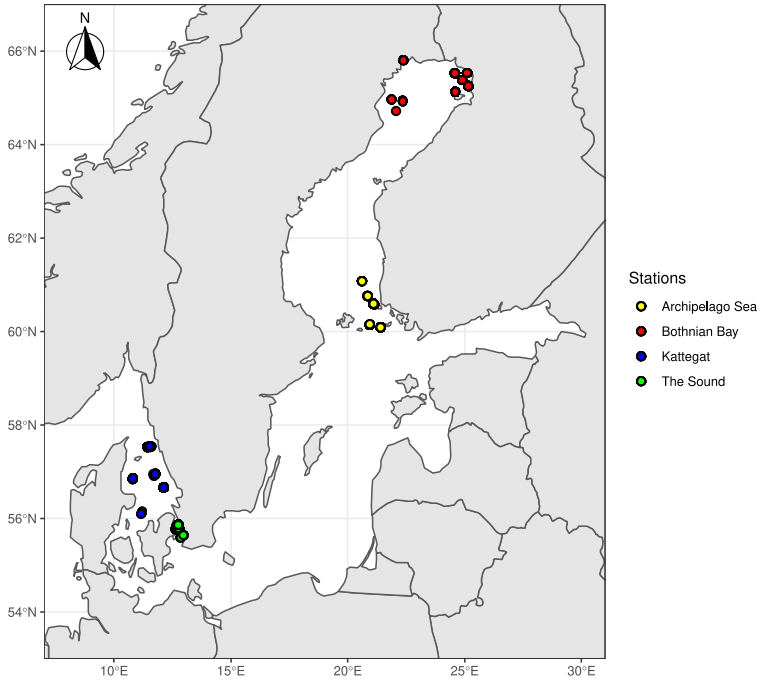

Figure 6.14: Locations from different Secchi depth locations from HELCOM ICES. Stations are shown by colours of blue, green, yellow and red which is Kattegat, The Sound, Archipelago Sea and the Bay of Bothnia, respectively.

The locations of the Secchi depths are provided in Fig. 6.14 and a summary of the Secchi depth measurements are provided in Table 6.3. Observation depths alongside a yearly

average (with confidence level of standard deviation) is shown in Fig. 6.15. What is evident for both Fig. 6.15 and Table 6.3 is that Kattegat and The Sound generally has significantly clearer waters than the Bothnian Bay or Archipelago Sea. This is similar to our expectations and assumptions. With maximum depths of 18 m (Kattegat) and 16.5 m (The Sound) compared to 10.8 m (Archipelago Sea) and 9 m (Bothnian Bay), it is very clear that the the Danish Waters are in fact clearer than the Baltic. However, we want to mention that the measurements in the Baltic can be slightly shallower than actually due to the correction from centimetre to meter we had to apply (see Sect. 4.3.3).

Table 6.3: Statistical parameters on Secchi depth observations from Kattegat, The Sound, Archipelago Sea and the Bothnian Bay.

Site	Number of observations	Minimum [m]	Maximum [m]	Mean [m]	Median [m]	Mode [m]
Kattegat	1052	2.5	18	8.06	8	7.94
The Sound	1044	1	16.5	8.30	8	7.82
Archipelago Sea	538	2	10.8	5.06	4.7	4.51
Bothnian Bay	844	0.5	9	3.10	3	2.89

To understand exactly how to use this data as evaluation data, we divided the data into monthly values, as we assume the Secchi depth changes with time and that usually, the processes, such as e.g. algae production which can hamper water turbidity, occurs approximately at the same time each year. Maximum, minimum and average depth for each month is shown in Fig. 6.16. Dividing the values by monthly averages and maximum may also provide an idea of when the bathymetric measurements are most likely to be available. Based on average measurements from Kattegat, measurements up to about 7 m should be possible to measure (with February having the smallest average depth of 6.93 m). Summer/late summer (July, August and September) have the highest average values of 8.47 m in July, 9.29 m in August and 8.95 m in September. For the Sound, the average values were highest during Spring (8.63 m in February and March, 10.3 m in April and 8.97 m in May) and in beginning of Winter (8.64 m in November, 8.49 m in December and 8.47 m in January). Archipelago Sea has the highest average values in winter (January with 5.17 m, February with 5.51 m and March with 6.33 m). For the Bothnian Bay, the average values are highest around winter and summer (5.88 m in January, 3.14 m in December and 3.47 m in November; 3.13 m in July, 3.79 m in August and 3.3 m in September). For the Bothnian Bay, the higher depths during winter time is following the general expectation of waters being clearer in winters, since colder temperatures can allow for less nutrients and production, with little mixing of the water column, however phytoplankton growth is also seen during winters, so this is not always the case (Stenseth et al., 2004). Generally, the maximum depth throughout the years follows a similar pattern as the average depth. For Kattegat, the maximum value measured was in September of 18 m, in Archipelago Sea it was in March of 10.8 m, for The Sound it was 16.5 m in April and the Bothnian Bay had a maximum depth of 9 m in November. We have also included the minimum depth to show the range of which bathymetry should be possible to measure. Kattegat had an absolute minimum value of 2.5 m in January. The minimum depth in the Sound was found in March of 1 m. For the Archipelago Sea the minimum depth was 2 m and for the Bothnian Bay was 0.5 m. Once again, we would like to emphasise that values below 1 m should be taken with care, as this may have been caused by the pre-processing step we

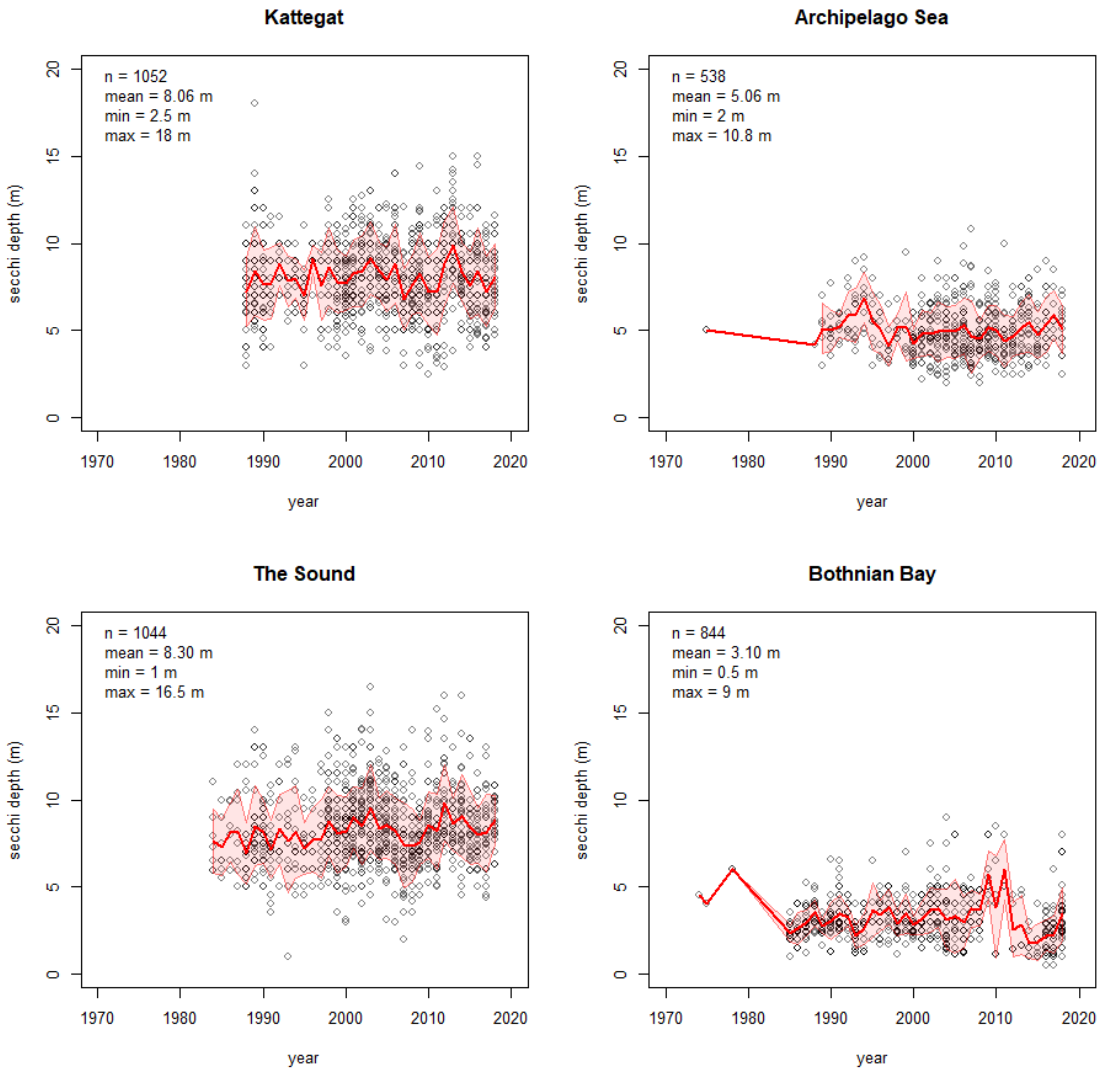

Figure 6.15: Secchi depth measurements from Kattegat, The Sound, Archipelago Sea and Bothnian Bay retrieved from HELCOM ICES acquired during the period of 1975-2018. In each graph amount of observations (*n*) alongside average (*mean*), minimum (*min*) and maximum (*max*) Secchi depth of observations from each site are given. Bold, red line is the yearly average value and filled, transparent red area shows $\pm$ standard deviation.

applied to assume the measurements being meters and not centimetres.

While the maximum depth may be useful to compare to ICESat-2 derived bathymetric measurements, the maximum depth is merely a snapshot of the specific conditions at a specific time where conditions are favourable for retrieving bathymetry. The average value is a general, typical value of the turbidity and clarity of the water in that area, but there is the possibility that the conditions favours clearer water depths than the average depth, such that ICESat-2 can, on that specific day with cloud-free skies, retrieve depths that are deeper than the average Secchi depth. The minimum depth can provide an idea of what bathymetric seafloor measurements ICESat-2 should *at least* be able to retrieve.

To understand the depth capability of ICESat-2 in the Baltic and Danish Waters, we have analysed the maximum depths (not corrected for refraction) for all of the sites, as provided

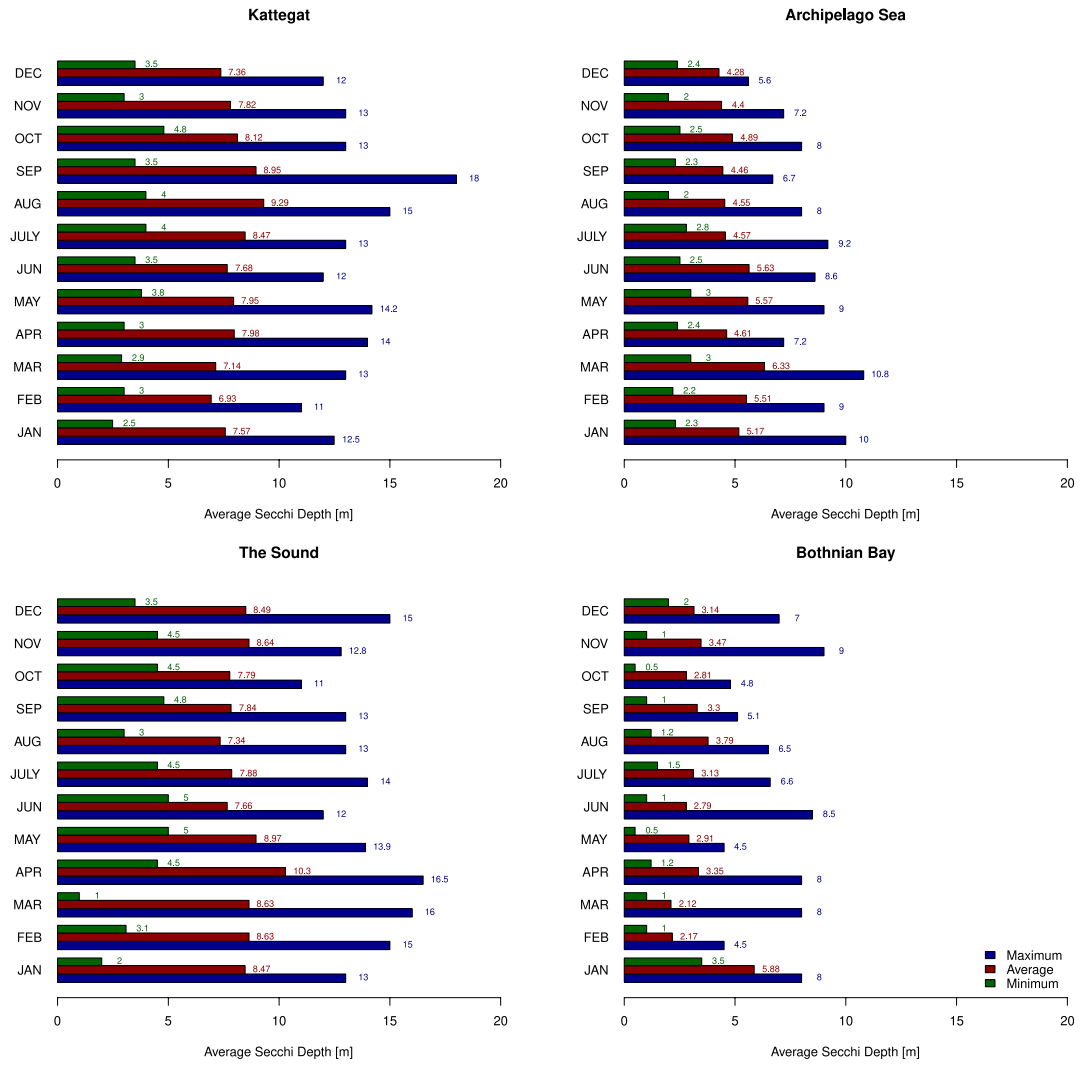

Figure 6.16: Maximum, minimum and average monthly Secchi depth measurements from Kattegat, The Sound, Archipelago Sea and Bothnian Bay retrieved from HELCOM ICES acquired during the period of 1975-2018. Each graph shows a bar as the maximum, the minimum and average Secchi depth by months with the exact value written beside.

in Table 6.4. The results show, that for the six areas tested, the maximum depth penetration was (based on monthly averaged, $Z_{SD,avg}$) 1.41±0.53 and 0.87±0.31 (based on monthly maximums, $Z_{SD,max}$). This generally shows that based on maximum monthly values, the maximum penetration of 0.87 Secchi depth provides a reasonable shallow depth range allowing for ATLAS to retrieve up to 15.66 m in Kattegat, 14.36 m in The Sound, 9.40 m in the Archipelago Sea and to 7.83 m in the Bothnian Bay if the conditions are favourable for clear waters. As can be shown in e.g. The Sound and the Bothnian Bay (near Luleå), depths can be retrieved even deeper than the monthly maximums (though below the absolute maximum measured from each area throughout the years of 1975-2018 of; 18 m in Kattegat, 16.5 m in The Sound, 10.8 m in the Archipelago Sea and 9 m in Bothnian Bay). The fact that two areas were significantly higher than the average monthly value (2.04 in Kattegat and 2.11 in Bothnian Bay (Luleå)) and than the maximum monthly value (1.23 in both Kattegat and Bothnain Bay, Luleå) is also an indication that there were favourable conditions and clearer waters during those days. Since the HELCOM measurements are

not constant throughout the year, but usually based on trials and missions, depths from all dates throughout the year will not be recorded. Thus, there may be clearer waters which simply have not been recorded yet.

Table 6.4: Maximum observed bathymetric depths (without refraction corrections) observed by ATLAS on board ICESat-2 from the chosen sites, along monthly averaged and maximum depths Secchi depths and maximum penetration in relation to the maximum and averaged Secchi depths.

Site	Maximum observed depth [m]	Monthly averaged Secchi depth, $Z_{SD,avg}$ [m]	Max penetration in Secchi depth, monthly mean	Monthly maximum, Secchi depth, $Z_{SD,max}$ [m]	Max penetration in Secchi depth, monthly max
Kattegat (near Jutland)	7	7.98	0.87	14	0.50
Kattegat (near Anholt)	10	8.95	1.18	11	0.91
The Sound	16	7.84	2.04	13	1.23
Bay of Bothnia (near Luleå)	8	3.79	2.11	6.5	1.23
Bay of Bothnia (near Oulu)	4	3.79	1.06	6.5	0.62
Archipelago Sea (near Kökar)	6.5	5.57	1.17	9	0.72
Mean	**8.58**	**6.32**	**1.41**	**10**	**0.87**
Standard deviation	**4.19**	**2.25**	**0.53**	**3.2**	**0.31**

Once more would we like to emphasise, that none of the maximum observed depths have been corrected for refraction corrections. So, especially for the deeper observed ICESat-2 depths, there most likely be a reduction in the depths after having applied the refraction corrections, suggesting that the maximum optical depth most likely will decrease. We assume the maximum refraction correction to be applied in the Baltic is of 5 m at depths of 20 m, but it is more likely to range from 1-2 m in depths up to 10 m (see Sect. 8.2). Nonetheless, this study does provide an overall idea of how well ATLAS will be able to retrieve depths and to what extent, which assuming favorable conditions will be up to 87 % of the monthly maximum depth based on HELCOM ICES Secchi depths.

7 Discussion

This section includes the discussion of the results in relation to the research questions formulated for this thesis.

7.1 Research questions

For this dissertation, we formulated three essential research questions associated with the objectives and which founded the basis of the dissertation. Here, we will answer the questions and present the most important findings (based on the results already explained), highlight some aspects which has not been included in this study and suggest improvements to the work presented here. Furthermore, in relation to this discussion, we will go in detail with some future considerations and work that could be done based on these findings in Sect. 8.

Q1 How do ICESat-2 measurements over the Baltic compare with operational ice charts?

The operational ice charts analysed daily by FIS provides information on minimum, maximum and average ice thickness, sea surface temperature, sea ice concentration and type and lastly a measure of DIR. Remote sensing measurements to estimate sea surface temperatures and concentration can be derived from passive microwave observations from radiometers (Matthews et al., 2020; Pearson et al., 2019). Ice types in FIS ice charts are based on two measures: (1) concentration (e.g. very open ice with a concentration of 1-3/10 versus consolidated ice with a concentration of 10/10) which can be retrieved from passive microwave observations and (2) ice drift (here, one discriminates between drift ice and landfast ice) (Berglund and Eriksson, 2015). Elevation observations from space, i.e. from ICESat-2, can be used to estimate two measures relevant for comparison with the ice charts: sea ice thickness and pressure ridges to estimate DIR.

Due to the current restrictions of the ICESat-2 measurements in terms of availability of a freeboard product (ATL10) in the Baltic, it has not been possible to compare ICESat-2 derived ice thickness with the values of operational ice charts. We could have presented a method of retrieving sea ice freeboards from the ATL03 data product ourselves. This is however a tidy process, as we would have to reduce the noise in the ATL03 data product (since we know, that the photon products can be disturbed by background photon events, clouds and/or scattering at the surface), detect and estimate leads in the photon measurements and thereafter retrieve the freeboard heights which still needs to be compared with snow depth uncertainties and may even be too much work for a five months Master's thesis. Furthermore, since the ATL10 (freeboard product) currently does not produce freeboards in conditions <50 km from coastlines and with ice concentrations <50 %, it would be highly unlikely that we would have been able to generate, produce and validate an algorithm that works better than the current algorithm. Thus, it has not been possible to compare sea ice thickness values with operational ice charts. However, we have given the matter some thoughts and do provide ideas and suggestions to be taken into account for when ATL10 becomes available in the Baltic Sea in Sect. 8.

We would also like to highlight that when freeboards, which can be converted into thickness values assuming hydrostatic equilibrium (Skourup, 2010), become available in the

Baltic Sea, it would be as continuous thickness measurements and not as polygons with a thickness range (e.g. 10-50 cm) which is presented in the ice charts. Hence, when one compares the ice charts and the ice thickness observations, it would simply be a comparison of how well the ICESat-2 thickness values compare with the thickness range given in the photons - and not with direct comparisons within polygons.

This leads us to the last observations to be retrieved from ICESat-2 to compare with the ice charts: DIR. With the method we have proposed to estimate DIR from ICESat-2, there seems to be an overall similarity with the ice charts. As we stated, lower DIR values occurs in higher DIR zones simply because ridging and deformation does not occur everywhere in the DIR zone. The same can be said about larger DIR values that will occur in lower DIR zones too as there will occur some heavy ridging there, although it will be more sparse compared to higher DIR zones. Thus, ICESat-2 provides information of DIR at scales with more details than provided within the ice chart derived polygons.

We especially see high DIR near the island of Hailuoto and the coast or the shoreline of landfast ice. This is to be expected, as the drifting ice can be crushed against grounded, stationary (i.e. landfast) ice, increasing the piling of ice. This suggests that the method generally provides information on the deformation in the area by assuming that large relative elevations (highest value with the mean elevation subtracted) is a measure of higher DIR zones. As stated before, the method has weaknesses. Currently, it assumes the highest elevation to be the reflection of the highest point of the ridge. The highest photon may also be caused by background photon events or photons disturbed by clouds. Furthermore, scattering from the surface can also mean that the highest value is in fact not from the ridge but from photons scattering on the piled blocks or if the snow of a dry snow cover is present. A need for reduction of possible noise should be investigated as well as the possibility of eliminating background events and cloud disturbed photons even more than has already been applied in the pre-processing.

In this study, we have estimated the DIR zones by extracting ICESat-2 photons that crossed a specific DIR polygon in the ice charts. However, as already stated, the polygons are drawn by ice analysts and even though they are based on ice breaker and SAR data, they are subjective to the ice analysts interpretation of the data. This means, that if polygons have been misclassified and we have utilised those misclassified DIR polygons for extracting photons, which we assume is from that DIR polygon, our DIR estimated will become misclassified or biased. Thus, additional validation is necessary.

Q2 Can ridging features (DIR in ice charts, ridge density and/or sail heights) be distinguished from the ICESat-2 data?

We have proposed a method to estimate DIR from ICESat-2 and shown, that by selecting the 5 % highest photon values it has been possible to distinguish three DIR zones (DIR2 = slightly ridged, DIR3 = ridged and DIR4 = heavily ridged ice) from each other with little overlap. This was based on ICESat-2 data overlapping the respective DIR zones provided in the FIS ice charts. From the distributions we were able to make a simple, threshold-based discrimination of DIR. So yes, we conclude that it is possible to detect ridging features from ICESat-2 (in small scale such as ridges in the Baltic, which on average has a sail height around 0.5 m (Lewis et al., 1993)). However, we will also like to highlight that the ridges has not been validated by ground truth measurements other than ice charts which are somewhat subjective based on the ice analysts interpretation of the data. In

general, studies of validated detection of ridges from ICESat-2 has not yet been published yet, so it is not known if ICESat-2 can detect small-scale ridging features such as sail heights and ridge density in the Baltic with high enough precision. Thus, we conclude that ridging features such as DIR was possible to distinguish based on the distribution of relative elevations (highest elevation with the mean elevation subtracted in segments of $N = 150$ photons).

Using SAR imaging as a validation source also highlights the important and interesting information that a combination of SAR and ICESat-2 can provide. Since Gegiuc et al. (2018) have showed the possibility of automatically detecting DIR zones from SAR imaging by combination of parameters extracted from SAR images, it would be interesting to investigate the information that a combination of high-resolution ICESat-2 photon elevations and SAR imaging can provide. When combining SAR and ICESat-2 images over sea ice, one must keep in mind the drift of sea ice occurring between the different acquisitions. In the Baltic (during ice season 2018-2019), at least 4 buoys were stationed to measure the drift of the ice with hourly intervals (Karvonen, 2020). Furthermore, a daily ice drift product of the Baltic based on SAR imaging is available at Copernicus Marine Environment Monitoring Service (CMEMS) based on the work of Karvonen (2012). Thus, the Baltic Sea proves an interesting area to investigate the combination of SAR imaging and ICESat-2 for smaller-scale roughness features in sea ice such as pressure ridges.

We assume that ridging features such as sail heights should be possible to distinguish in the data as long as noise reduction is taken into account (based on study by Farrell et al. (2015)). There is a fine balance between filtering and reducing the signal just enough to reduce the noise, but to keep the important and relevant information. We would like to, when the first results from Duncan and Farrell (2019) are published, see just how well the individual ridges can be detected and to what extent they can be detected, e.g. whether only higher than 0.5 m sails or if smaller scales be detected. This is an interesting aspect, since the studies of Duncan and Farrell (2019) are based on Arctic pressure ridges which in general are higher than Baltic ridges (e.g. Duncan et al., 2018; Rabenstein et al., 2009). Since their study is also validated by ATM lidar measurements, it provides a good background for whether or not ridge sails can be detected in the Baltic by using their method. In Sect. 8 one can find considerations and thoughts for future work when estimating ridges from ATL03 and explanations on why we were not successful in determining individual ridges during this study.

Q3 To what extent coastal bathymetry in the Baltic archipelago can be derived from ICESat-2 data?

For all of our four sites (Kattegat, The Sound, Archipelago Sea and The Bay of Bothnia) it was possible to retrieve bathymetric measurements from ICESat-2. Measurements were acquired either in late winter/spring or late summer. We were able to extract maximum depths ranging from 4 m (Bay of Bothnia, near Oulu) down to 16 m (the Sound), with an average maximum depth of 8.58 m. In Kattegat near Anholt even specific bathymetric features were able to be distinguished from the noisy photons showing that ICESat-2 is even able to retrieve submerged features should under right conditions.

We have compared some of the photon measurements with manually selected depth profiles from BSBD which showed a great consistency and correlation with ICESat-2 bathymetric seafloor detections. This is positive in the sense, that in the right conditions nearshore

bathymetric measurements can profile high-resolution values where none may have been available before. It is also negative, since ICESat-2 data is public, so everyone can get a hold of the data and try to retrieve bathymetry over regions which may be otherwise restricted or confidential information. Not all tracks could be compared to depth profiles due to restrictions on the available bathymetric data.

To know to which extent coastal bathymetry in the Baltic could be derived from ICESat-2 as a function of water clarity, we compared with Secchi depth data from HELCOM ICES (acquired during 1975-2018). We partitioned the Secchi depths into monthly values and compared the maximum observed ICESat-2 depth with average Secchi depth pr. month and maximum Secchi depth pr. month. Maximum penetration in Secchi depth based on monthly mean was on average 1.41 for the four sites, suggesting that the dates we retrieved from ICESat-2 bathymetry has favourable conditions and clearer waters than on average. The maximum penetration in Secchi depth with monthly maximum values was on average 0.87 for the four sites, suggesting that ICESat-2 is able to retrieve bathymetric measurements almost to the complete length of the deepest Secchi depth observed during those years. Hence, ICESat-2 is able to retrieve bathymetry measurements as long as the water is clear enough for this, even if the waters are murkier and more affected by eutrophication than at the sites used in Parrish et al. (2019), who achieved a maximum penetration of 0.96 with depths down to $\sim$40 m.

Lastly, a comment should be made on the important need for refraction corrections in bathymetric measurements. As has been mentioned several times throughout the dissertation, we have not applied the corrections caused by the photons interaction with air-water interface and the change of speed that occurs when travelling in water. We will once more highlight that this is an necessary step to retrieve truth (or reliable) bathymetric measurements from ICESat-2. In Sect. 8, we explain the needs in further detail and introduce a possible value of uncertainty in the bathymetric measurements retrieved in this study based on analysis and results from Parrish et al. (2019).

An important factor, also briefly mentioned in the study of Parrish et al. (2019), is the seafloor reflectance as a function of the laser wavelength of 532 nm and seafloor type. They mentioned that with their four sites being mostly sandy substrates with some coral and limestone, it could be considered ideal for maximum depth mapping by LIDAR. We have not thoroughly investigated the seafloor type and the effect on the bathymetric measurements, but we would like to briefly mention where and how it can be affected. A study by Pe'eri et al. (2011), based on Airborne LIDAR Bathymetry (ALB), have investigated the ability to detect the sea-bottom based on the seafloor type. They concluded that there was a strong correlation between sandy bottoms and strong bottom detection in ALB seafloor measurements. Furthermore, they concluded that there was a strong correlation between lack of ALB measurements over rocky bottoms and vegetated bottoms (regardless of bottom composition).

Sediment substrates for the Baltic and Danish waters is shown in Fig. 7.1. It is evident here, that values from Kattegat, The Sound and the Bothnian Bay (near Oulu) should be able to receive the strongest bottom detections, since the substrate sediments here are mostly sand, mud to muddy sand, coarse substrate or mixed substrate. The Swedish side of the Bothnian Bay (near Luleå) is mostly mud to muddy sand or mixed sediment with small amount of sand as sediment substrate, so there can be a lack of received bottom detections

in correlation with the seafloor type. The Archipelago Sea has almost no evident sand as substrate type, but is largely covered by mixed sediment alongside rock and boulders. This indicates that there can be a lack of sea-bottom detections from here as well. This is due to the laser pulse interacting with steep-sloped rocky areas causing multiple interactions to occur with several reflections occurring in the rocky environment, thus the energy reflected back to the detector is significantly lower than from e.g. sandy bottoms, where the reflection is occurring as a single interaction (Pe'eri et al., 2011). We do not have further information on distribution of vegetation of the sea bottom, but can simply suggest that this will also lead to lack of seafloor detections as has been concluded by Pe'eri et al. (2011). Furthermore, we would also like to highlight a conclusion from Parrish et al. (2019) in relation to data gaps in the photon data. They believe, after analysing their data from an area with a large data gap, that darker substrates, i.e. less reflective at 532 nm, and nearshore effects such as e.g. bubbles, foam, breaking waves and/or suspended sediment, can lead to data gaps in the surface measurements as well.

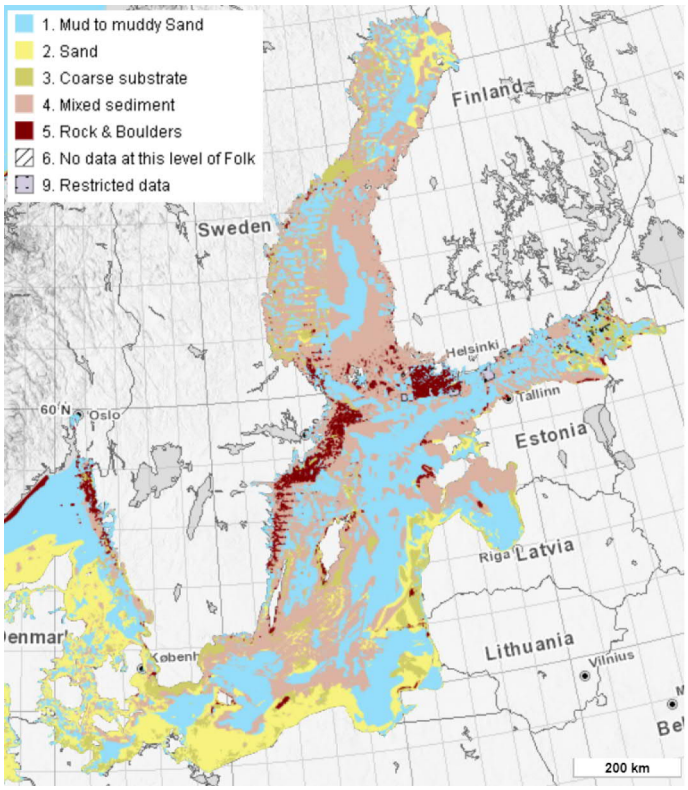

Figure 7.1: Sediment substrates in the Baltic and Danish Waters (The Sound and Kattegat included), courtesy of EMODnet Geology (available at https://www.emodnet-geology.eu/map-viewer/?p=seabed_substrate, *Multiscale - folk 5 (1:50k Seabed Substrate Map) as part of EMODnet-Geology III project. The EMODnet-Geology III project started in 2017 with 39 marine departments of the geological surveys of Europe (from 30 countries), with an objective to assemble marine geological information from all European sea areas*).

The vegetation at sea bottom and change in sediments having an impact on the capability of retrieving bathymetric measurements from ICESat-2 is where the eutrophication status in the Baltic plays an important role. Not only does eutrophication affect the turbidity of the waters, but it can also allow oxygen deprived organic material to sink to the bottom (Furman et al., 2013). As was previously concluded by Pe'eri et al. (2011), vegetation on the sea bottom can result in a lack of seafloor detection and different seafloor substrates

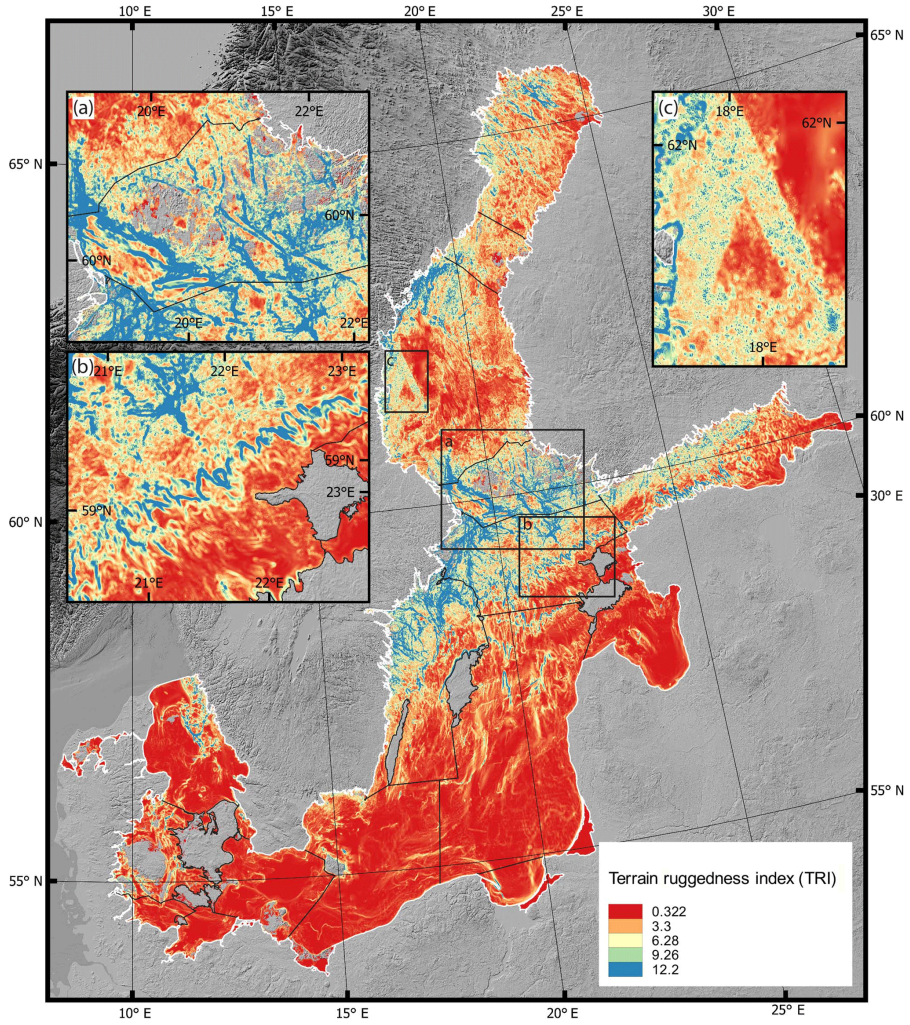

Figure 7.2: Calculated Terrain Ruggedness Index (TRI) of the Baltic seafloor, courtesy of Jakobsson et al. (2019). Areas highlighted are explained further in the study of Jakobsson et al. (2019).

respond differently to the laser pulse, causing the reflected signal to be scattered several times and less clear in the received signal. Thus, it would be interesting to see if ICESat-2 is even able to achieve nearshore bathymetric measurements in areas more affected by eutrophication (such as the coastlines of the Baltic Proper, see Fig. 2.7), compared to the areas we have investigated, that are either neutral in the aspect of not being or being affected by eutrophication or being almost unaffected by eutrophication.

With regards to a rocky sea-bottom causing increased scattering of the signal with a possible lack of bottom detections, we have looked into the Terrain Ruggedness Index (TRI) of the Baltic (see Fig. 7.2). TRI is a measure of the ruggedness of the surface. Hence, this may also indicate why seafloor detections are sparse in some regions, because of the scattering that may occur in the largely rugged (i.e. rough) seafloor. Thus, the signal would be scattered several times and only limited amount of signal will return to the observatory (i.e. fewer photons will be detected). Based on Fig. 7.2, the loss of seafloor detections because of rugged seafloors, are highest in the northeastern Kattegat, the western Gotland Basin, the northwestern Baltic Proper, the entire Åland Sea and Archipelago Sea, some of the Gulf of Finland, the northeastern Bothnian Sea and the northwestern Bay of Bothnia.

For us, this may suggest that bathymetry in the Archipelago Sea and the Bay of Bothnia could be affected by the ruggedness. For the Archipelago Sea and the Bay of Bothnia, the bathymetric measurements were sparse and mainly retrieved over inland waters. Open sea area did barely contain any bathymetric measurements. Whether this was caused by water turbidity, the seafloor depth being lower than what the water clarity (hence, penetration of photons) allows for, seafloor sediment and seafloor type or rugged seafloor is not known, but all are factors that affects the return of the signal.

8 Considerations for future work with ICESat-2

The results presented in this dissertation is based on months of assessment of the ICESat-2 photon clouds. The findings presented here successfully demonstrate the potential of using ICESat-2 to extract on pressure ridges and shallow water bathymetry and provide researchers in the field with knowledge on how to handle the photon cloud, including limitations and challenges by using these data. In the following Sections we will present some ideas and considerations which should be carefully assessed in future work related to shallow water bathymetry, sea ice pressure ridges, and sea ice thickness, in the Baltic. Comments on the prospect of using these measurements for ice navigation in the Arctic is also provided, where we draw a parallel to the effect on Arctic sea ice caused by climate change.

8.1 Sea ice pressure ridges and thickness

For future work, if one would like to investigate ridge sail heights or ridge density, we recommend to generate an algorithm that can automatically discriminate between surface and background photon returns to ensure further filtration of cloud or background sun event returns and to apply a spatial filter to reduce noise and smooth the surface response. Then, with a smoothed surface response, one could apply a local maxima filter with a Rayleigh criterion incorporated which ensure that two adjacent ridges can be separated to detect independent ridges in the data and use this to investigate the density and sail heights. The coarse discrimination and smoothing can use suggestions based on findings by Farrell et al. (2015). Here, they apply the MABEL surface-finding algorithm described by Brunt et al. (2014). This allows for a coarse discrimination between signal (surface) photons and background photons to reduce the photon cloud, much similar to what has already been applied by the high-signal confidence pre-processing step in this study (Sect. 5.1.2). Furthermore, an along-track maximum likelihood probability filter (of 10 m) was applied to reduce the noise and smooth the surface response to the MABEL data by Farrell et al. (2015). We propose a similar approach in order to prepare the data before applying the local maxima algorithm to detect pressure ridges. Furthermore, one would need to estimate the Local Sea Surface (LSS) to estimate reliable ridge sail heights (see Fig. 8.1 for a schematic diagram of pressure ridges). In Farrell et al. (2015) they estimated the LSS by using DMS visible imagery from same transect as both ATM airborne laser altimeter and MABEL measurements and found the LSS by a decrease in pixel brightness (leads being darker with open water/very thin ice). This approach by use of DMS visible images is not applicable for ICESat-2, as there are no coincident images and other methods needs to be investigated and applied.

To estimate LSS one needs a measure of the water level. It is common to use elevation heights from leads, open-water areas in ice-covered regions, as estimate for the LSS. In conventional altimetry, one uses parameters derived from the waveform, i.e. the shape of the return signal, since leads has a very characteristics shape (narrow and high peak, steep slope on trailing edge of the waveform). The parameters, such as maximum value or pulse

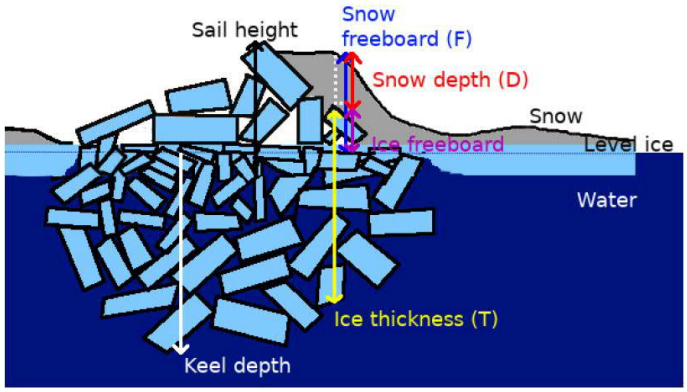

Figure 8.1: Schematic diagram of a typical ridge, courtesy of (Mei et al., 2019). The ridge may not be symmetric, and peaks of the sail and keel may not coincide.

peakiness of the waveform, are usually significantly higher for leads and open water compared to sea ice, so it is is possible to distinguish between the different surface types and use these lead values as a reference of LSS (e.g. Wernecke and Kaleschke, 2015). Waveform parameters are not possible to extract from ICESat-2 as the data product is a photon cloud of the surface, so another measure to estimate leads is necessary. Other methods of estimating the LSS in laser altimetry, has been by applying a lowest-level filtration to the data (e.g. Kwok et al., 2007; Skourup, 2010; Zwally et al., 2008), assuming the lowest measurements are from sea levels as was the case of ICESat carrying a NIR laser. This assumption fails for ICESat-2, as the green laser allows for penetration into water bodies. In Level-3A Arctic/Antarctic Sea Ice Elevation (ATL07) data, they make use of a coarse and fine discrimination of the surface type to estimate whether the measurements are from e.g. sea ice or open water/thin ice (leads). They aggregate the photons into segments of 150 (can be changed, but currently allows for vertical accuracy better than 3 cm (Brunt et al., 2019)) and uses the background photon rate, photon rate per laser pulse and width of the photon distribution to estimate the surface height (the fine discrimination) (Kwok et al., 2019a). The photon rate is used to estimate leads, as both dark water leads (with a low photon rate) and the specular or quasi-specular returns that are usually seen in very narrow leads (with a high photon rate) are seen in the data (Kwok et al., 2019b). The combination of photon rate and background rate provides the ability to detect both large, dark water leads and narrow, maybe even thin ice-covered narrow leads. However, the leads detected in ATL07 over the Baltic Sea are currently flagged as having bad signal confidence in the overpasses that we investigated. Furthermore, several of the days we investigated did not have leads to use as a reference for LSS. So even with an interpolation of a simulated LSS based on a linear fit between the identified leads, it was still not straightforward for specific tracks. In case of a sparse distribution of leads, e.g. only leads in the first part of the first region of the track, the regions later on will be introduced to a bias from the LSS linear trend, either causing it to become more positive or negative depending on amount of measured leads and the trend between these. Thus, the algorithm suggested by (Kwok et al., 2019a) does not always apply to the Baltic region where surface measurements are not necessarily available at high confidence, and thus alternative methods are needed.

Nonetheless, the data products ATL07 (Sea Ice Heights) and especially ATL10 (Sea Ice

Freeboard) over the Baltic Sea should be investigated further. ATL07 are only calculated over local sea ice concentration >15 % according to the MASIE product, and has as previously mentioned a vertical height precision of ∼2 m over relatively flat surfaces (Kwok et al., 2019b). We highlight that this specific type of single-pulse photon-counting laser altimeter that ICESat-2 is, is affected by an effect called the first-photon bias (Neumann et al., 2019b). First-photon bias is dependent on the strength of the signal and primarily related to photon-counting devices. To briefly explain it, an individual detector has a brief period of time after it has measured a photon (known as the dead time) before the detector can measure a new photon. This means, that with only 16 (strong beams) and 4 (weak beams) detectors, the photons arriving from the reflected surface first will most likely be detected first, thus introduction an upward bias (Kwok et al., 2019b). This effect is largest over strong returns such as e.g. specular and quasi-specular returns. A correction should be applied which is available in the ATL07 product.

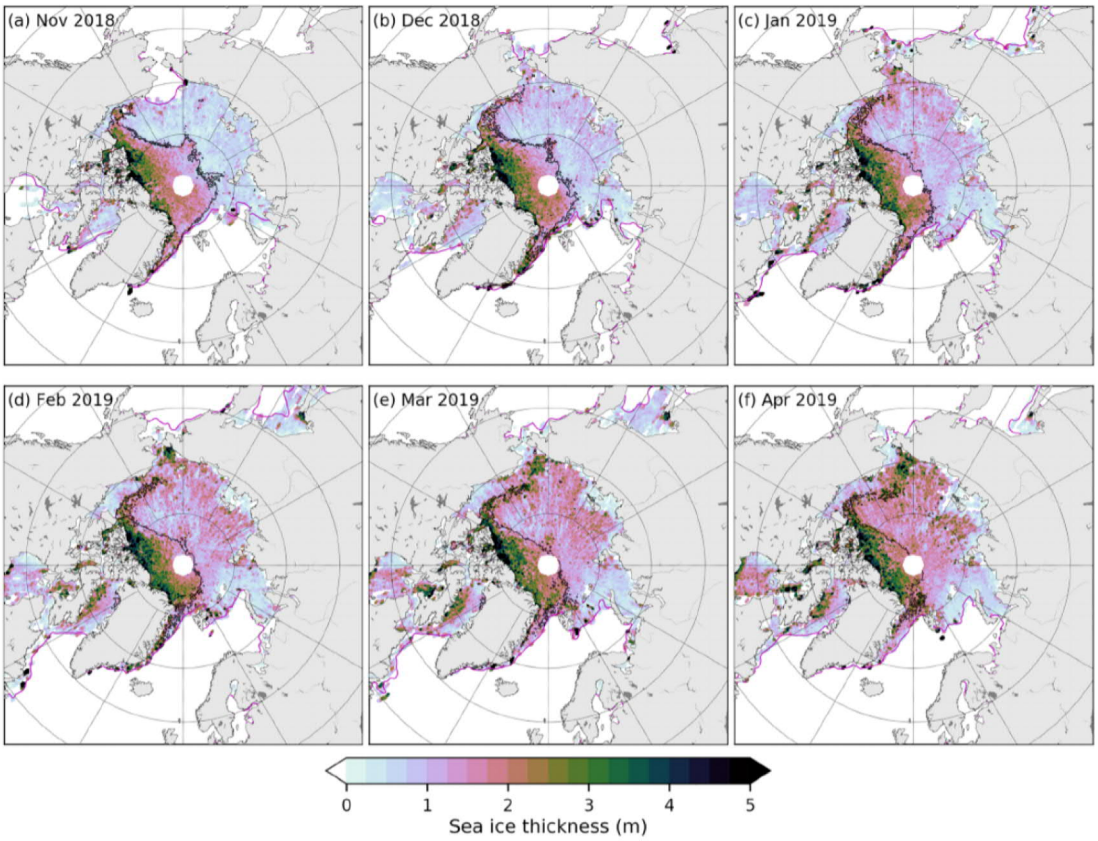

Figure 8.2: Gridded sea ice thickness from ICESat-2 (monthly average of November 2018 to April 2019) with NEOSIM piece-wise redistributed snow depth (NS_{rd-pw}), courtesy of Petty et al. (2020). Magenta line shows the 50 % ice concentration contour from NASA's Climate Data Record passive microwave data set. Black line shows the FY/MY ice boundary from OSI SAF ice type product.

Finally, we would also like to highlight the ATL10 data product. While probably being one of the most interesting features as it provides sea ice freeboard values that can be converted into sea ice thickness by assuming hydrostatic equilibrium, the possibility of doing that in the Baltic is currently very limited. ATL10 is currently only being calculated in regions where the ice concentration is >50 %, within a 10 km segment of a lead and has to be more than 50 km away from the nearest shore/coast-line. While the requirement for

ice concentration is not an issue in the Bothnian Bay, the requirement of height samples being at least 50 km from the coast can prove a bigger obstacles, as the Bay of Bothnian has a length of about 300 km and a width of 100-150 km. The data product would need to be studied further in the Bay of Bothnia - especially since the lead values extracted from ATL07 show low signal confidence. Based on this, we chose not to investigate the possible ATL10 freeboard heights in further detail.

It is however, still a data product that should be investigated, especially when future releases hopefully provides information on sea ice in coastal zones and with smaller ice concentrations, as it could provide high-spatial information of sea ice in the Baltic Sea. When estimating the sea ice thickness from freeboard measurements from ICESat-2 one assumes the entire freeboard to be with both sea ice and snow cover in laser altimetry which is a valid assumption for e.g. NIR lasers. However, it should be mentioned that snow cover on the ice can scatter the laser which will affect the result of the freeboard observations (Kwok et al., 2019a). Thus, additional snow cover and depth information is needed to redeem reliable sea ice thickness results. The first results of sea ice thickness in the Arctic from ICESat-2 (see Fig. 8.2) has recently been published (Petty et al., 2020). In their comparison with CryoSat-2 (carrying a SAR radar altimeter), the estimated ICESat-2 measurements are thinner than CryoSat-2 which they attribute to most likely be a systematic bias, but claims that it needs to be studied further. They also mentions that errors in assumed snow depth can introduce the difference in the thickness due to different methods of computing the thickness from laser and radar altimetry.Thus, even though there are also limited data coverage (25 granules with useful data during January-March 2019 in the Bay of Bothnia based on ATL03 data product, see Table 4.3) and the ATL10 is not yet fully developed for coastal sea ice thickness, it is worth looking into the possibilities of estimating sea ice thickness in the Baltic. And, it becomes even more relevant when the ATL10 product allows for coastal freeboard measurements.

8.2 Detection and investigation of bathymetry in the Baltic

As mentioned in the Sect. 5.2, there is a need for refraction corrections to be applied to the measurements from ICESat-2. The geolocation process of photons from ICESat-2 does not take into account the refraction that occurs at the air-water interface nor the change in speed of light after entering the water column (Parrish et al., 2019). These effects produces both vertical and horizontal errors, causing the bathymetric measurements to be deeper and more off-nadir than they actually are. To account for the refraction and change in speed in the water column, there are five steps that needs to be taken according to Parrish et al. (2019): (1) either manually (current method) or automatically (needs work to estimate this algorithm) select af a subset the geolocated seafloor photon returns; (2) estimate a water surface reference from the water surface photon returns; (3) provide estimates of the refractive indices of air and water; (4) provide the angle of incidence for each photons by using relevant parameters available in the ATL03 product; and (5) provide the azimuth of the unit pointing vector provided by the ATL03 algorithm. The refraction corrections have not been applied in this study mainly due to two things; it is a tedious and time-consuming process to manually extract bathymetric measurements and the corresponding water surface reference from available surface photons. Furthermore, the idea of this dissertation was a proof-of-concept of shallow water bathymetry in murky waters. Thus,

we have confined ourselves to describe the capabilities of ICESat-2 with few bathymetric examples and a description of the future work needed for reliable estimation of shallow water bathymetry obtained with the smallest error as possible. The need for refraction corrections is explained as a *z-error* correction by Parrish et al. (2019), where *z*-axis is the vertical direction parallel to and opposite of the direction of gravity.

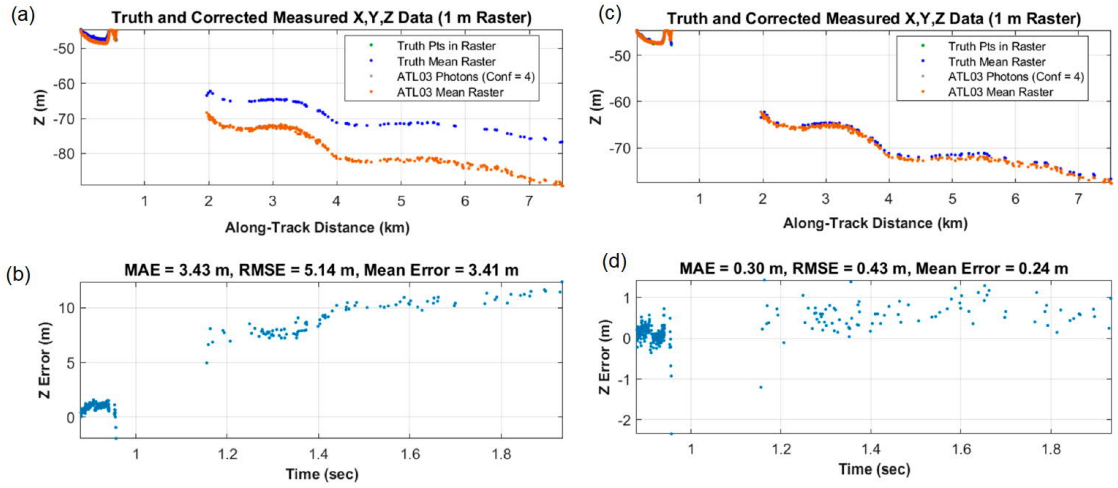

Figure 8.3: Elevation differences between Experimental Advanced Airborne Research Lidar-B (EAARL-B) topographic-bathymetric lidar data (used as the 'truth') and ATLAS bathymetry at 1 m grid resolution, courtesy of Parrish et al. (2019). (a) truth and ATL03 seafloor bottom measurements without refraction correction, (b) *z-error* for ATL03 photons without refraction correction, (c) truth and ATL03 seafloor bottom measurements with refraction corrections and (d) *z-error* for ATL03 with refraction corrections. RMSE is the root mean square error and MAE is the mean absolute error.

From their measurements over a full ∼6 km track of sea floor bottom measurements they have estimated the impact of the *z-error* in bathymetric measurements (see Fig. 8.3), where they measured a maximum depth of 38 m (with refraction corrections applied). What is shown is that the *z-error* increases with increasing depth. At depths of ∼35 km (along-track 4 km, Fig. 8.3a), the *z-error* is ∼10 m and overall over this transect, the Root Mean Square Error (RMSE) is 5.14 m (Fig. 8.3b). Here you can also see that depths between 0 m to ∼20 m ranges from 0-5 m in *z-error*. After applying the corrections, the photons are almost completely on top of the 'true' values in Fig. 8.3c, i.e. the *z-error* ranges between -1 m to 1 m (but is mostly around 0.5 m, see Fig. 8.3d) with a RMSE of 0.43 m. Thus, it is a necessary and important correction that almost reduced errors in depth caused by the air-water interface and change in speed of light. Since our depths are ranging from 0-16 m, we can expect there to be a *z-error* in the order of maximum 5 m, but since most of our measurements are within 0-10 m, we should not expect more than 0-2 m corrections in *z-order* according to their measurements. These measurements are however also affected by the turbidity of the water and thus, it can be different values of correction in the Baltic Sea, but it is a reasonable estimate of uncertainty.

Parrish et al. (2019) also noted how performance enhancements to this method should be investigated. They specifically mention automating the manual process of extracting the bathymetric detections, possibly by leveraging the recent work done on detecting weak echoes in photon-counting LIDAR's (Wang et al., 2018) and a variation of the Random Sample Consensus (RANSAC) algorithm (Parrish et al., 2019). We have also discussed

a method to automatically detect bathymetric measurements based on the density of photons as the water surface has the highest density and the bathymetric measurements often having slightly higher densities than background sun or scattering events. Thus, using the highest densities in a vertical column for the water surface reference and second higher density as bathymetric measurements could be an approach to automate the extraction process. This assumption has shown to be true to some extent, however the deeper the bathymetry, the less bathymetric measurements. At some point, even though a human can interpret the graphs to follow the bathymetry measurements well enough, an algorithm based on density may not be feasible anymore. It would mean that the shallow water bathymetry measurements detected by an automatic, density-based algorithm would underestimate the actual depth that ATLAS would be able to measure. Furthermore, the problem of after-pulses will prove a complication here.

As seen in Fig. 6.8 and to some extent in Fig. 6.11, after-pulses are present in the graphs. The after-pulses, as also mentioned before, have been studied and were found to most likely be a product of small after-pulses from either the ATLAS transmitted pulse or electronic noise following the arrival of the primary surface return, also known as *ringing* (see the online Known Issues document online, https://nsidc.org/sites/nsidc.org/files/technical-references/ICESat2_ATL03_Known_Issues_v002.pdf). Multiple returns like these are often seen over smooth open water surfaces. Thus, if one were to make a density-based algorithm, it would be required to somehow remove the dense distributed after-pulses to properly extract the correct bathymetric measurements. This leads us to an additional study that needs to be done. In our study of sea ice, since we only wanted to look into surface returns, we used the *signal confidence parameter* provided in the ATL03 product. For bathymetric measurements, we did not use the signal confidence parameter, as we wanted *all* the measurements available, in case the coarse surface discrimination algorithm did not identify bathymetric measurements as surface returns, which is likely if the measurements are sparse. As a result of this, not only low, medium or high signal confidence measurements were shown, but also background (*buffer*), noise, and possible Transmitter Echo Path (TEP) photons. It would be necessary to look into the *signal confidence* parameter or another measure of confidence to see whether these can still be used to remove noise, background and TEP photons while still preserving the bathymetric measurements. It is noteworthy that Parrish et al. (2019) got bathymetric measurements using only *high confidence* (confidence = 4) values (see Fig. 8.3), whereas we saw very limited bathymetric measurements when applying this restriction.

Lastly, it would be interesting to make an assessment of when bathymetric measurements would be available in the Baltic. As can now be concluded, the availability of bathymetric measurements from ICESat-2 in the Baltic is a function of water turbidity and cloud cover. Water turbidity is affected by e.g. CDOM or phytoplankton. An interesting study would be to see, when there would most likely be ICESat-2 data available based on measures of water clarity other than Secchi depths. One could for example look into water turbidity data from Finnish Environment Institute (SYKE) (they utilise Sentinel-2 employing a multi-spectral imager) to estimate the ability of retrieving ICESat-2 bathymetric measurements based on water clarity. Alternatively, one could look into chlorophyll-a measurements (see Fig. 8.4), a measurement that shows the amount of phytoplankton in upper waters, from e.g. Aqua or Terra (different satellites both employing the Moderate Resolution Imaging Spectroradiometer (MODIS) instrument), by the change of colour in

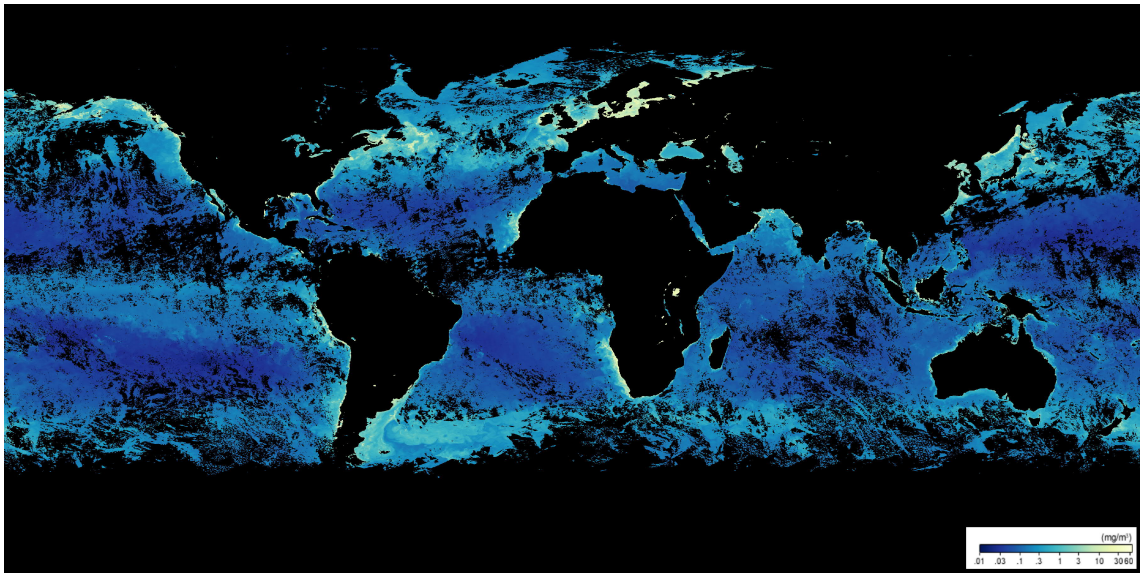

Figure 8.4: One month of chlorophyll-a data from Moderate Resolution Imaging Spectroradiometer (MODIS)/Aqua. Courtesy of NASA Earth Observation (available at https://neo.sci.gsfc.nasa.gov/view.php?datasetId=MY1DMM_CHLORA).

shallow waters. During this study, we worked with the assumption that shallow waters were clearest during late spring or fall/early winter (in ice-covered regions), as the algae bloom is expected to be worse during the summer (Seppänen, 2020). For Kattegat and The Sound, the clearest waters are generally during winter (Hermanni, 2020), based on Secchi depths, however this is not entirely in relation with the Secchi depths investigated in this study. We also chose data during spring for Kattegat and The Sound as clear bathymetric measurements were available here. Nonetheless, if one wants to automate the method estimating shallow water bathymetry from ICESat-2, it would be valuable to know if there are values above specific thresholds for e.g. water turbidity or chlorophyll-a where no bathymetric measurements can be retrieved from ICESat-2 and use this additional data in the process when automatically determining bathymetry from ICESat-2.

8.3 Restrictions on data acquired during ice season 2018-2019

We would like to briefly mention a few restrictions we encountered during the work of this dissertation. Firstly, even though ATL03 does not have a *cloud flag* useful for providing information on whether or not the measurements were affected by clouds, some of the higher level data products have that (e.g. ATL07). We initially had the idea to utilise this *cloud flag* for pre-processing of photons to exclude measurements disturbed by clouds. However, it was clear from the beginning that the *cloud flag* was not available due to calibration of ICESat-2. After the availability of new versions and identification of this error, it seems to no longer be an issue. Thus, it could also be interesting to see if the *cloud flag* or *apparent surface reflection flag* could be used in future pre-processing steps.

We would like to highlight some information about the .kml-files that provides the RGT orbit tracks. The ICESat-2 team have stated that prior to 1 April 2019, ICESat-2 was not pointing directly at the RGT's. Thus, one should not attempt to sync data with the .kml-files acquired between Oct 2018 and April 2019. We have used the .kml-files as an

approximate measure of where the ICESat-2 track would be during the ice season, but when e.g. choosing photons based on DIR polygons we have of course utilised the exact latitude and longitude measurements provided in ATL03 data set and not by .kml-files. Measurements after 1 April 2019 are now pointing towards the RGT's.

Finally, we want to mention that this thesis is based on Version 002 ICESat-2 measurements, and only on Version 001 if Version 002 were not available. By mid-May 2020 Version 003 became available. ATL03 Version 003 includes further pre-processing and filtration by thresholds related to the reference DEM used and parameter values on how fully saturated the photon cloud is within a given segment. It can prove useful when pre-processing the photons and should be considered, e.g. in terms of cloud disturbed segments. One can find information of the exact updates for the current Version by opening the *Version Summary* tab on the related data product site (e.g. https://nsidc.org/data/ATL03/versions/3).

8.4 Ocean and wave modelling

Another thing that could also be interesting to look at, both in the Baltic Sea, but also generally in ice-covered regions, is the ice-ocean interaction and modelling of ocean waves. The first studies in retrieving high-resolution ocean wave and wind characteristics from ICESat-2 has already been published. Klotz et al. (2019) uses a modified version of ICESat-2 Land Surface algorithm (ATL08) to map individual waves along the ICESat-2 track, and by this allows for retrieval of relevant parameters such as significant wave heights and wind speed. Thus, they show that ICESat-2 can be used to provide detailed regional and localised ocean observations to improve the understanding of air-sea and ocean-sea ice interaction. Already Parrish et al. (2019) pointed out the possibility to look into ocean waves, as from their photon product (though it focused on near shore bathymetry), they highlighted ocean waves which were higher than calmer ocean surfaces closer to the coast, see Fig. 8.5.

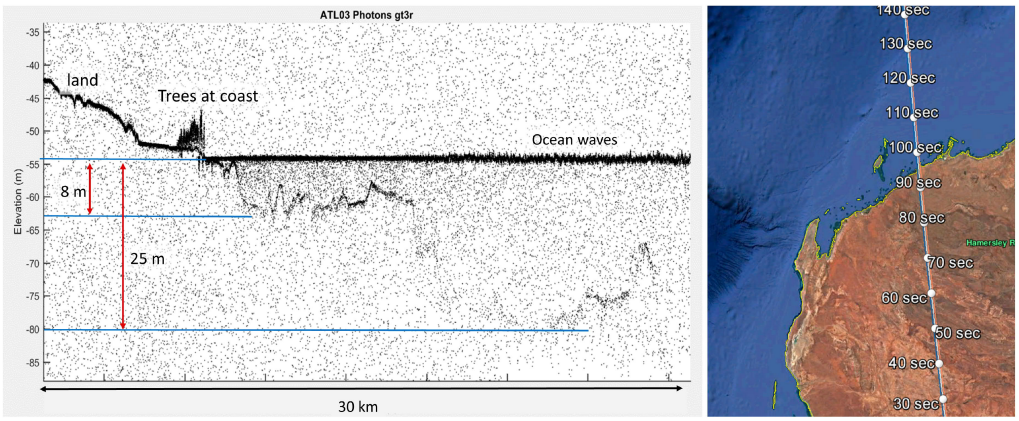

Figure 8.5: Geolocated bottom return photons for the North West Australia (western Pilbara region), courtesy of Parrish et al. (2019). Note, on the right side of the photons, the variation at the water surface related to ocean waves.

Specifically for the Baltic it would be interesting to investigate the ocean-wave possibilities, as there are currently 11 locations with buoys measuring the waves in the Baltic which can be used as reference data. As waves contributes to the mixing of surface layers and

is a huge source of information on the ocean environment in the Baltic (Pettersson et al., 2019), it would be interesting to investigate to what extent ocean waves characteristics and information can be retrieved from ICESat-2 and possibly use this to work with ice-ocean interactions as well.

8.5 MTA ARANDA COMBINE1 ice trials

The MTA ARANDA COMBINE1 ice trial was one of the ice breakers winter-monitoring missions of 2020 in the Baltic. COMBINE1 was based on HELCOM's monitoring programs which includes hydrographic and chemical measurements and analysis of waters alongside measurements of surface waters and sediments (to be measured and extracted in the Northern Gulf of Bothnia and Gulf of Finland). In addition, ice classification tests and ice-tests were to be extracted if possible since research in ice parameters and micro-plastic in ice and in water under ice was of interest. The classification tests were to be executed in the Bay of Bothnia. COMBINE1 took place from the 27/01-2020 to the 08/02-2020, with a total duration of 12 days, 3 hours and 7 min and had a total of 40 observation places to visit. On board COMBINE1 was a laser profiler that in combination with ICESat-2 tracks could provide valuable information on the precision and uncertainty of the photon observations, and possibly even higher-level products such as surface heights (ATL07). A ship radar and a Electro-Magnetic (EM) instrument to measure thickness was also carried on board. The ship route (with the name of stops) are shown in Fig. 8.6(a) and ICESat-2 tracks during the duration of COMBINE1 are shown in Fig. 8.6(b).

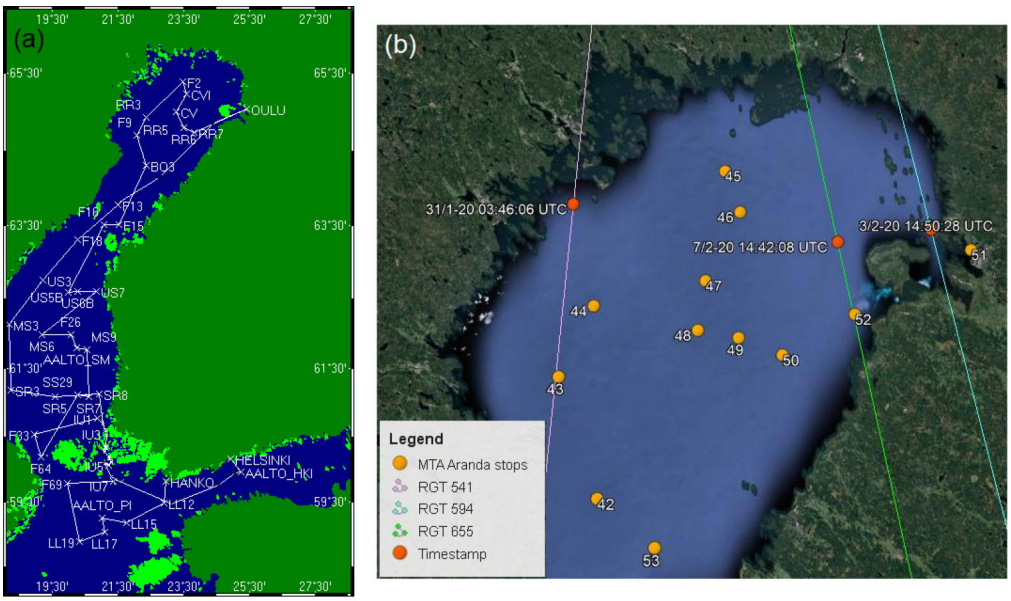

Figure 8.6: MTA ARANDA COMBINE1 route plan and ICESat-2 track near this route. (a) MTA ARANDA COMBINE1 route plan for the Baltic with stops given by abbreviation. (b) ICESat-2 overpasses of the Bay of Bothnia within period of 27/01-2020 to 08/02-2020 (using .kml-files provided by NASA, shown in Google Earth Pro). MTA ARANDA COMBINE1 stops in the Bothnian Bay are also highlighted.

One ICESat-2 track is close to the ship route, thus if the ICESat-2 track overpasses the laser profiler from the ship or the radar of the ship, it would be interesting to see what a combination of these measurements could provide. By mid-May the ICESat-2 ATL03 photon product over the Bothnian Bay has not yet become available, and thus we have not been able to include studies based on the cruise in this thesis. Whether this is due to

errors/delay of the specific data product or the issue with not pointing towards RGT's, as mentioned in Sect. 8.3, so that the track is in fact not over the Bothnian Bay, is not known by this point. It was however expected to have become available during this thesis work since the data latency for data product ATL03 is usually 21 days, with latency defined as approximate time from data acquisition on satellite until reaching users in a proper data format (Brown et al., 2016).

8.6 Climate change and shipping in the Arctic

A clear and rapid decline in sea ice extent in the Arctic has been observed by satellites since 1979 with loss of 2.4 mio km^2 Arctic sea ice from 1979-2019, see Fig. 8.7, likely caused by the warming of the Earth. Even over the past decades, the Arctic has warmed twice as fast as the rest of the globe, known as the Arctic Amplification. The accelerated loss of Arctic sea ice has lead to new openings of wintertime shipping routes in previously inaccessible areas. The melting and thinning of Arctic sea ice cause the ice cover to be dominated by younger, thinner ice than previously, which hampers the new ice production and thickening of the ice. In addition, shipping and pollution from active fleets will only accelerate the thinning of the Arctic ice cover, darken the ice cover surface and add to the warming and melting of ice caps (and subsequently, the rise of global sea level), since the albedo of the sea ice will decrease enhancing the positive ice-albedo feedback loop (Kedzierski and Dings, 2012).

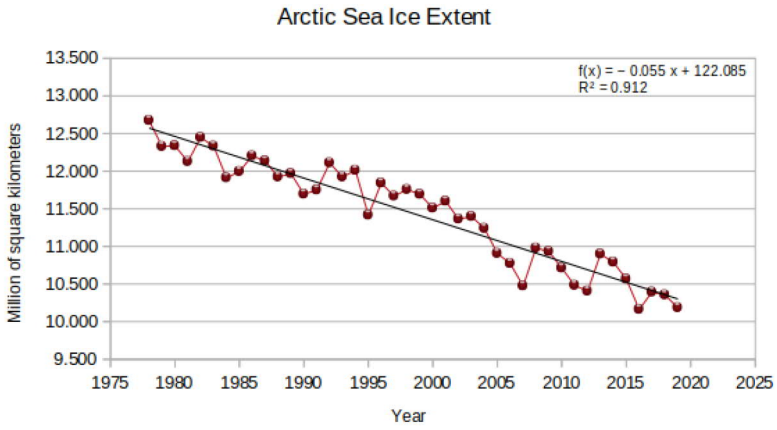

Figure 8.7: Annual Arctic sea ice extent (1979-2019) generated from available data from NSIDC (https://nsidc.org/arcticseaicenews/sea-ice-tools/).

With the melting of the ice caps and shrinking of the sea ice extent, the possibility of commercial shipping routes through the Arctic would significantly benefit the regional, EU and global economy. Hence, the first complete opening of the Northwest Passage in Summer (via Canada) happened in 2008, and the opening of the Northeast Passage by Summer crossings (via Russia; also known as the Northern Sea Route) the following year, see Fig. 8.8 (Kedzierski and Dings, 2012). While Summer crossings have been possible for quite some years, the first ship to make a winter crossing of the ice covered Arctic Ocean following the Northern Sea Route from Asia to Europe without ice-breaker support, was the cargo vessel "Eduard Toll" in February 2017 (Gabbatiss, 2018). It is estimated that by 2050, Arctic sea routes could attract around 10 % if the total container trade between Asia and Europe. Bennet (2019) even spoke of a Transpolar Arctic passage opening up, which allows for crossing directly through the North Pole, by 2050.

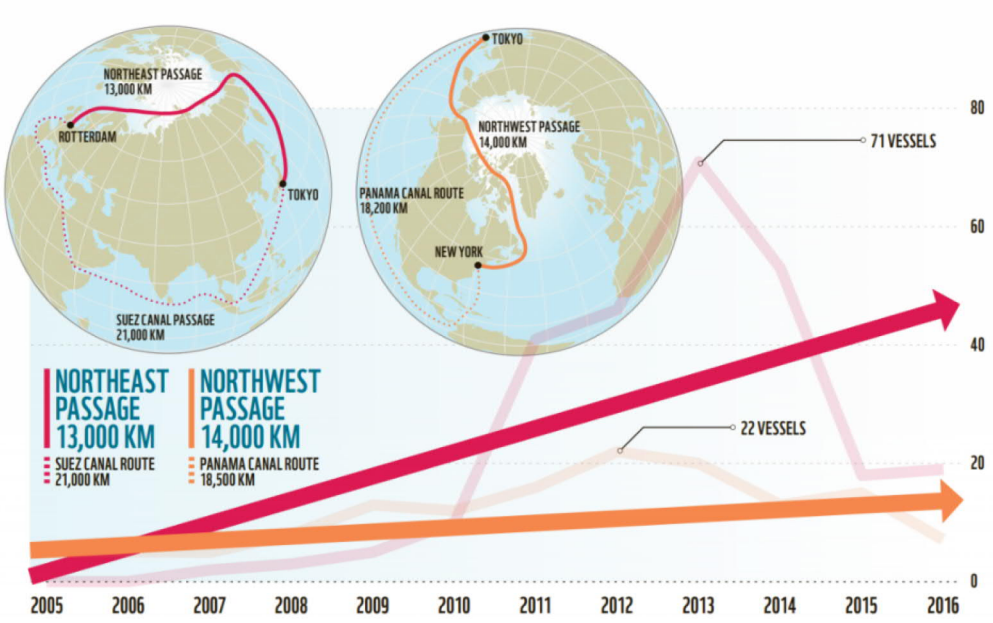

Figure 8.8: Activity of the Northeast (Northern Sea) and Northwest passage through the Arctic. Transparent line shows the yearly amount of vessels and filled line with arrow shows the trend (courtesy of WWF).

While several initiatives being taken (e.g. the Polar Code, a mandatory code for ships operating in polar waters) to ensure that the sensitive and unique ecosystem of the polar regions are kept, it is generally understood that an increase in polar shipping without any prerequisite measures taken to ensure the protection of the Arctic environment, means an acceleration of the sea ice extent and thickness (Kedzierski and Dings, 2012). And while new initiatives are under development to ensure as little harm as possible, it becomes clear that an increase in Arctic shipping is inevitable. Hence, navigation in ice-covered regions once more becomes a pressing issue especially with an increase in shipping. In particular wintertime shipping routes are hazardous and a potential danger to the pristine Arctic environment. Here we propose using ICESat-2 high-resolution surface measurements to investigate the surface roughness related to sea ice pressure ridges to aid navigation. As already mentioned, pressure ridges are some of the biggest hazards in ice-covered regions when a ship has to pass. While ice charting generally provides an idea of the ice conditions in the area, e.g. thickness, type and concentration, it is, to the best of our knowledge, only the FIS that provides ice charts with DIR information based on observation from an active icebreaker fleet (WMO, 2010). Furthermore, the results of our study in the Baltic shows that ICESat-2 can provide crucial information on surface roughness (even in smaller scales of ridging than in the Arctic) in terms of DIR. We propose, when considering the increase of wintertime shipping in the Arctic, that ice charting services around the world look into into utilising ICESat-2 to investigate the surface roughness related to pressure ridges that occurs in the Arctic, to produce ice charts that provides information on DIR.

9 Conclusion

The research aimed to assess ICESat-2 photon observations to support ice charting with a focus on distinguishing small-scale surface roughness features in the Baltic Sea such as pressure ridges, and to estimate shallow water bathymetry. ICESat-2 is the first Earth-orbiting photon counting laser altimeter and utilises a novel measurement strategy that allows for high-resolution surface elevations and across-track sampling, especially useful for estimating sea ice parameters. Space-borne altimeters is used to estimate sea ice thickness in inaccessible areas such as the Arctic and Antarctica, and provides, beside sea ice thickness measurements, global elevation measurements useful for estimating sea surface heights, gravity anomalies and bathymetry. With the increased spatial resolution, a multi-beam configuration and two different measurements strategies (nadir pointing for polar regions and off-nadir sampling for vegetated areas), ICESat-2 can provide unprecedented surface elevation measurements useful for a variety of scientific fields.

Pressure ridges and highly deformed sea ice is assumed a hazard for ships and prove as difficult obstacles to ship navigation in ice-covered regions. To aid navigation, ice charting services around the world provide ice charts during the ice season that informs on sea ice parameters such as thickness, type, extent and deformation. The Finnish Ice Services (FIS) provides daily ice charts with a deformation numeral on degree of ice ridging (DIR) based on ice breaker observations and SAR imaging. To estimate sea ice features, this thesis investigated the Bay of Bothnia with its extensive and deformed ice cover and presented the first results in using ICESat-2 measurements to estimate small-scale surface roughness features. The work presented here, proved successful in estimating DIR by a simple threshold-based discrimination of the relative photon elevations after applying pre-processing steps to filter away cloud disturbed photons and background sun events. The DIR zones estimated by ICESat-2 were compared with DIR polygons from FIS ice charts. DIR zones from ICESat-2 generally followed the DIR polygons from ice charts, however the photons allows for better spatial understanding of the surface (with footprints of 17 m and a pulse spacing of 0.7 m). By aggregating segments of 150 photons to produce relative elevations measurements containing information on the ridging occurring, which on average were separated by 17 m, it was possible to estimate deformation that followed the ice chart polygons. The elevation measurements showed greater deformation near landfast boundary and coastlines as expected.

We highlight, that the ice charts are used as the ground truth, but we acknowledge that the ice charts are subject to the ice analysts interpretation of data and may not be the actual ground truth. Thus, we emphasise the need for further validation of the ATL03 photons in estimating small-scale surface roughness. This could be done by comparing ICESat-2 measurements with e.g. Sentinel-1 SAR images or airborne laser surveys. Furthermore, we acknowledge that the method used in this study has weaknesses that requires more work. This includes additional filtration schemes to ensure that background sun events and cloud-disturbed photons are removed, to ensure a possible bias from those photons will not be introduced to the DIR estimation. To investigate individual ridges, noise reduction is a necessity. An impending study on sea ice pressure ridge detection in the Arctic from ICESat-2 photons could be used as inspiration in detecting ice ridges in the Baltic, should

their method prove able to measure ridge sails, i.e. ridge height above the water level, of 0.5 m as it is the average sail height in the Baltic.

It should be mentioned, that the sea ice freeboard, i.e. the ice above water surface, data product from ICESat-2 is currently not available in the Baltic and thus, have not been examined. When it becomes available in the Baltic, the distribution of sea ice thickness (converting freeboard observations to sea ice thickness by assuming hydrostatic equilibrium) should be investigated, since ICESat-2 provides measurements at high spatial resolution that would be interesting, not only for ice charting services, but also in relation to climate and science applications.

The second objective of this thesis was the possibility of estimating near shore bathymetry in shallow waters. Shallow water bathymetry is notoriously difficult to map, but is of interest to science and engineering applications and for navigation purposes as submerged features, such as rocks, can prove a hazard for ships. Bathymetry has been estimated previously echo sounders on ships, airborne lidar surveys, spaceborne radar altimetry or multi-spectral imagery. ICESat-2's green (532 nm) laser pulse allows for penetration into water bodies and is reflected at the seafloor, which makes it possible to obtain bathymetric measurements. Furthermore, ICESat-2 can overcome some of the limitations in measuring shallow water bathymetry that e.g. multi-spectral imagery is struggling with.

Former studies have already showed ICESat-2's ability to retrieve seafloor detections in shallow, clear waters near the US Virgin Islands and the Bahamas, but studies in murkier and eutrophicated waters such as the Baltic was yet to be done. This thesis presents the first successful results in estimating shallow water bathymetry in the Baltic and Danish waters down to depths of 16 m. Furthermore, investigating ICESat-2's capability of estimating shallow water bathymetry as a function of clarity showed, that ICESat-2 was able to measure up to 0.87 Secchi depth (based on monthly maximums), where Secchi depths are used as a proxy for water clarity. In addition, comparing with depth profiles from Baltic Sea Bathymetric Database (BSBD), specific submerged features were identified, which shows the possibility of utilising ICESat-2's high spatial resolution to map specific submerged features.

We emphasise that refraction corrections have not been applied to the retrieved bathymetric observations of shallow waters in the Baltic and is a requirement, should one use these observations in the future. We estimate the correction to be of 0-2 m in depths up to 10 m, and up to 5 m in depths up to 20 m. We also highlight, that future studies on seafloor reflectance as a function of sediment substrates and ruggedness of the terrain are encouraged.

Bibliography

Aas, E., Høkedal, J., and Sørensen, K. (2014). Secchi depth in the Oslofjord-Skagerrak area: theory, experiments and relationships to other quantities. *Ocean Science*, 10:177–199.

Abdalati, W., Zwally, J. H., Bindschadler, R., Csatho, B., Farrell, S. L., Fricker, H. A., Harding, D., Kwok, R., Lefsky, M., Markus, T., Marshak, A., Neumann, T., Palm, S., Schutz, B., Smith, B., Spinhirne, J., and Webb, C. (2010). The ICESat-2 Laser Altimetry Mission. *Proceedings of the IEEE*, 98(5):735–751.

Alikas, K. and Kratzer, S. (2017). Improved retrieval of Secchi depth for optically-complex waters using remote sensing data. *Ecological Indicators*, 77:218–277.

Armon, M., Dente, E., Shmilovitz, Y., Mushkin, A., Cohen, T. J., Morin, E., and Enzel, Y. (2020). Determining bathymetry of shallow and ephemeral desert lakes using satellite imagery and altimetry. *Geophysical Research Letters*, 47(e2020GL087367):9.

Attila, J. (2019). *Water quality monitoring and assessment of the Northern Baltic Sea using Earth Observation*. PhD thesis, Aalto University, Helsinki, Finland. ISSN: 9-7688-06-259-879.

Bennet, M. (2019). The Arctic Shipping Route No One's Talking About. The Maritime Executive (published 05 August 2019). Available at: https://www.maritime-executive.com/editorials/the-arctic-shipping-route-no-one-s-talking-about (Accessed 15 May 2020). News article.

Berglund, R. and Eriksson, P. B. (2015). *National ice service operations and products around the world*, chapter 5.2. H. Shen (Ed.) Cold Regions Science and Marine Technology. This chapter discusses "Ice Charts and – Formats".

BIM (2019). Baltic sea icebreaking report 2018-2019. Available at: http://baltice.org/about/ (Accessed 24 Jan 2020). BIM is the Baltic Icebreaking Management.

Bowditch, N. (2019). American Practical Navigator - An Epitome of Navigation. NSN: 7642014014652 (Also available at: https://msi.nga.mil/api/publications/download?key=16693975/SFH00000/Bowditch_Vol_1.pdf&type=view, accessed 24 Jan 2020), National Geospatial-Intelligence Agency, Virginia. 2019 edition, originally from 1802, pp. 753.

Brenner, A. C., DiMarzio, J. P., and Zwally, H. J. (2007). Precision and Accuracy of Satellite Radar and Laser Altimeter Data Over the Continental Ice Sheets. *IEEE Transactions on Geoscience and Remote Sensing*, 45(2):321–331.

Brown, M. E., Arias, S. D., Neumann, T., Jasinksi, M. F., Posey, P., Babonis, G., Glenn, N. F., Birkett, C. M., Escobar, V. M., and Markus, T. (2016). Applications for ICESat-2 data. *IEE Geoscience and Remote Sensing Magazine*, pages 24–37.

Brunt, K. M., Neumann, T. A., and Smith, B. E. (2019). Assessment of ICESat□2 ice

sheet surface heights, based on comparisons over the interior of the Antarctic ice sheet. *Geophysical Research Letters*, 46(22):13,072–13,078.

Brunt, K. M., Neumann, T. A., Walsh, K. M., and Markus, T. (2014). Determination of Local Slope on the Greenland Ice Sheet Using a Multibeam Photon-Counting Lidar in Preparation for the ICESat-2 Mission. *IEEE Geoscience and Remote Sensing Letters*, 11(5):935–939.

BSHC (2020a). Baltic sea bathymetry database. Available at: http://data.bshc.pro/about/ [Accessed 23 April 2020]. BSHC is the Baltic Sea Hydrographic Commission.

BSHC (2020b). Source data used for the BSBD compilation. Available at: http://data.bshc.pro/metadata/sources/ [Accessed 23 April 2020]. BSHC is the Baltic Sea Hydrographic Commission.

Duncan, K. and Farrell, S. (2019). Analysis of Arctic Sea Ice Pressure Ridges from ICESat-2. Available at: https://cisess.umd.edu/assets/1/7/5-2_Kyle_Duncan.pdf (Accessed 17 May 2020). Abstract for 2019 CISESS Science Meeting.

Duncan, K., Farrell, S., Connor, L., Richter-Menge, J., Hutchings, J., and Dominguez, R. (2018). High-resolution airborne observations of sea-ice pressure ridge sail height. *Annals of Glaciology*, 59(76pt2):137–147.

Dyrcz, C. (2017). Analysis of Ice Conditions in the Baltic Sea and in the Puck Bay. *Scientific Journal of Polish Naval Academy*, 3(210):13–31.

EEA (2019). Arctic and Baltic sea ice. Available at: https://www.eea.europa.eu/data-and-maps/indicators/arctic-sea-ice-3/assessment-1 (Accessed 24 Jan 2020). EEA is the European Environment Agency.

Eriksson, P., Karvonen, J., and Vainio, J. (2018). Sea ice charts and SAR for sea ice classification. The Finnish Meteorological Institute. Slides for ECMWF Ocean Workshop, 22-25 January. Available at: https://www.ecmwf.int/sites/default/files/elibrary/2018/17974-sea-ice-charts-and-sar-sea-ice-classification.pdf (Accessed 10 Jan 2020).

ESA (2020). ERS 1 and 2. Available at: https://www.esa.int/Applications/Observing_the_Earth/ERS_1_and_2 (Accessed 08 Jan 2020).

Fan, D., Li, S., Meng, S., Zhang, C., Feng, J., Huang, Y., Du, J., and Xing, Z. (2019). Bathymetric Prediction from Multi-source Satellite Altimetry Gravity Data. *Journal of Geodesy and Geoinformation Science*, 2(1):49–58.

Farrell, S., Markus, T., Kwok, R., and Connor, L. (2011). Laser altimetry sampling strategies over sea ice. *Annals of Glaciology*, 52(57):69–76.

Farrell, S. L., Brunt, K. M., Ruth, J. M., Kuhn, J. M., Connor, L. N., and Walsh, K. M. (2015). Sea-ice freeboard retrieval using digital photon-counting laser altimetry. *Annals of Glaciology*, 56(69):167–174.

Fleming-Lehtinen, V. (2016). *Secchi depth in the Baltic Sea - an indicator of eutrophication*. PhD thesis, University of Helsinki, Faculty of Biological and Environmental Sciences, Helsinki. 42 pp.

Fleming-Lehtinen, V., Kaitaranta, J., and Hoikkala, L. (2020). Water clarity HELCOM core indicator report 2018. Available at: https://www.helcom.fi/wp-content/uploads/2019/08/Water-clarity-HELCOM-core-indicator-2018.pdf (Accessed 16 May 2020). Contributors beside authors are participants of HELCOM IN-Eutrophication project. Authors are from the Finnish Environment Institute (SYKE) and Secretariat of the Helsinki Comission.

FMI (2020). Ice conditions. Available at: https://en.ilmatieteenlaitos.fi/ice-conditions (Accessed 13 Jan 2020). FMI is The Finnish Meteorological Institute.

Forfinski-Sarkozi, N. A. and Parrish, C. E. (2016). Analysis of MABEL Bathymetry in Keweenaw Bay and Implications for ICESat-2's ATLAS. *Remote Sensing*, 8(772):21.

Furman, E., Pihlajamäki, M., Valipakka, P., and Myrberg, K. (2013). The Baltic Sea: Environment and Ecology. Helsinki. pp. 69, Baltic Sea presentation package. Originally produced by scientists from Helsinki University, The Finnish Institute of Marine Research and the Environmental Administration of Finland.

Gabbatiss, J. (2018). First ship crosses Arctic without an icebreaker as global warming causes ice sheets to melt. Independent (published 14 February 2018). Available at: https://www.independent.co.uk/environment/arctic-sea-route-first-ship-no-icebreaker-winter-icebergs-ice-shelf-teekay-russia-a8208596.html (Accessed 22 May 2020).

Gegiuc, A., Similä, M., Karvonen, J., Lensu, M., Mäkynen, M., and Vainio, J. (2018). Estimation of degree of sea ice ridging based on dual-polarized C-band SAR data. *The Cryosphere*, 12:343–364.

HELCOM (2018). State of the Baltic Sea – Second HELCOM holistic assessment 2011-2016. Available at: http://stateofthebalticsea.helcom.fi/in-brief/our-baltic-sea/ (Accessed 23 Jan 2020. Baltic Sea Environment Proceedings 155.

Hermanni, K. (2020). Private communication. A correspondence on water clarity in the Baltic with reference to HELCOM ICES data and recommendations on where and when the water clarity is best. Hermanni Kaartokallio is a Senior Research Scientist at the Finnish Environment Institute (SYKE).

Huang, L., Liu, B., Li, X., Zhang, Z., and Yu, W. (2017). Technical Evaluation of Sentinel-1 IW Mode Cross-Pol Radar Backscattering from the Ocean Surface in Moderate Wind Condition. *Remote Sensing*, 9(854):21.

Irish, J. L. and White, T. E. (1998). Coastal Engineering Applications of High-Resolution LIDAR Bathymetry. *Coastal Engineering*, 25:47–71.

Jakobsson, M., Stranne, C., O'Regan, M., Greenwood, S. L., Gustafsson, B., Humborg, C., and Weidner, E. (2019). Bathymetric properties of the Baltic Sea. *Ocean Sci.*, 14:905–924.

Karvonen, J. (2012). Operational SAR-based sea ice drift monitoring over the Baltic Sea. *Ocean Science*, 8:473–483.

Karvonen, J. (2020). Private communication. A correspondence on sea ice drift in the Baltic and which data was available on this during ice season 2018-2019.

Kedzierski, A. and Dings, J. (2012). Troubled waters: How to protect the Arctic from the growing impact of shipping. Copyright of 2012 Soft Free and European Federation for Transport and Environment (T&E).

Klotz, B. W., Neuenschwander, A., and Magruder, L. A. (2019). High-Resolution Ocean Waves and Wind Characteristics Determined by the ICESat-2 Land Surface Algorithm. *Geophysical Research Letters*, 47:10.

Kwok, R., Cunningham, G. F., Zwally, H. J., and Yi, D. (2007). Ice, Cloud, and land Elevation Satellite (ICESat) over Arctic sea ice: Retrieval of freeboard. *Journal of Geophysical Research*, 112(C12013):19.

Kwok, R., G., C., Hancock, D., Ivanoff, A., and Wimert, J. (2019a). Algorithm Theoretical Basis Document (ATBD) for Sea Ice Products. Available at: https://icesat-2.gsfc.nasa.gov/sites/default/files/page_files/ICESat2_ATL07_ATL10_ATBD_r002.pdf (Accessed 10 Feb 2020). ICE, CLOUD and Land Elevation Satellites (ICESat-2) Project, Goddard Space Flight Center, Greenbelt, Maryland. Release 002.

Kwok, R., Kacimi, S., Webster, M. A., Kurtz, N. T., and Petty, A. A. (2020). Arctic Snow Depth and Sea Ice Thickness From ICESat-2 and CryoSat-2 Freeboards: A First Examination. *Journal of Geophysical Research: Oceans*, 125(3).

Kwok, R., Markus, T., Kurtz, N. T., Petty, A. A., Neumann, T. A., Farrell, S. L., Cunningham, C. F., Hancock, D. W., Ivanoff, A., and Wimert, J. T. (2019b). Surface Height and Sea Ice freeboard of the Arctic Ocean From ICESat-2: Characteristics and Eearly Results. *Journal of Geophysical Research: Oceans*, 124:6942–6959.

Leppäranta, M. and Myrberg, K. (2009). Physical oceanography of the Baltic Sea. Springer-Praxis, Chichester. pp. 378.

Lewis, J., Leppäranta, M., and Granberg, H. (1993). Statistical properties of sea ice surface topography in the Baltic Sea. *Tellus*, 45A.

Leys, C., Ley, C., Klein, O., Bernard, P., and Licata, L. (2013). Detecting outliers: Do not use standard deviation around the mean, use absolute deviation around the median. *Journal of Experimental Social Psychology*, 49:764–766.

Li, Y., Gao, H., Jasinski, M. F., Zhanf, S., and Stoll, J. D. (2019). Deriving High-Resolution Reservoir Bathymetry From ICESat-2 Prototype Photon-Counting Lidar and Landsat Imagery. *IEEE Transcations on Geoscience and Remote Sensing*, 57(10):7883–7893.

Lund-Hansen, L. (2004). Diffuse attenuation coefficients Kd(PAR) at the estuarine North Sea – Baltic Sea transition: time-series, partitioning, absorption, and scattering. *Estuarine, Coastal and Shelf Science*, 61:251–259.

Mandlburger, G., Pfennigbauer, M., Steinbacher, F., and Pfeifer, N. (2011). Airborne Hydrographic LiDAR Mapping-Potential of a new technique for capturing shallow water bodies.

Markus, T., Neumann, T., Martino, A., Abdalati, W., Brunt, K., Csatho, B., Farrell, S., Fricker, H., Gardner, A., Harding, D., Jasinski, M., Kwow, R., Magruder, L., Lubin, D.,

Lutchke, S., Morison, J., Nelson, R., Neuenschwander, A., Palm, S., Popescu, S., Shum, C., Schutz, B., Smith, B., Yang, Y., and Zwally, J. (2017). The Ice, Cloud, and land Elevation Satellite-2 (ICESat-2): Science requirements, concept, and implementation. *Remote Sens. of Environment*, 90:260–273.

Matthews, J. L., Peng, G., Meier, W. N., and Brown, O. (2020). Sensitivity of Arctic Sea Ice Extent to Sea Ice Concentration Threshold Choice and Its Implication to Ice Coverage Decadal Trends and Statistical Projections. *Remote Sensing*, 12(807):17.

Mei, J. M., Maksym, T., Weissling, B., and Singh, H. (2019). Estimating early-winter Antarctic sea ice thickness from deformed ice morphology. *The Cryosphere*, 13:2915–2934.

NASA (2020a). ICESat-2. Available at: https://icesat-2.gsfc.nasa.gov/ (Accessed 15 Jan 2020).

NASA (2020b). Technical Specs. Available at: https://icesat-2.gsfc.nasa.gov/science/specs (Accessed 16 Jan 2020).

Neumann, T., Brenner, A., Hancock, D., Robbins, J., Saba, J., Harbeck, K., Gibbons, A., Lee, J., Luthcke, S., and Rebold, T. (2019a). Algorithm Theoretical Basis Document (ATBD) for Global Geolocated Photons ATL03. Available at: https://icesat-2.gsfc.nasa.gov/sites/default/files/page_files/ICESat2_ATL03_ATBD_r002.pdf (Accessed 30 Jan 2020). Goddard Space Flight Center, Greenbelt, Maryland, Release 002.

Neumann, T., Martino, A., Markus, T., Bae, S., Bock, M., Brenner, A., Brunt, K., Cavanaugh, J., Fernandes, S., Hancock, D., Harbeck, K., Lee, J., Kurtz, N., Luers, P., Luthcke, S., Magruder, L., Pennington, T., Ramos-Izquierdo, L., Rebold, T., Skoog, J., and Thomas, T. (2019b). The Ice, Cloud and Land Elevation Satellite-2 mission: A global geolocated photon product derived from the Advanced Topographic Laser Altimeter System. *Remote Sens. of Environment*, 233(111325):16.

Nielsen, K., Stenseng, L., Andersen, O. B., and Knudsen, P. (2017). The Performance and Potensials of the CryoSat-2 SAR and SARIn Modes for Lake Level Estimation. *Water*, 371(9):13.

NSIDC (2020a). ATLAS/ICESat-2 L2A Global Geolocated Photon Data, Version 2, User Guide. Available at: https://nsidc.org/data/atl03 (Accessed 10 Jan 2020). NSIDC (National Snow and Ice Data Center).

NSIDC (2020b). Ice formation. Available at: https://nsidc.org/cryosphere/seaice/characteristics/formation.html (Accessed 14 Jan 2020). NSIDC (National Snow and Ice Data Center).

Parrish, C. E., Magruder, L. A., Neuenschwander, A. L., Forfinski-Sarkozi, N., Alonzo, M., and Jasinki, M. (2019). Validation of ICESat-2 ATLAS Bathymetric and Aanalysis of ATLAS's Bathymetric Mapping Performance. *Remote Sensing*, 11(1634):19.

Pearson, K., Good, S., merchant, C. J., Prigent, C., Embury, O., and Donlon, C. (2019). Sea Surface Temperature in Global Analyses: Gains from the Copernicus Imaging Microwave Radiometer. *Remote Sensing*, 11(2362):13.

Pe'eri, S., Gardner, J. V., Ward, L. G., and Morrison, J. R. (2011). The Seafloor: A

Key Factor in Lidar Bottom Detection. *IEEE Transactions on Geoscience and Remote Sensing*, 49(3):1150–1156.

Pettersson, H., Brüning, T., Larsson, M., and Kalén, O. (2019). Wave climate in the Baltic Sea in 2018. Available at: https://helcom.fi/baltic-sea-trends/environment-fact-sheets/hydrography/wave-climate-in-the-baltic-sea-in-2018/ (Accessed 14 May 2020. HELCOM Baltic Sea Environment Fact Sheets.

Petty, A. A., Kurtz, N. T., Kwok, R., Markus, T., and Neumann, T. A. (2020). Winter Arctic sea ice thickness from ICESat-2 freeboards. *Journal of Geophysical Research: Oceans*, 125:28.

Preisendorfer, R. (1986). Secchi depth sicence: Visual optics of natural waters. *Limnology and Oceanography*, 31:909–926.

Quadros, N. D., Collier, P., and Fraser, C. (2008). Integration of Bathymetric and Topographic LIDAR: A preliminary investigation. *The International Archives of the Photogrammetry, Remote Sensing and Spatial Information Sciences.*, XXXVII(B8):1299–1304.

Rabenstein, L., Hendricks, S., Martin, T., Pfaffhuber, A., and Haas, C. (2009). Thickness and surface-properties of different sea-ice regimes within the Arctic Trans Polar Drift: Data from summers 2001, 2004 and 2007. *J. Geophys. Res*, 115(C12059):201–213.

Rheinheimer, G. (1998). Pollution in the Baltic Sea. *Naturwissenschaften*, 85(7):318–329.

Rinne, E. (2020a). Private communication. A correspondence on ridge spacing in the Baltic Sea, including information on the average amount of ridging and level ice and average sail width.

Rinne, E. (2020b). Private communication. A correspondence on mean sea surface (MSS) and restrictions in relation to MSS commonly used over sea ice.

Rinne, E. (2020c). Private communication. A correspondence on Secchi depth data and maximum Secchi depths that can be measured in the Baltic.

Ronkainen, I., Lehtiranta, J., Lensu, M., Rinne, E., Haapala, J., and Haas, C. (2018). Interannual sea ice thickness variability in the Bay of Bothnia. *The Cryosphere*, 12:3459–3476.

Seinä, A. and Palosuo, P. (1991). Duration of ice season and statistics of fast ice thickness along the finnish coast 1961-1990. Finnish Institute of Marine Research, Finland, Report 258, pp. 46.

Seppänen, J. (2020). Private communication. A correspondence on bathymetry in the Baltic, when algae is worse and which types of Earth Observation measurements and data could be useful for deciding when do look for bathymetric measurements.

Shokr, M. and Sinha, N. (2015). *Sea Ice: Physics and Remote Sensing*. Published under the aegis of the AGU Publication Committee and by John Wiley & Sons, Inc., Hoboken, New Jersey. Copyright by the American Geophysical Union (AGU), Washington D. C.

Skourup, H. (2010). *A study of Arctic sea ice freeboard heights, gravity anomalies and dynamic topography from ICESat measurements*. PhD thesis, Niels Bohr Institute, Uni-

versity of Copenhagen and Division of Geodynamics, National Space Institute (DTU Space), Copenhagen.

Skourup, H., Forsberg, R., and Braun, A. (2007). Gravity anomalies and sea ice thickness in the arctic ocean from icesat. 1st Meeting of the International Gravity Field Service : Gravity Field of the Earth ; Conference date: 28-08-2006 Through 01-09-2006.

Stasolla, K. and Neyt, X. (2018). An Operation Tool for the Automatic Detection and Removal of Border Noise in Sentinel-1 GRD Products. *Sensors*, 18(10):14.

Steel, A. and Neuhausser, S. (2002). Comparison of methods for measuring visual water clarity. *Journal of the North American Benthological Society*, 21:236–335.

Stenseth, N. C., Ottersen, G., Hurrell, J. W., and Belgrano, A. (2004). *Marine Ecosystem and Climate Variation - The North Atlantic, A Comparative Perspective*, volume 1. Oxford University Press, Great Clarendon Street, Oxford OX2 6DP.

Tan, B., Li, Z., Lu, P., Haas, C., and Nicolaus, M. (2012). Morphology of sea ice pressure ridges in the northwestern Weddell Sea in winter. *J. Geophys. Res.*, 117(C06024):13.

Tilling, R., Ridout, A., Shepherd, A., Laxon, S., and Giles, K. (2020). Determining sea ice thickness from space-borne radar altimetry. Available at: https://cpom.org.uk/determining-sea-ice-thickness-from-space-borne-radar-altimetry/ (Accessed 08 Jan 2020).

United States Coast Guard (1953). Aid to Navigation Manual. Available as free Ebook (if you sign in) at: https://play.google.com/store/books/details?id=wbBIAQAAIAAJ&rdid=book-wbBIAQAAIAAJ&rdot=1 (Accessed 16 May 2020). Manual for navigation by United States Coast Guard, published by U.S. Government Printing Office. pp 954.

Uotila, P., Vihma, T., and Haapala, J. (2015). Atmospheric and oceanic conditions and the extremely low Bothnian Bay sea ice extent in 2014/2015. *Geophys. Res. Lett.*, 42:7740–7749.

Wang, X., Glennia, C., and Pan, Z. (2018). Weak Echo Detection from Single Photon Lidar Data Using a Rigorous Adaptive Ellipsoid Searching Algorithm. *Remote Sensing*, 10(1035):15.

Wernecke, A. and Kaleschke, L. (2015). Lead detection in Arctic sea ice from CryoSat-2: quality assessment, lead area fraction and width distribution. *The Cryosphere*, (9):1955–1968.

Williams, G. D., Maksym, T., Kunz, C., Murphy, C., Kimball, P., and Singh, H. (2015). Thick and deformed Antarctic sea ice mapped with autonomous underwater vehicles. *Nat. Geosci.*, 8:61–67.

WMO (2010). *Sea-Ice Information Services in the World*, volume 574. 2010 edition. World Meteorological Organisation (WMO).

Wozencraft, J. M. and Millar, D. (2005). Airborne LIDAR and Integrated Technologies for Coastal Mapping and Nautical Charting. *Marine Technology Society Journal*, 39(3):27–35.

Zwally, H. J., Yi, D., Kwok, R., , and Zhao, Y. (2008). ICESat measurements of sea ice freeboard and estimates of sea ice thickness in the Weddell Sea. *Journal of Geophysical Research*, 113(C02S15):17.

A ICESat-2

A.1 Data products

ICESat-2's primary data products adapted from Markus et al. (2017).

- **ATL00 - Telemetry data:** Raw ATLAS telemetry in packet format.
- **ATL01 - Reformatted Telemetry Parsed:** Parsed, partially reformatted into Hierarchical Data Format 5 (HDF5), generated daily, segmented into several minute granules.
- **ATL02 - Science Unit Converted Telemetry:** Photon time of flight, corrected for instrument effects. Includes all photons, pointing data, spacecraft position, housekeeping data, engineering data, and raw atmospheric profiles, segmented into several minute granules.
- **ATL03 - Global Geolocated Photon Data:** Precise latitude, longitude and elevation for every received photon, arranged by beam in the along-track direction. Photons classified by signal vs. background, as well as by surface type (land ice, sea ice, land, ocean), including all geophysical corrections (e.g. Earth tides, atmospheric delay, etc.…). Segmented into several minute granules.
- **ATL04 - Uncalibrated Backscatter Profiles:** Along-track atmospheric backscatter data, 25 times per second. Includes calibration coefficients for polar regions. Segmented into several minute granules.
- **ATL06 - Land Ice Elevation**: Surface height for each beam with along and across-track slopes calculated for each beam pair. Posted at 40 m along-track; segmented into several minute granules.
- **ATL07 - Arctic/Antarctic Sea Ice Elevation:** Height of sea ice and open water leads at varying length scale based on returned photo rate for each beam presented along-track.
- **ATL08 - Land Water Vegetation Elevation:** Height of ground including canopy surface posted at variable length scales relative to signal level, for each beam presented along-track. Where data permits include canopy height, canopy cover percentage, surface slope and roughness, and apparent reflectance.
- **ATL09 - Calibrated Backscatter and Cloud Characteristics:** Along-track cloud and other significant atmosphere layer heights, blowing snow, integrated backscatter, and optical depth.
- **ATL10 - Arctic/Antarctic Sea Ice Freeboard:** Estimate of sea ice freeboard over specific spatial scales using all available sea surface height measurements. Contains statistics of sea surface and sea ice heights.
- **ATL11 - Antarctica/Greenland Ice Sheet H(t) Series:** Time series of height at points on the ice sheet, calculated based on repeat tracks and/or cross-overs.
- **ATL12 - Ocean Elevation:** Surface height at specific length scale. Where data permits include estimates of height distribution, roughness, surface slope, and apparent reflectance.
- **ATL13 - Inland Water Height:** Along-track inland and near shore water surface height distribution within water mask. Where data permit, include roughness, slope and aspect.

A.2 Photon heights

Graphs of ICESat-2 photon heights for January to March 2019 before using signal confidence parameter in pre-processing. Colors denote which beam is used.

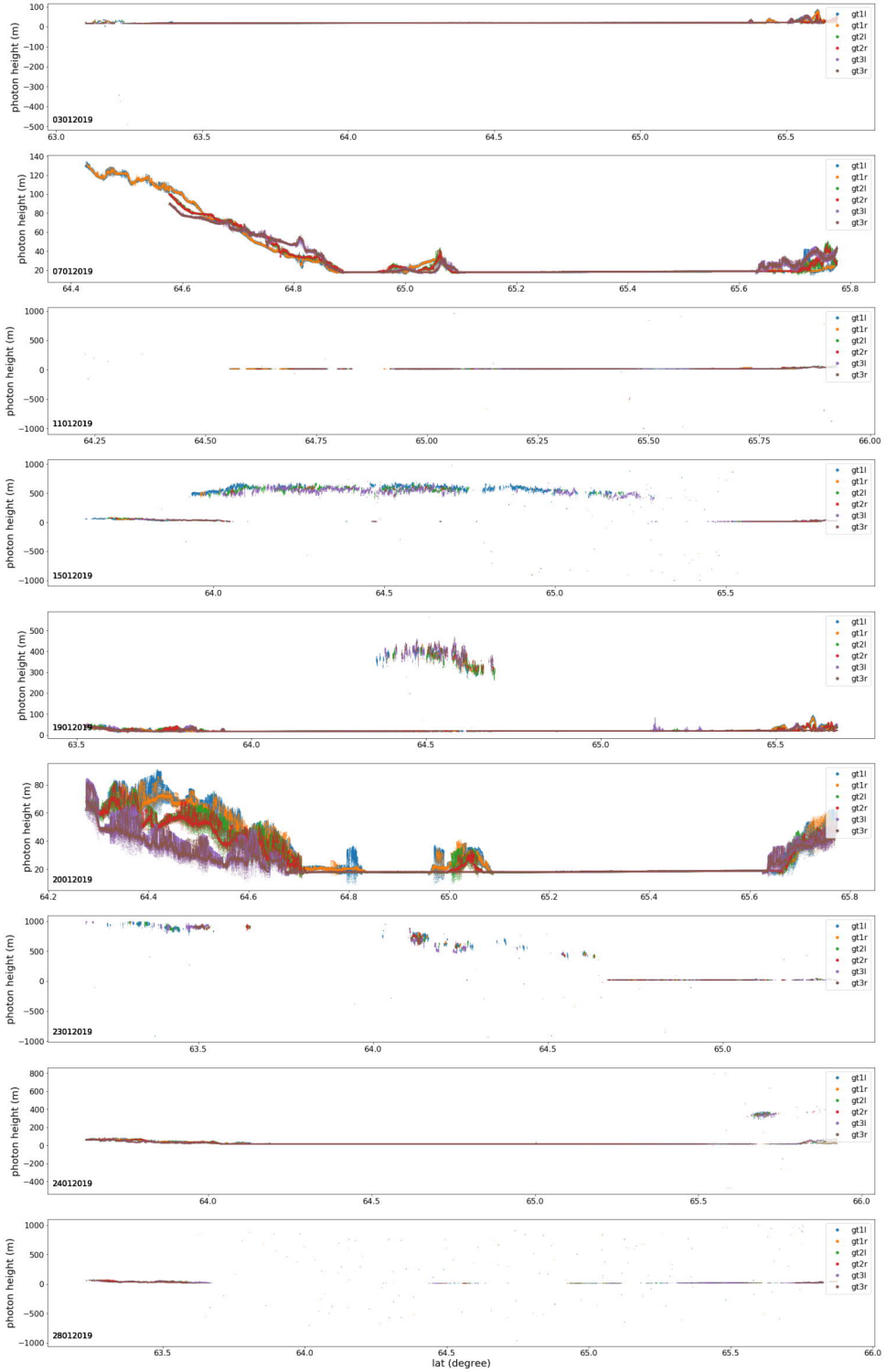

Figure A.1: Photon observations from ICESat-2 observed in January 2019 from all six beams.

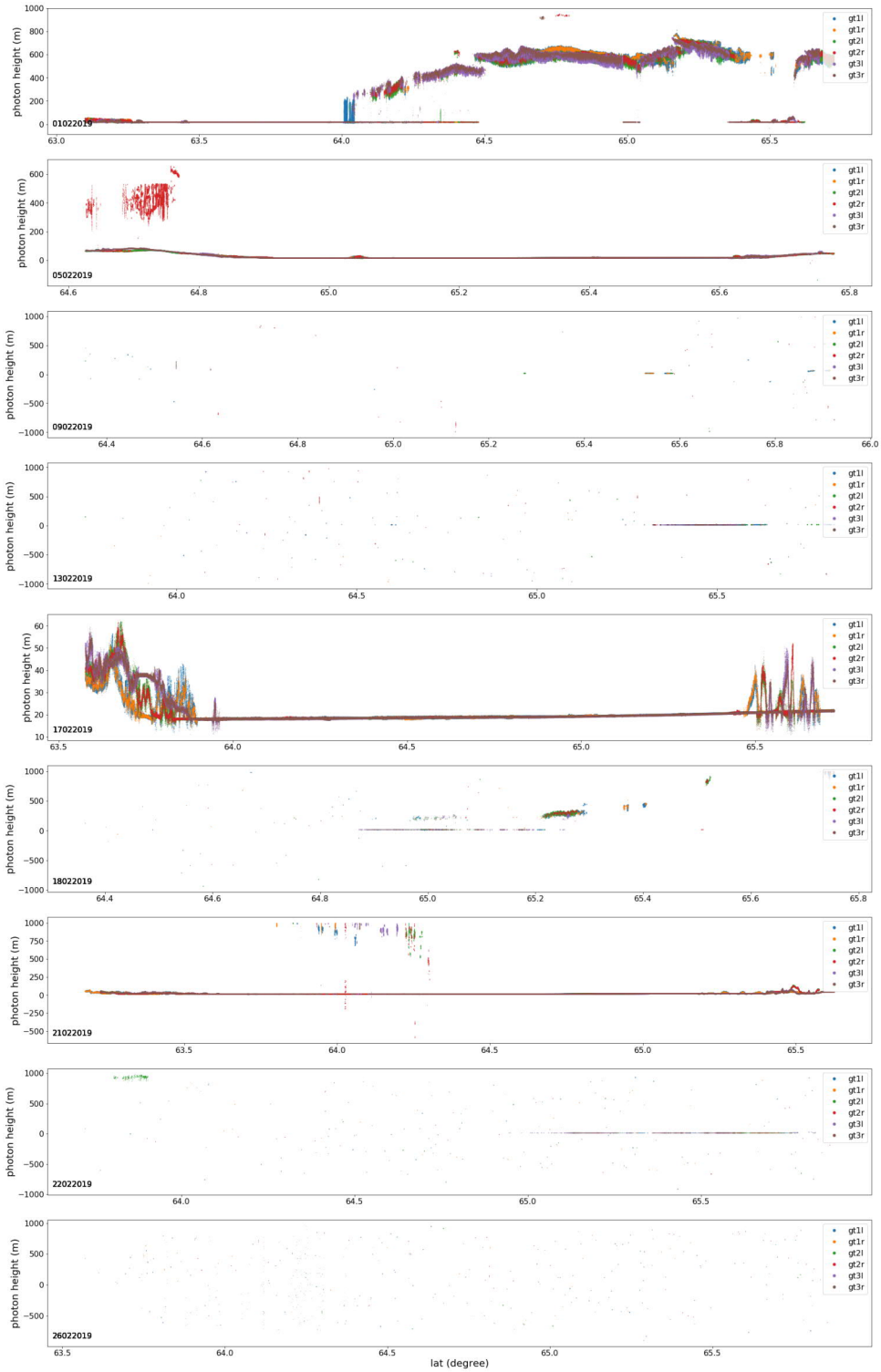

Figure A.2: Photon observations from ICESat-2 observed in February 2019 from all six beams.

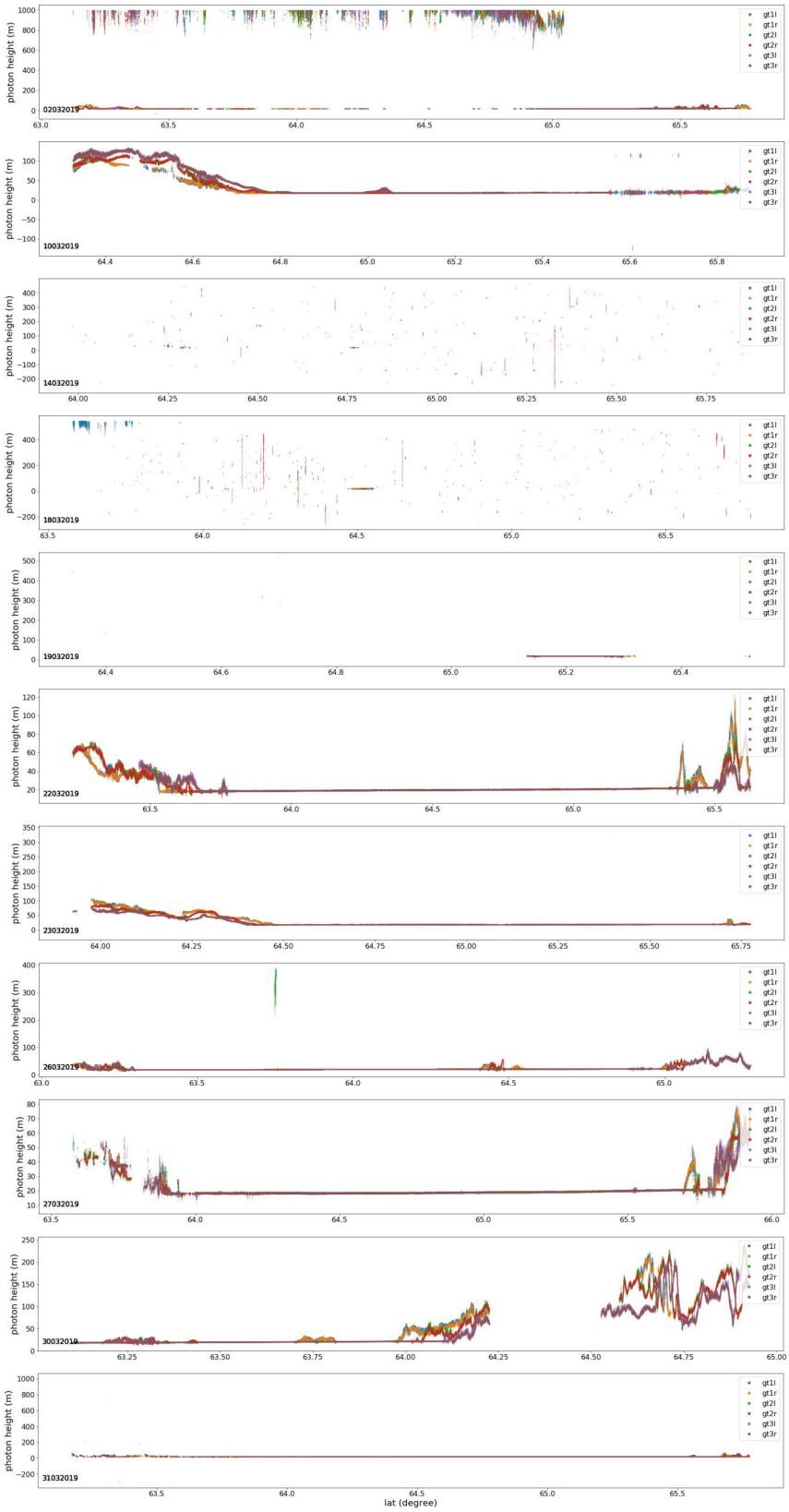

Figure A.3: Photon observations from ICESat-2 observed in March 2019 from all six beams.

A.3 Significance confidence quality photons

ICESat-2 photons acquired over the Bay of Bothnia during January to March 2019 shown by a signal confidence quality parameter.

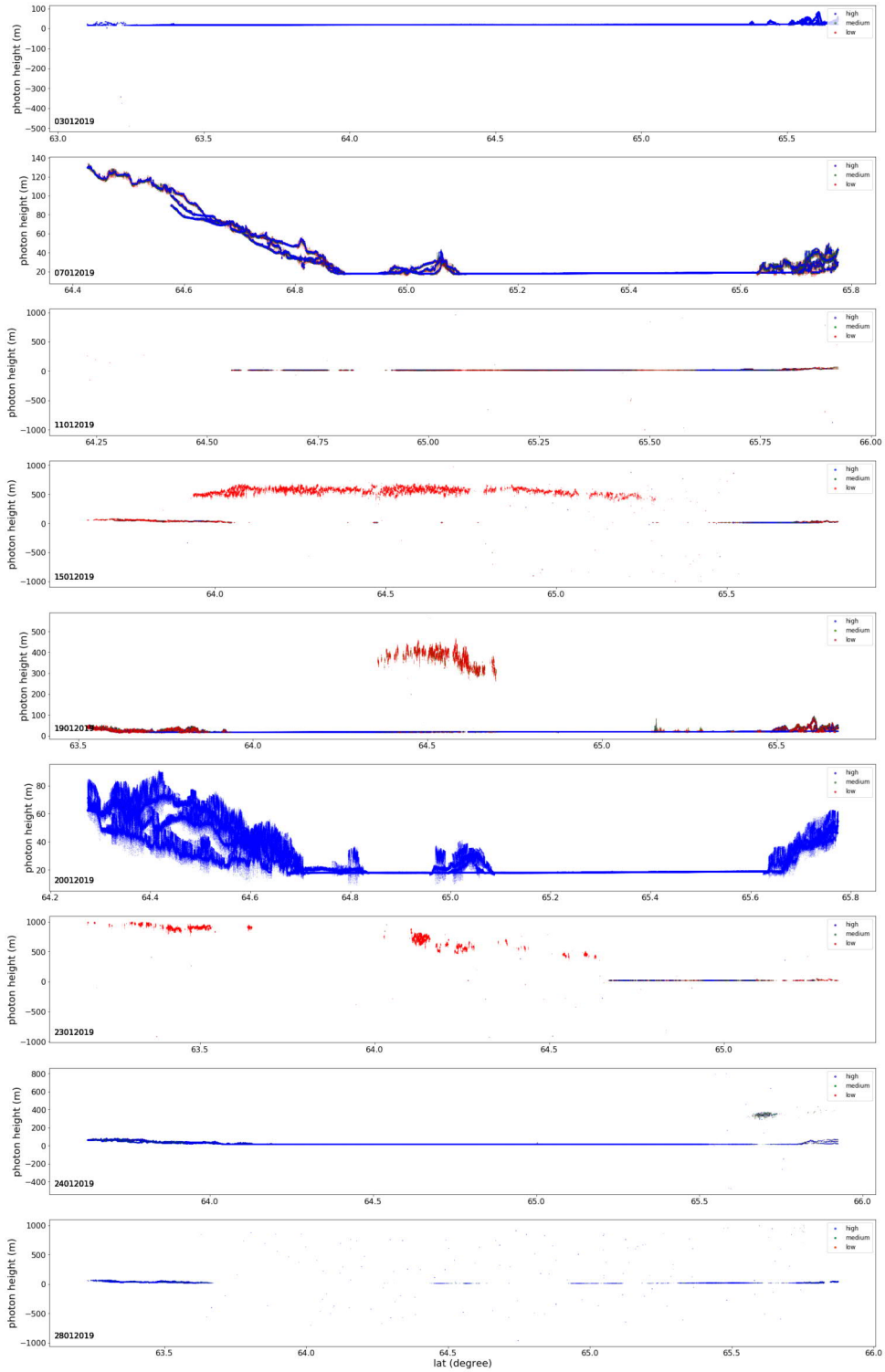

Figure A.4: Photon observations from ICESat-2 presented by signal confidence observed in January 2019 from all six beams. Red, green and blue denotes low, medium and high signal confidence, respectively.

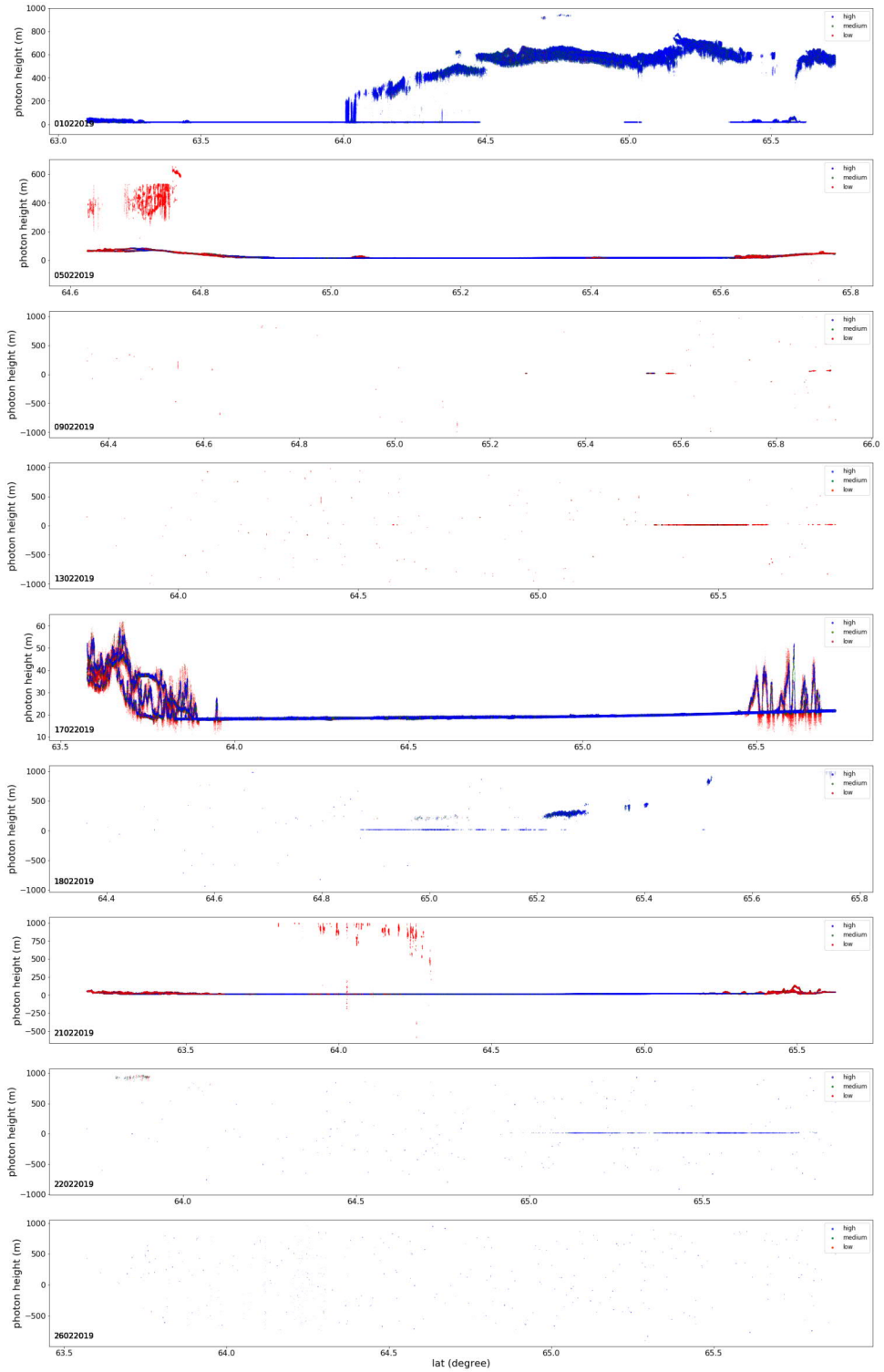

Figure A.5: Photon observations from ICESat-2 presented by signal confidence observed in February 2019 from all six beams. Red, green and blue denotes low, medium and high signal confidence, respectively.

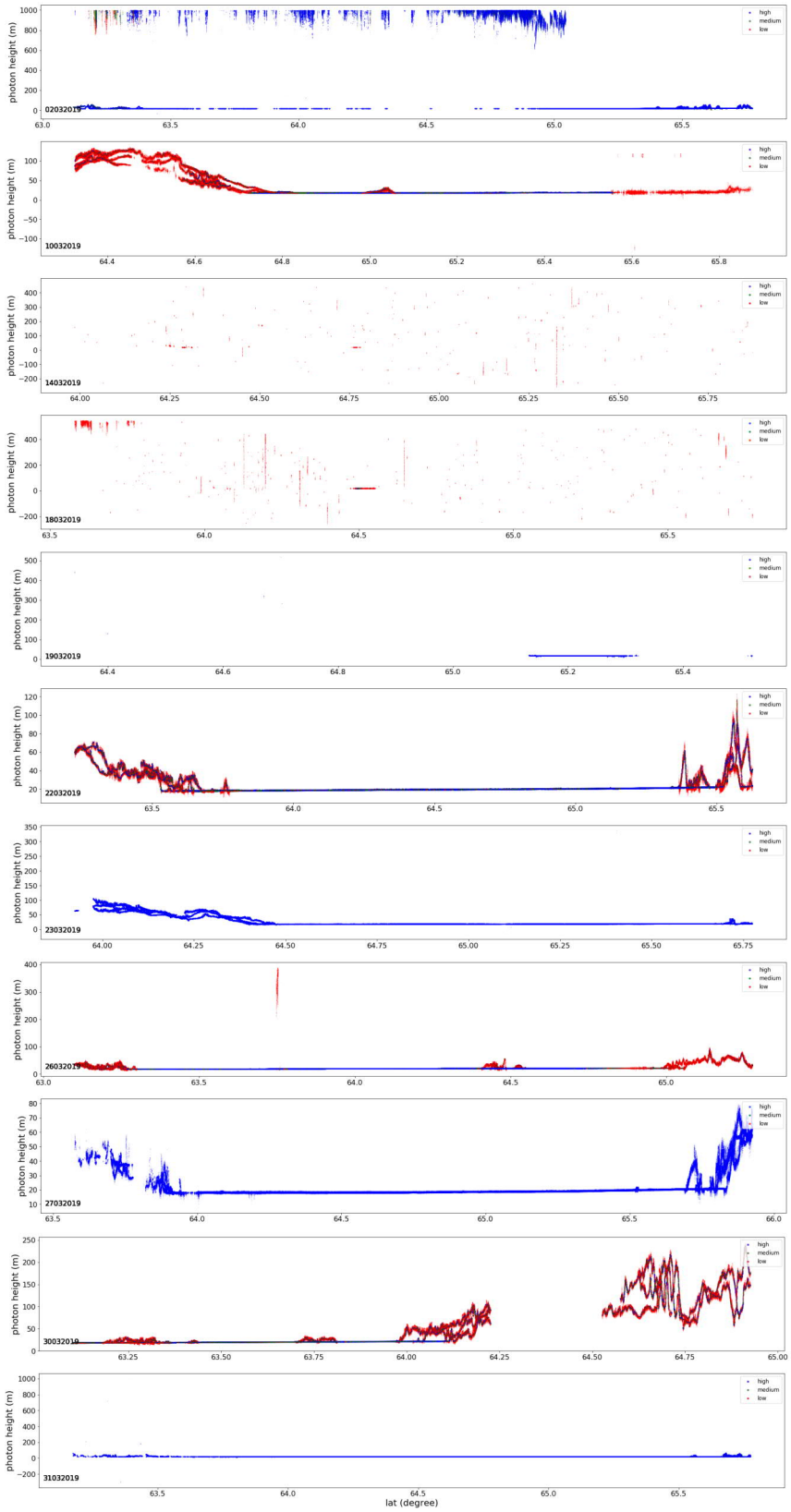

Figure A.6: Photon observations from ICESat-2 presented by signal confidence observed in March 2019 from all six beams. Red, green and blue denotes low, medium and high signal confidence, respectively.

A.4 Statistics on confidence quality

Statistics of amount of the photon observations from each date in each month is partitioned as high, medium and low signal confidence.

Table A1: Distribution of the photons from January 2019 divided by the signal confidence level.

	3/1	7/1	11/1	15/1	19/1	20/1	23/1	24/1	28/1
High [%]	99.98	98.83	82.97	53.06	96.70	99.99	79.23	99.59	98.52
Med [%]	00.02	02.75	11.10	08.53	01.76	00.01	04.01	00.36	01.40
Low [%]	00.00	00.42	05.93	38.40	01.54	00.00	16.76	00.05	00.08

Table A2: Distribution of the photons from February 2019 divided by the signal confidence level.

	1/2	5/2	9/2	13/2	17/2	18/2	21/2	22/2	26/2
High [%]	98.68	96.28	47.79	32.02	97.58	89.88	96.81	89.88	86.62
Med [%]	01.27	01.69	17.83	22.93	01.31	10.21	01.58	07.38	09.35
Low [%]	00.05	02.03	34.38	45.05	01.61	00.72	01.91	02.74	04.03

Table A3: Distribution of the photons from March 2019 divided by the signal confidence level.

	2/3	10/3	14/3	18/3	19/3	22/3	23/3	26/3	27/3	30/3	31/3
High [%]	99.63	92.04	01.19	33.57	99.99	95.17	99.99	97.99	99.99	86.13	99.99
Med [%]	00.30	03.69	06.30	08.41	00.01	03.06	00.01	01.08	00.01	07.34	00.01
Low [%]	00.07	04.00	92.51	58.02	00.00	01.77	00.00	00.93	00.00	06.53	00.00

B Code

This section includes coding used to extract, format and prepare data for analysis by Python (Jupyter Notebook). Some of the results, such as specific statistical parameters, distribution graphs and similar have been calculated by additional coding in R studio and have not been provided in Appendix. Maps over the Bay of Bothnia (sea ice study) and ICESat-2 photon graphs are generated in Python.

```
import pyproj
from astropy.time import Time
import h5py
import numpy as np
import matplotlib.pyplot as plt
import pandas as pd
from netCDF4 import Dataset
from mpl_toolkits.basemap import Basemap
from itertools import chain
import sys

def list_files_local(path):
    ''' Get file list from local folder. '''
    from glob import glob
    return glob(path)

def gps2dyr(time):
    '''Convert GPS time to decimal years'''
    return Time(time, format='gps').decimalyear

def track_type(time, lat, tmax=1):
    '''
    Separate tracks into ascending and descending.

    Defines tracks as segments with time breaks > tmax ,
    and tests whether lat increases or decreases w/time.
    '''
    tracks = np.zeros(lat.shape) # generates track segment
    tracks[0:np.argmax(np.abs(lat))] = 1 # set values for segment
    i_asc = np.zeros(tracks.shape, dtype=bool) # output index array

    # loop through individual segments
    for track in np.unique(tracks):

        i_track, = np.where(track == tracks) # get all pts from seg

        if len(i_track) < 2: continue

        # Test if lat increase (asc) or descreases (des) with time
        i_min = time[i_track].argmin()
        i_max = time[i_track].argmax()
        lat_diff = lat[i_track][i_max] - lat[i_track][i_min]

        # Determine track trype
        if lat_diff > 0: i_asc[i_track] = True
```

```
    return i_asc, np.invert(i_asc)

def transform_coord(proj1, proj2, x, y):
    '''
    Transform coordinates from proj1 to proj2 (EPSG num).

    Example EPSG projs:
        Geodetic (lon/lat): 4326
        Polar Stereo AnIS (x/y): 3031
        Polar Stereo GrIS (x/y): 3413
    '''
    # Set full EPSG projection strings
    proj1 = pyproj.Proj("+init=EPSG:"+str(proj1))
    proj2 = pyproj.Proj("+init=EPSG:"+str(proj2))
    return pyproj.transform(proj1, proj2, x, y)  # convert

def read_h5(fname, vnames=[]):
    '''Simple HDF5 reader'''
    with h5py.File(fname, 'r') as f:
        return [f[v][:] for v in vnames]
```

Listing B.1: Initial utility functions

```
def read_data(fname, bbox=None):
    '''
    Read ATL03 data file and output 6 reduced files.

    Extract variables of interest and separate the ATL03 file
    into each beam (ground track) and ascending/descending orbits.
    '''

    # Each beam is a group
    group = ['/gt1l', '/gt1r', '/gt2l', '/gt2r', '/gt3l', '/gt3r']

    # Loop through beams
    for k,g in enumerate(group):

        #-----------------------------------#
        # 1) Read in data for a single beam #
        #-----------------------------------#

        # Load variables into memory (more can be added!)
        with h5py.File(fname, 'r') as fi:
            sc = fi['/orbit_info/sc_orient'][:]

            #if sc == 1:
            #    g = ['/gt3r', '/gt3l', '/gtl2r', '/gt2l', '/gt1r', '/
                gt1l']

            lat = fi[g+ '/heights/lat_ph'][:]
            lon = fi[g+ '/heights/lon_ph'][:]
            h_ph = fi[g+ '/heights/h_ph'][:]
            t_dt = fi[g+'/heights/delta_time'][:]
            t_ref = fi['/ancillary_data/atlas_sdp_gps_epoch'][:]
            geoid = fi[g+'/geophys_corr/geoid'][:]
            dac = fi[g+'/geophys_corr/dac'][:]
```

```
            ocean = fi[g+'/geophys_corr/tide_ocean'][:]
            signal_conf = fi[g+ '/heights/signal_conf_ph'][:, 2]
            signal_conf_ocean = fi[g+'/heights/signal_conf_ph'][:, 1]
            signal_conf_inland = fi[g+'/heights/signal_conf_ph'][:, 4]
            tide_load = fi[g+'/geophys_corr/tide_load'][:]
            ref_lat = fi[g+'/geolocation/reference_photon_lat'][:]
            ref_lon = fi[g+'/geolocation/reference_photon_lon'][:]
            bcr = fi[g+'/bckgrd_atlas/bckgrd_rate'][:]
            delta_t = fi[g+ '/bckgrd_atlas/delta_time'][:]

            #orb = np.full_like(h_ph, k)

        #-------------------------------------------#
        # 2) Filter data according region and quality #
        #-------------------------------------------#

        # Select a region of interest
        if bbox:
            lonmin, lonmax, latmin, latmax = bbox
            bbox_mask = (lon >= lonmin) & (lon <= lonmax) & \
                        (lat >= latmin) & (lat <= latmax)
            bbox_maskref = (ref_lon >= lonmin) & (ref_lon <= lonmax) &
                \
                           (ref_lat >= latmin) & (ref_lat <= latmax)
        else:
            bbox_mask = np.ones_like(lat, dtype=bool)  # get all
            bbox_maskref = np.ones_like(ref_lat, dtype=bool)

        # Only keep good data, and data inside bbox
        mask = (np.abs(h_ph) < 1e3) & (bbox_mask == 1) #& (signal_conf
            > 3)
        mask_ref = bbox_maskref == 1

        # Update variables
        lat, lon, h_ph, t_dt, signal_conf, signal_conf_ocean,
            signal_conf_inland = lat[mask], lon[mask], h_ph[mask], t_dt
            [mask], signal_conf[mask], signal_conf_ocean[mask],
            signal_conf_inland[mask]
        geoid, dac, ocean, ref_lat, ref_lon = geoid[mask_ref], dac[
            mask_ref], ocean[mask_ref], ref_lat[mask_ref], ref_lon[
            mask_ref]

        # Test for no data
        if len(h_ph) == 0: continue

        #-------------------------------------#
        # 3) Convert time and separate tracks #
        #-------------------------------------#

        # Time in GPS seconds (secs since 1980...)
        t_gps, delta_t_gps = t_ref + t_dt, t_ref + delta_t

        # Time in decimal years
        t_year, delta_t_year = gps2dyr(t_gps), gps2dyr(delta_t_gps)

        # Determine orbit type
        i_asc, i_des = track_type(t_year, lat)
```

```
        #-----------------------#
        # 4) Save selected data #
        #-----------------------#

        # Define output file name
        ofile = fname.replace('.h5', '_'+g[1:]+'.h5')

        # Save variables
        with h5py.File(ofile, 'w') as f:
            #f['orbit'] = orb
            f['lon'] = lon
            f['lat'] = lat
            f['h_elv'] = h_ph
            f['t_year'] = t_year
            f['geoid'] = geoid
            f['dac'] = dac
            f['ocean'] = ocean
            f['signal_conf'] = signal_conf
            f['signal_conf_ocean'] = signal_conf_ocean
            f['signal_conf_inland'] = signal_conf_inland
            f['ref_lat'] = ref_lat
            f['ref_lon'] = ref_lon
            f['bcr'] = bcr
            f['delta_t_year'] = delta_t_year

            print('out ->', ofile)
```

Listing B.2: Extracting as well as initial pre-processing and formatting of ICESat-2 ATL03 data. Outcomment "signal_conf > 3" in mask to include only high confidence photons. Data is saved by beams (six output files will be generated)

```
# Example of loading data
lon_gt1l, lat_gt1l, t_gt1l, h_gt1l, sig_conf_gt1l,
    signal_conf_ocean_gt1l, signal_conf_inland_gt1l, geoid_gt1l,
    dac_gt1l, ref_lat_gt1l, ref_lon_gt1l, ocean_gt1l, bcr_gt1l,
    delta_t_gt1l = read_h5('D:/ICESat-2/data/march/
    ATL03_20190327182253_13640205_002_01_gt1l.h5', ['lon', 'lat', '
    t_year', 'h_elv', 'signal_conf', 'signal_conf_ocean', '
    signal_conf_inland', 'geoid', 'dac', 'ref_lat', 'ref_lon', 'ocean',
     'bcr', 'delta_t_year'])
lon_gt1r, lat_gt1r, t_gt1r, h_gt1r, sig_conf_gt1r,
    signal_conf_ocean_gt1r, signal_conf_inland_gt1r, geoid_gt1r,
    dac_gt1r, ref_lat_gt1r, ref_lon_gt1r, ocean_gt1r, bcr_gt1r,
    delta_t_gt1r = read_h5('D:/ICESat-2/data/march/
    ATL03_20190327182253_13640205_002_01_gt1r.h5', ['lon', 'lat', '
    t_year', 'h_elv', 'signal_conf', 'signal_conf_ocean', '
    signal_conf_inland', 'geoid', 'dac', 'ref_lat', 'ref_lon', 'ocean',
     'bcr', 'delta_t_year'])
lon_gt2l, lat_gt2l, t_gt2l, h_gt2l, sig_conf_gt2l,
    signal_conf_ocean_gt2l, signal_conf_inland_gt2l, geoid_gt2l,
    dac_gt2l, ref_lat_gt2l, ref_lon_gt2l, ocean_gt2l, bcr_gt2l,
    delta_t_gt2l = read_h5('D:/ICESat-2/data/march/
    ATL03_20190327182253_13640205_002_01_gt2l.h5', ['lon', 'lat', '
    t_year', 'h_elv', 'signal_conf', 'signal_conf_ocean', '
    signal_conf_inland', 'geoid', 'dac', 'ref_lat', 'ref_lon', 'ocean',
     'bcr', 'delta_t_year'])
```

```
lon_gt2r, lat_gt2r, t_gt2r, h_gt2r, sig_conf_gt2r,
    signal_conf_ocean_gt2r, signal_conf_inland_gt2r, geoid_gt2r,
    dac_gt2r, ref_lat_gt2r, ref_lon_gt2r, ocean_gt2r, bcr_gt2r,
    delta_t_gt2r = read_h5('D:/ICESat-2/data/march/
    ATL03_20190327182253_13640205_002_01_gt2r.h5', ['lon', 'lat', '
    t_year', 'h_elv', 'signal_conf', 'signal_conf_ocean', '
    signal_conf_inland', 'geoid', 'dac', 'ref_lat', 'ref_lon', 'ocean',
     'bcr', 'delta_t_year'])
lon_gt3l, lat_gt3l, t_gt3l, h_gt3l, sig_conf_gt3l,
    signal_conf_ocean_gt3l, signal_conf_inland_gt3l, geoid_gt3l,
    dac_gt3l, ref_lat_gt3l, ref_lon_gt3l, ocean_gt3l, bcr_gt3l,
    delta_t_gt3l = read_h5('D:/ICESat-2/data/march/
    ATL03_20190327182253_13640205_002_01_gt3l.h5', ['lon', 'lat', '
    t_year', 'h_elv', 'signal_conf', 'signal_conf_ocean', '
    signal_conf_inland', 'geoid', 'dac', 'ref_lat', 'ref_lon', 'ocean',
     'bcr', 'delta_t_year'])
lon_gt3r, lat_gt3r, t_gt3r, h_gt3r, sig_conf_gt3r,
    signal_conf_ocean_gt3r, signal_conf_inland_gt3r, geoid_gt3r,
    dac_gt3r, ref_lat_gt3r, ref_lon_gt3r, ocean_gt3r, bcr_gt3r,
    delta_t_gt3r = read_h5('D:/ICESat-2/data/march/
    ATL03_20190327182253_13640205_002_01_gt3r.h5', ['lon', 'lat', '
    t_year', 'h_elv', 'signal_conf', 'signal_conf_ocean', '
    signal_conf_inland', 'geoid', 'dac', 'ref_lat', 'ref_lon', 'ocean',
     'bcr', 'delta_t_year'])
```

Listing B.3: Example of how to load the formatted ICESat-2 data

```
# Load FIS ice charts
def icechart_load_2(fileaname):
    root_chart = Dataset(filename, 'r')
    root_chart.variables.keys()
    lat_DIR = root_chart.variables['lat'][:]
    lon_DIR = root_chart.variables['lon'][:]
    DIR = root_chart.variables['kFmiIceType'][:]
    lat2 = np.array(lat_DIR.data[:])
    lon2 = np.array(lon_DIR.data[:])
    data2 = np.array(DIR.data[0, :, :])
    DIR_mask = DIR.mask[:]

    # Apply land mask
    for i in list(range(0,(3120-1))):
        for j in list(range(0,(2640-1))):
            if DIR_mask[0,i, j] is True:
                data2[i, j] = np.nan

    return data2, lat2, lon2

filename = 'D:/ICESat-2/charts/20190327140000_icechart.nc'
data2_27032019, lat2_27032019, lon2_27032019 = icechart_load_2(
    filename)
filename = 'D:/ICESat-2/charts/20190323140000_icechart.nc'
data2_23032019, lat2_23032019, lon2_23032019 = icechart_load_2(
    filename)
filename = 'D:/ICESat-2/charts/20190217140000_icechart.nc'
data2_17022019, lat2_17022019, lon2_17022019 = icechart_load_2(
    filename)
filename = 'D:/ICESat-2/charts/20190201140000_icechart.nc'
```

```
data2_01022019, lat2_01022019, lon2_01022019 = icechart_load_2(
    filename)
```

Listing B.4: Load relevant ice charts from FIS netcdf files

```
# Masking of geoid values with threshold of 1000m
def mask_geoid(geoid, lat, lon, ocean, dac):
    mask = (geoid < 1e3) & (ocean < 1e3) & (dac < 1e3)
    geoid, lat, lon, ocean, dac = geoid[mask], lat[mask], lon[mask],
        ocean[mask], dac[mask]
    return geoid, lat, lon, ocean, dac

geoid_gt1l, ref_lat_gt1l, ref_lon_gt1l, ocean_gt1l, dac_gt1l =
    mask_geoid(geoid_gt1l, ref_lat_gt1l, ref_lon_gt1l, ocean_gt1l,
    dac_gt1l)
geoid_gt1r, ref_lat_gt1r, ref_lon_gt1r, ocean_gt1r, dac_gt1r =
    mask_geoid(geoid_gt1r, ref_lat_gt1r, ref_lon_gt1r, ocean_gt1r,
    dac_gt1r)
geoid_gt2l, ref_lat_gt2l, ref_lon_gt2l, ocean_gt2l, dac_gt2l =
    mask_geoid(geoid_gt2l, ref_lat_gt2l, ref_lon_gt2l, ocean_gt2l,
    dac_gt2l)
geoid_gt2r, ref_lat_gt2r, ref_lon_gt2r, ocean_gt2r, dac_gt2r =
    mask_geoid(geoid_gt2r, ref_lat_gt2r, ref_lon_gt2r, ocean_gt2r,
    dac_gt2r)
geoid_gt3l, ref_lat_gt3l, ref_lon_gt3l, ocean_gt3l, dac_gt3l =
    mask_geoid(geoid_gt3l, ref_lat_gt3l, ref_lon_gt3l, ocean_gt3l,
    dac_gt3l)
geoid_gt3r, ref_lat_gt3r, ref_lon_gt3r, ocean_gt3r, dac_gt3r =
    mask_geoid(geoid_gt3r, ref_lat_gt3r, ref_lon_gt3r, ocean_gt3r,
    dac_gt3r)

# Total geophysical correction to be applied
corr_gt1l = geoid_gt1l + ocean_gt1l + dac_gt1l
corr_gt1r = geoid_gt1r + ocean_gt1r + dac_gt1r
corr_gt2l = geoid_gt2l + ocean_gt2l + dac_gt2l
corr_gt2r = geoid_gt2r + ocean_gt2r + dac_gt2r
corr_gt3l = geoid_gt3l + ocean_gt3l + dac_gt3l
corr_gt3r = geoid_gt3r + ocean_gt3r + dac_gt3r
```

Listing B.5: Masking of geoid values

```
# Mask photons by signal confidence 4 (if not already applied when
    extracting photons)
def mask(lat, lon, h, sign, t):
    mask_high = sign == 4
    lat_masked, lon_masked, h_masked, sign_masked, t_masked = lat[
        mask_high], lon[mask_high], h[mask_high], sign[mask_high], t[
        mask_high]
    return lat_masked, lon_masked, h_masked, sign_masked, t_masked

m_lat_gt1l, m_lon_gt1l, m_h_gt1l, m_sig_conf_gt1l, m_t_gt1l = mask(
    lat_gt1l, lon_gt1l, h_gt1l, sig_conf_gt1l, t_gt1l)
m_lat_gt1r, m_lon_gt1r, m_h_gt1r, m_sig_conf_gt1r, m_t_gt1r = mask(
    lat_gt1r, lon_gt1r, h_gt1r, sig_conf_gt1r, t_gt1r)
m_lat_gt2l, m_lon_gt2l, m_h_gt2l, m_sig_conf_gt2l, m_t_gt2l = mask(
    lat_gt2l, lon_gt2l, h_gt2l, sig_conf_gt2l, t_gt2l)
m_lat_gt2r, m_lon_gt2r, m_h_gt2r, m_sig_conf_gt2r, m_t_gt2r = mask(
    lat_gt2r, lon_gt2r, h_gt2r, sig_conf_gt2r, t_gt2r)
```

```
m_lat_gt3l, m_lon_gt3l, m_h_gt3l, m_sig_conf_gt3l, m_t_gt3l = mask(
    lat_gt3l, lon_gt3l, h_gt3l, sig_conf_gt3l, t_gt3l)
m_lat_gt3r, m_lon_gt3r, m_h_gt3r, m_sig_conf_gt3r, m_t_gt3r = mask(
    lat_gt3r, lon_gt3r, h_gt3r, sig_conf_gt3r, t_gt3r)
```

Listing B.6: Masking photons by signal confidence with value of 4 in case this has not been applied when formatting and extracting the data properly

```
# Mask photons by given bounding box (area of interest, AOI)
def mask_bbox(lat, lon, h, sign, bbox, t):
    lonmin, lonmax, latmin, latmax = bbox
    bbox_mask = (lon >= lonmin) & (lon <= lonmax) & \
                (lat >= latmin) & (lat <= latmax)

    lat_masked, lon_masked, h_masked, sign_masked, t_masked = lat[
        bbox_mask], lon[bbox_mask], h[bbox_mask], sign[bbox_mask], t[
        bbox_mask]
    return lat_masked, lon_masked, h_masked, sign_masked, t_masked

# Mask geophysical corrections (reference photons) by bounding box (
    area of interest, AOI)
def mask_bbox2(lat, lon, geoid, bbox):
    lonmin, lonmax, latmin, latmax = bbox
    bbox_mask = (lon >= lonmin) & (lon <= lonmax) & \
                (lat >= latmin) & (lat <= latmax)

    lat, lon, geoid = lat[bbox_mask], lon[bbox_mask], geoid[bbox_mask]
    return lat, lon, geoid


bbox = [20.0, 27, 63., 66.]  # example of bounding box used
mb_lat_gt1l, mb_lon_gt1l, mb_h_gt1l, mb_sig_conf_gt1l, mb_t_gt1l =
    mask_bbox(m_lat_gt1l, m_lon_gt1l, m_h_gt1l, m_sig_conf_gt1l, bbox,
    m_t_gt1l)
mb_lat_gt1r, mb_lon_gt1r, mb_h_gt1r, mb_sig_conf_gt1r, mb_t_gt1r =
    mask_bbox(m_lat_gt1r, m_lon_gt1r, m_h_gt1r, m_sig_conf_gt1r, bbox,
    m_t_gt1r)
mb_lat_gt2l, mb_lon_gt2l, mb_h_gt2l, mb_sig_conf_gt2l, mb_t_gt2l =
    mask_bbox(m_lat_gt2l, m_lon_gt2l, m_h_gt2l, m_sig_conf_gt2l, bbox,
    m_t_gt2l)
mb_lat_gt2r, mb_lon_gt2r, mb_h_gt2r, mb_sig_conf_gt2r, mb_t_gt2r =
    mask_bbox(m_lat_gt2r, m_lon_gt2r, m_h_gt2r, m_sig_conf_gt2r, bbox,
    m_t_gt2r)
mb_lat_gt3l, mb_lon_gt3l, mb_h_gt3l, mb_sig_conf_gt3l, mb_t_gt3l =
    mask_bbox(m_lat_gt3l, m_lon_gt3l, m_h_gt3l, m_sig_conf_gt3l, bbox,
    m_t_gt3l)
mb_lat_gt3r, mb_lon_gt3r, mb_h_gt3r, mb_sig_conf_gt3r, mb_t_gt3r =
    mask_bbox(m_lat_gt3r, m_lon_gt3r, m_h_gt3r, m_sig_conf_gt3r, bbox,
    m_t_gt3r)

m_ref_lat_gt1l, m_ref_lon_gt1l, m_corr_gt1l = mask_bbox2(ref_lat_gt1l,
     ref_lon_gt1l, corr_gt1l, bbox)
m_ref_lat_gt1r, m_ref_lon_gt1r, m_corr_gt1r = mask_bbox2(ref_lat_gt1r,
     ref_lon_gt1r, corr_gt1r, bbox)
m_ref_lat_gt2l, m_ref_lon_gt2l, m_corr_gt2l = mask_bbox2(ref_lat_gt2l,
     ref_lon_gt2l, corr_gt2l, bbox)
m_ref_lat_gt2r, m_ref_lon_gt2r, m_corr_gt2r = mask_bbox2(ref_lat_gt2r,
```

```
    ref_lon_gt2r, corr_gt2r, bbox)
m_ref_lat_gt3l, m_ref_lon_gt3l, m_corr_gt3l = mask_bbox2(ref_lat_gt3l,
    ref_lon_gt3l, corr_gt3l, bbox)
m_ref_lat_gt3r, m_ref_lon_gt3r, m_corr_gt3r = mask_bbox2(ref_lat_gt3r,
    ref_lon_gt3r, corr_gt3r, bbox)
```

Listing B.7: Mask photons and reference photons (for geophysical corrections) by bounding box (area of interst (AOI))

```
# Function to make the fitting process faster
def fit2(lat, lat2,  h, degree):
    p_fit = np.polyfit(lat, h, degree)
    p_val = np.polyval(p_fit, lat2)
    return p_val

# Apply geophysical corrections by 3rd degree polynomial
f_gt1l = fit2(m_ref_lat_gt1l, mb_lat_gt1l, m_corr_gt1l, 3)
h_f_gt1l = mb_h_gt1l- f_gt1l
f_gt1r = fit2(m_ref_lat_gt1r, mb_lat_gt1r, m_corr_gt1r, 3)
h_f_gt1r = mb_h_gt1r- f_gt1r
f_gt2l = fit2(m_ref_lat_gt2l, mb_lat_gt2l, m_corr_gt2l, 3)
h_f_gt2l = mb_h_gt2l- f_gt2l
f_gt2r = fit2(m_ref_lat_gt2r, mb_lat_gt2r, m_corr_gt2r, 3)
h_f_gt2r = mb_h_gt2r- f_gt2r
f_gt3l = fit2(m_ref_lat_gt3l, mb_lat_gt3l, m_corr_gt3l, 3)
h_f_gt3l = mb_h_gt3l- f_gt3l
f_gt3r = fit2(m_ref_lat_gt3r, mb_lat_gt3r, m_corr_gt3r, 3)
h_f_gt3r = mb_h_gt3r- f_gt3r

# Save as data frame for future processing
df_gt1l = pd.DataFrame({'lat':mb_lat_gt1l, 'h':h_f_gt1l, 'lon':
    mb_lon_gt1l})
df_gt1r = pd.DataFrame({'lat':mb_lat_gt1r, 'h':h_f_gt1r, 'lon':
    mb_lon_gt1r})
df_gt2l = pd.DataFrame({'lat':mb_lat_gt2l, 'h':h_f_gt2l, 'lon':
    mb_lon_gt2l})
df_gt2r = pd.DataFrame({'lat':mb_lat_gt2r, 'h':h_f_gt2r, 'lon':
    mb_lon_gt2r})
df_gt3l = pd.DataFrame({'lat':mb_lat_gt3l, 'h':h_f_gt3l, 'lon':
    mb_lon_gt3l})
df_gt3r = pd.DataFrame({'lat':mb_lat_gt3r, 'h':h_f_gt3r, 'lon':
    mb_lon_gt3r})

## MSS filtration (+- 3 m from MSS as sea ice is only here)
df_gt1l = df_gt1l[abs(df_gt1l['h'])<3]
df_gt1r = df_gt1r[abs(df_gt1r['h'])<3]
df_gt2l = df_gt2l[abs(df_gt2l['h'])<3]
df_gt2r = df_gt2r[abs(df_gt2r['h'])<3]
df_gt3l = df_gt3l[abs(df_gt3l['h'])<3]
df_gt3r = df_gt3r[abs(df_gt3r['h'])<3]
```

Listing B.8: Apply geophysical corrections by third degree polynomial

```
# Calculation relative elevations (highest-mean) for N = 150 segments
def calc_high_mean(df, n):
    # init
    value, lat, lon = [], [], [], [], [], [],[]
```

```
    # extract data
    df_lat, df_lon, df_h = np.array(df['lat'].dropna()), np.array(df['
        lon'].dropna()), np.array(df['h'].dropna())

    #calculate value max-mean within photon segment of n values
    for i in range(0, len(df_h)-1, n):
        # calculate as long as there are 150 photons available
        if i < len(df_h)-(n+1):
            track, track_lat, track_lon = df_h[i:i+n], df_lat[i:i+n],
                df_lon[i:i+n]
            value = np.append(value, np.max(track)-np.mean(track))
            lat = np.append(lat, np.mean(track_lat))
            lon = np.append(lon, np.mean(track_lon))
        elif i > len(track)-(n+1):
            break
    # save data to new dataframe
    df = pd.DataFrame({'lat':lat, 'lon': lon, 'h':value)
    return df

N = 150
df_gt1l_calc = calc_high_mean(df_gt1l_corr, N)
df_gt1r_calc = calc_high_mean(df_gt1r_corr, N)
df_gt2l_calc = calc_high_mean(df_gt2l_corr, N)
df_gt2r_calc = calc_high_mean(df_gt2r_corr, N)
df_gt3l_calc = calc_high_mean(df_gt3l_corr, N)
df_gt3r_calc = calc_high_mean(df_gt3r_corr, N)
```

Listing B.9: Calculate relative elevations (highest-mean) for N

```
# Calculate relative elevations (highest - median) of segments of N
    values (used in larger segment study)
def calc_high_median(df, n):
    # init
    value, lat, lon, list_mean, list_per90, list_per95,list_per99 =
        [], [], [], [], [], [],[]

    # extract data
    df_lat, df_lon, df_h = np.array(df['lat'].dropna()), np.array(df['
        lon'].dropna()), np.array(df['h'].dropna())

    #calculate value max-mean within photon segment of n values
    for i in range(0, len(df_h)-1, n):
        # calculate as long as there are 150 photons available
        if i < len(df_h)-(n+1):
            track, track_lat, track_lon = df_h[i:i+n], df_lat[i:i+n],
                df_lon[i:i+n]
            value = np.append(value, np.max(track)-np.median(track))
            list_mean = np.append(list_mean, np.max(track)-np.mean(
                track))
            list_per90 = np.append(list_per90, np.percentile(track-np.
                median(track), 90))
            list_per95 = np.append(list_per95, np.percentile(track-np.
                median(track), 95))
            list_per99 = np.append(list_per99, np.percentile(track-np.
                median(track), 99))
            lat = np.append(lat, np.mean(track_lat))
```

```
            lon = np.append(lon, np.mean(track_lon))
        elif i > len(track)-(n+1):
            break
    # save data to new dataframe
    df = pd.DataFrame({'lat':lat, 'lon': lon, 'h':value, 'mean':
        list_mean, 'per90':list_per90, 'per95':list_per95, 'per99':
        list_per99})
    return df

N = 15000
df_gt1l_calc = calc_high_median(df_gt1l_corr, N)
df_gt1r_calc = calc_high_median(df_gt1r_corr, N)
df_gt2l_calc = calc_high_median(df_gt2l_corr, N)
df_gt2r_calc = calc_high_median(df_gt2r_corr, N)
df_gt3l_calc = calc_high_median(df_gt3l_corr, N)
df_gt3r_calc = calc_high_median(df_gt3r_corr, N)
```

Listing B.10: Calculate relative elevations (highest-median) from longer segments

```
# Estimating DIR from 95% percentile
def DIR_calc(df):
    value, lat, lon = [], [], []

    #95% percentile
    DIR2 = np.array([0.38, 0.48])
    DIR3 = np.array([0.48, 0.60])
    DIR4 = np.array([0.60, 0.75])

    df_h = np.array(df['h'].dropna())
    df_lat, df_lon = np.array(df['lat'].dropna()), np.array(df['lon'].
        dropna())
    for i in range(0, len(df_h)):
        if df_h[i] > DIR2[0] and df_h[i] <= DIR2[1]:
            value = np.append(value, 2)
            lat = np.append(lat, df_lat[i])
            lon = np.append(lon, df_lon[i])
        elif df_h[i] > DIR3[0] and df_h[i] <= DIR3[1]:
            value = np.append(value, 3)
            lat = np.append(lat, df_lat[i])
            lon = np.append(lon, df_lon[i])
        elif df_h[i] > DIR4[0] and df_h[i] <= DIR4[1]:
            value = np.append(value, 4)
            lat = np.append(lat, df_lat[i])
            lon = np.append(lon, df_lon[i])

    df = pd.DataFrame({'lat':lat, 'lon': lon, 'cat':value})

    return df

df_result_gt1l = DIR_calc(df_gt1l_calc)
df_result_gt1r = DIR_calc(df_gt1r_calc)
df_result_gt2l = DIR_calc(df_gt2l_calc)
df_result_gt2r = DIR_calc(df_gt2r_calc)
df_result_gt3l = DIR_calc(df_gt3l_calc)
df_result_gt3r = DIR_calc(df_gt3r_calc)
```

Listing B.11: Estimate DIR from 95% percentile threshold-based intervals

```
from numpy import savetxt

# Extract longer segment of photons to create typical distributions
def calc_seg(df, n):
    # init
    value, list_mean, list_median = [], [], []

    # extract data
    df_lat, df_lon, df_h = np.array(df['lat'].dropna()), np.array(df['
        lon'].dropna()), np.array(df['h'].dropna())

    #calculate value max-mean, max-median and keep all elevations
        within photon segment of n values
    for i in range(0, len(df_h)-1, n):
        # calculate as long as there are 150 photons available
        if i == 0:
            track, track_lat, track_lon = df_h[i:i+n], df_lat[i:i+n],
                df_lon[i:i+n]
            value = np.append(value, track)
            list_mean = np.append(list_mean, track-np.mean(track))
            list_median = np.append(list_median, track-np.median(track
                ))
        elif i > 0 and i < len(df_h)-(n+1):
            track, track_lat, track_lon = df_h[i:i+n], df_lat[i:i+n],
                df_lon[i:i+n]
            value = np.vstack((value, track))
            list_mean = np.vstack((list_mean, track-np.mean(track)))
            list_median = np.vstack((list_median, track-np.median(
                track)))
        elif i > len(track)-(n+1):
            break

    return value, list_mean, list_median

N = 15000
text5 = '_n_'+str(N)+'_'
gt1l_value, gt1l_mean, gt1l_median = calc_seg(df_gt1l_corr, N)
gt1r_value, gt1r_mean, gt1r_median = calc_seg(df_gt1r_corr, N)
gt2l_value, gt2l_mean, gt2l_median = calc_seg(df_gt2l_corr, N)
gt2r_value, gt2r_mean, gt2r_median = calc_seg(df_gt2r_corr, N)
gt3l_value, gt3l_mean, gt3l_median = calc_seg(df_gt3l_corr, N)
gt3r_value, gt3r_mean, gt3r_median = calc_seg(df_gt3r_corr, N)

value_all = np.vstack((gt1l_value, gt1r_value, gt2l_value, gt2r_value,
    gt3l_value, gt3r_value))
mean_all = np.vstack((gt1l_mean, gt1r_mean,gt2l_mean, gt2r_mean,
   gt3l_mean, gt3r_mean))
median_all = np.vstack((gt1l_median, gt1r_median,gt2l_median,
   gt2r_median, gt3l_median, gt3r_median))
```

Listing B.12: Extraction of longer segments to create typical distributions

Technical University of Denmark
The National Space Institute (DTU Space)

Elektrovej, Bygning 327
2800 Kgs. Lyngby
Tlf. 4525 1700

www.space.dtu.dk